Letter of Intent
by the
SOLENOIDAL DETECTOR COLLABORATION
to construct and operate a detector at the
Superconducting Super Collider
30 November 1990

Summary

The Solenoidal Detector Collaboration (SDC) submits herewith its Letter of Intent (LoI) to propose a general purpose detector for a high-luminosity interaction region at the SSC. The SDC physics goals and the general characteristics of its detector have been described in the Expression of Interest submitted in May 1990. Since that time, the SDC detector concept has undergone some evolution, driven partly by the necessity of cost reduction and partly by progress in the design of various subsystems. Cost savings have been achieved through reduction of the central tracking volume, decrease in the tracking channel count, and replacement of the muon system intermediate-angle air-core toroids by iron toroids. The muon system has also been refined to improve triggering capability and overall performance. A magnet style has been chosen in which the calorimeter completely surrounds the coil to provide good hermiticity. Two calorimeter technologies have been chosen for further engineering work. A more detailed and accurate costing methodology has been put into place. As requested by the SSC Laboratory, this document also contains responses to specific questions asked by the Program Advisory Committee, and a budget request for engineering design and integration. The SDC is prepared to develop a detailed proposal for its detector within a year. Following approval, the SDC plans to fabricate its detector to be fully operational at SSC turn-on.

Contact person:
George H. Trilling, Spokesperson
50A-2160 Lawrence Berkeley Laboratory
Berkeley CA 94720
415/486-6801, Bitnet GHT@LBL

Members of the Solenoidal Detector Collaboration

Argonne National Laboratory: E. L. Berger, R. E. Blair, J. W. Dawson, T. L. Ekenberg, M. Derrick, T. H. Fields, V. Guarino, R. T. Hagstrom, N. F. Hill, P. K. Job, T. B. W. Kirk, E. N. May, J. Nasiatka, L. J. Nodulman, L. E. Price, J. Proudfoot, H. M. Spinka, R. L. Talaga, H.-J. Trost, D. G. Underwood, R. G. Wagner, A. B. Wicklund

University of Arizona: K. A. Johns

Institute for High Energy Physics, Beijing, China: Cui Huachuan, Gao Wenxiu, Huang Deqiang, Li Weiguo, Mao Huishun, Ni Huiling, Qi Nading, Wang Taijie, Yan Wuguang, Zhao Weiren, Zhou Yuehua

Beijing University, China: He Yu Ming, Lai Chu Xi, Liu Hong Tao, Liu Song Qiu, Lou Bing Qiao, Yang Ji Xiang, Yao Shu De, Zhang Re Ju

Brandeis University: S. Behrends, J. R. Bensinger, C. Blocker, P. Kesten, L. Kirsch

Bratislava State University, Czechoslovakia: P. Povinec, P. Strmen

University of Bristol: B. Foster, G. P. Heath

Brown University: D. Cutts, G. S. Gao, R. Partridge

Institute for Physics and Nuclear Engineering, Bucharest, Romania: A. Alexa, M. Horoi, D. Pantea, M. Pentia, C. Petrascu

California Institute of Technology: A. J. Weinstein

University of California at Davis: J. Gunion, D. Pellett, S. Mani

University of California at Irvine: A. Lankford

University of California at Los Angeles: K. Arisaka, H.-U. Bengtsson, C. Buchanan, D. Chrisman, D. Cline, J. Hauser, T. Muller, J. Park, D. Roberts, W. Slater

University of California at Riverside: J. Ellison, S. J. Wimpenny,

University of California at San Diego: M. Sivertz, D. Thomas

University of California at Santa Cruz: J. DeWitt D. Dorfan, C. Heusch, B. Hubbard, D. Hutchinson, A. L. Litke, W. Lockman, W. Nilsson, K. O'Shaughnessy, D. Pitzl, W. Rowe, H. Sadrozinski, A. Seiden, E. Spencer

Carleton University: J. Armitage, M. S. Dixit, P. Estabrooks, S. Godfrey, M. Losty, H. Mes, G. Oakham, M. O'Neille

Chiba University: H. Kawai

University of Chicago: C. Campagnari, M. Contreras, S. Eno, H. Frisch, C. Grosso-Pilcher, M. Miller, L. Rosenberg, H. Sanders, M. Shochet, G. Sullivan

University of Colorado: G. J. Baranko, H. W. K. Cheung, J. P. Cumalat, E. Erdos, W. T. Ford, U. Nauenberg, P. Rankin, G. Schultz, J. G. Smith

Joint Institute for Nuclear Research, Dubna: V. I. Astakhov, B. V. Batyunia, A. Bischoff, Y. A. Budagov, A. M. Chuenko, K. G. Denisenko, N. L. Denisenko, A. I. Dokshin, S. B. Gerasimov, V. M. Golovatyuk, Yu. N. Gotra, Yu. S. Gusar, Z. Guzik, D. I. Hubua, Yu. V. Ilyin, R. B. Kadyrov, S. V. Kashigin, Y. N. Kharzheev, I. F. Kolpakov, A. D. Kovalenko, F. V. Levchanovsky, Y. F. Lomakin, A. I. Malakhov, E. A. Matyushevsky, A. A. Omelianenko, Yu. S. Pakhmutov, Y. A. Panebratsev, I. V. Puzynin, A. A. Semenov, A. E. Senner, A. V. Shabunov, V. T. Sidorov, A. N. Sinaev, A. N. Sissakian, V. A. Smirnov, T. Spassoff, E. N. Tsyganov, I. A. Tyapkin, L. A. Vasilyev, G. V. Velev, V. B. Vinogradov, A. S. Vodopianov, V. Vrba, Y. V. Zanevsky, N. I. Zhuravlev, N. I. Zimin, A. I. Zinchenko

Duke University: A. T. Goshaw, S. H. Oh, T. J. Phillips, W. J. Robertson, J. D. Simpkins, W. D. Walker

Erevan Institute of Physics, USSR: A. C. Amatuni, G. A. Vartgapetian

Fermilab: V. H. Areti, M. Atac, E. Barsotti, L. Bartoszek, A. E. Baumbaugh, A. Beretvas, R. Bernstein, M. Binkley, A. D. Bross, A. G. Clark, J. W. Cooper, B. Denby, T. Droege, D. P. Eartly, J. E. Elias, R. W. Fast, D. Finley, G. W. Foster, J. Freeman, I. Gaines, S. A. Gourlay, D. R. Green, J. Grimson, C. Grozis, S. R. Hahn, R. M. Harris, J. Hoff, J. Huth, J. Hylen, R. D. Kephart, J. Kilmer, H. J. Krebs, J. Kuzminski, A. Lee, P. J. Limon, P. S. Martin, A. Mukherjee, T. Nash, C. Newman-Holmes, A. Para, J. Patrick, R. Plunkett, E. E. Schmidt, S. L. Segler, R. P. Stanek, A. Stefanik, H. J. Stredde, S. Tkaczyk, R. Vidal, R. L. Wagner, R. H. Wands, R. Yarema, G. P. Yeh, J. Yoh, T. Zimmerman

University of Florida: R. Field, J. Harmon, J. Walker

Florida State University: M. Corden, V. Hagopian, K. Johnson, H. Wahl

Fukui University: M. Kawaguchi, H. Yoshida

Gomel State University, USSR: A. M. Dvornik, N. B. Maksimenko

Harvard University: G. Brandenburg, G. Feldman, M. Franklin, S. Geer, J. Konigsberg, J. Oliver, E. Sadowski, P. Schlabach, R. Wilson

University of Hawaii: C. Kenney, S. Parker

Hiroshima University: Y. Chiba, T. Ohsugi

Hiroshima Institute of Technology: M. Asai

Ibaraki College of Technology: M. Shioden

University of Illinois at Chicago: H. Goldberg, S. Margulies, J. Solomon

University of Illinois at Urbana: R. Downing, S. Errede, A. Gauthier, M. Haney, L. Holloway, I. Karliner, A. Liss, T. O'Halloran, J. Thaler, P. Sheldon, V. Simaitis, J. Wiss

Indiana University: D. Blockus, B. Brabson, A. Dzierba, R. Foster, G. Hanson, X. Lou, F. Luehring B. Martin, H. Ogren, D. Rust, E. Wente

Iowa State University: J. Hauptman

Johns Hopkins University: J. A. Bagger, B. A. Barnett, B. J. Blumenfeld, P. H. Fisher, J. A. J. Matthews

University of Manitoba: G. Smith

McGill University: K. Ragan, D. G. Stairs

National Laboratory for High Energy Physics (KEK), Japan: F. Abe, K. Amako, Y. Arai, Y. Doi, H. Fujii, Y. Fukui, T. Haruyama, H. Ikeda, S. Inaba, T. Inagaki, H. Iwasaki, S. Kabe, N. Kanematsu, J. Kanzaki, T. Kondo, A. Maki, A. Manabe, M. Mishina, M. Noumachi, S. Odaka, K. Ogawa, T. K. Ohska, Y. Sakai, H. Sakamoto, O. Sasaki, T. Shinkawa, Y. Takaiwa, S. Terada, T. Tsuboyama, K. Tsukada, N. Ujiie, Y. Unno, Y. Watase, A. Yamamoto, Y. Yasu

Slovak Academy of Science, Košice, Czechoslovakia: F. Krivan, M. Seman, J. Špalek

Kyoto University: R. Kikuchi, K. Miyake

Lawrence Berkeley Laboratory: G. S. Abrams, A. Barbaro-Galtieri, R. M. Barnett, R. N. Cahn, C. A. Corradi P. H. Eberhard, K. Einsweiler, W. R. Edwards, R. Ely, M. G. D. Gilchriese, D. E. Groom, C. Haber, C. Hearty, I. Hinchliffe, M. Hoff, R. Jared, R. W. Kadel, J. A. Kadyk, S. Kleinfelder, M. E. Levi, A. Lim S. C. Loken, N. Madden, Y. Y. Minamihara, O. Milgrome, J. Millaud, T. L. Moore, D. R. Nygren, A. P. T. Palounek, W. L. Pope, M. Pripstein, J. Rasson, M. Shapiro, D. Shuman, H. G. Spieler, R. Stone, M. Strovink, W. Thur, G. H. Trilling, R. C. Weidenbach, W. A. Wenzel

Los Alamos National Laboratory: H. Ziock

University of Liverpool: J. Bailey, G. A. Beck, J. B. Dainton, E. Gabathuler, S. J. Maxfield

University of Manitoba: G. Smith

University of Maryland: A. R. Baden, A. H. Ball, C. Y. Chang, D. G. Fong, J. A. Goodman, N. J. Hadley, A. Jawahery, R. G. Kellogg, S. Kunori, A. Skuja, G. T. Zorn

University of Michigan: D. Amidei, R. C. Ball, M. Campbell, J. Chapman, K. De, P. Derwent, H. R. Gustafson, K. Hashim, S. Hong, L. W. Jones, S. B. Kim, M. J. Longo, J. Mann, M. R. Marcin, H. A. Neal, D. Nitz, B. P. Roe, G. Snow, R. Thun, D. Wu, S. Zhang

University of Minnesota: P. Border, H. Courant, R. Gray, K. Heller, Y. Kubota, M. Marshak, E. Peterson, R. Poling, K. Ruddick

Academy of Science of BSSR, Minsk, USSR: J. A. Kulchitsky, L. G. Moroz

University of Mississippi: D. Moore, D. Summers

Miyazaki University: T. Nakamura

Nagoya University: M. Nakamura, K. Niwa

Niigata University: K. Miyano, H. Miyata

University of Notre Dame: J. Bishop, N. Biswas, N. Cason, J. Godfrey, V. P. Kenney, J. Piekarz, R. Ruchti, W. Shepard

Oak Ridge National Laboratory: G. Alley, R. G. Alsmiller, Jr., F. S. Alsmiller, C. Y. Fu, C. W. Glover, J. Mahall, T. Ryan, D. Vandergriff

Ohio State University: B. Byslma, L. S. Durkin, T. Y. Ling, S. K. Park, T. A. Romanowski

Okayama University: N. Tamura

Osaka City University: T. Okusawa, T. Takahashi, Y. Teramoto, T. Yoshida

Osaka University: Y. Nagashima, S. Sugimoto

University of Oxford: J. Bibby, R. J. Cashmore, N. Harnew, R. Nickerson, W. Williams

University of Pennsylvania: L. Gladney, R. J. Hollebeek, M. Newcomer, R. Van Berg, H. H. Williams

Pennsylvania State University: T. A. Armstrong, K. W. Hartman, A. Hasan, S. F. Heppelmann, R. A. Lewis, E. D. Minor, B. Y. Oh, G. A. Smith, W. S. Toothacker, J. Whitmore, Y. Zhang

University of Pisa: R. Amendolia, F. Bedeschi, G. Bellettini, S. Galeotti, H. Grassman, M. Mangano, A. Menzione, G. Pauletta, D. Passuello, G. Punzi, L. Ristori

University of Pittsburgh: E. E. Engels, Jr., T. Humanic, P. F. Shepard

Purdue University: V. E. Barnes, A. F. Garfinkel, D. S. Koltick, A. T. Laasanen, R. McIlwain, D. H. Miller, E. Shibata, I. P. Shipsey

Rice University: D. Adams, S. Ahmad, B. Bonner, M. Corcoran, H. Miettinen, G. Mutchler, J. Roberts, J. Skeens

University of Rochester: A. Bodek, S. Kanda, F. Lobkowicz, A. Sill, P. Slattery, E. H. Thorndike

Rockefeller University: G. Appolinari, N. Giokaris, D. Goulianos, P. Melese, R. Rusack, A. Vacchi, S. White

Rutgers University: T. Devlin, T. Watts

Rutherford Appleton Laboratory: M. Edwards, N. Gee, G. Grayer

CEN Saclay, France: P. Bonamy, J. Ernwein, R. Hubbard, P. Le Du, J.-P. Pansart, F. Rondeaux

Saga University: A. Murakami, S. Kobayashi

Saitama College of Health: K. Masuda

Sofia State University, Bulgaria: R. V. Tsenov, A. B. Iordanov

Superconducting Super Collider Laboratory: D. Bintinger, D. Coupal, A. Fry, H. Johnstad J. Siegrist, M. Turcotte

Institute of Nuclear Physics, Tashkent, USSR: S. Aliev, S. Kan, A. Khaneles, A. Pak, E. Surin, B. Yuldashev

Physical Technical Institute, Tashkent, USSR: M. Alimov, K. Gulamov, V. Kaprior, V. Myalkovski, K. Turdaliev, A. Yuldashev

Institute of High Energy Physics, Tbilisi State University, USSR: N. S. Amaglobely, B. G. Chiladze, D. I. Hubua, R. G. Salukvade

Tel Aviv University: J. Grunhaus, R. Heifetz, A. Levy

Texas A&M University: E. Barasch, T. Bowcock, F. R. Huson, P. M. McIntyre, J. T. White

University of Texas at Dallas: C. D. Cantrell, R. C. Chaney, E. J. Fenyves, H. Hammack, J. Orgeron, W. B. Lowery, N. P. Johnson,

Tohoku Gakuin University: M. Higuchi, Y. Hoshi

Tohoku University: K. Abe, K. Hasegawa, H. Yuta

University of Tokyo (Institute for Nuclear Study): S. Kato, K. Nishikawa, S. Homma, T. Miyachi

Tokyo Institute of Technology: K. Kaneyuki, T. Tanimori, Y. Watanabe,

Tokyo Metropolitan University: M. Chiba, R. Hamatsu, T. Hirose

Tokyo University of Agriculture and Technology: T. Emura, K. Takahashi

University of Toronto: D. C. Bailey, G. J. Luste, J. F. Martin, R. S. Orr, J. D. Prentice, P. Sinervo, T-S. Yoon

University of Tsukuba (Institute of Physics): I. Fujiwara, Y. Funayama, K. Hara, T. Iinuma, T. Kaneko, S. Kim, K. Kondo, S. Miyashita, Y. Morita, I. Nakano, M. Takano, K. Takikawa, K. Yasuoka

University of Tsukuba (Institute of Applied Physics): Y. Asano, S. Mori, Y. Takada

Tufts University: T. Kafka, W. A. Mann, R. H. Milburn, A. Napier, K. Sliwa

Virginia Polytechnic Institute and State University: B. Lu, L. W. Mo, T. A. Nunamaker, L. E. Piilonen

Wakayama Medical College: M. Daigo

University of Washington: R. J. Davisson, G. Liang, H. J. Lubatti, R. J. Wilkes, T. Zhao

University of Wisconsin: J. Bellenger, D. Carlsmith, J. Cherwinka, A. Erwin, F. Feyzi, C. Foudas, J. Lackey, R. Loveless, G. Ott, D. D. Reeder, W. Smith, C. Wendt, S. L. Wu

rk University: W. R. Frisken, D. Hasell, R. Koniuk

Other collaborators involved in the SDC proposal preparation:

IBM FSD Team:

Dallas Marketing Center: W. Courtney, S. Fisher
Houston Laboratory: A. Elam, E. Poole
Manassas Laboratory: C. Caprio, P. Kapcio
Owego Laboratory: B. Buddle, T. Gerace

Space Sciences Laboratory, University of California at Berkeley: J. F. Arens, J. G. Jernigan

Hughes Electro-optical & Data Systems Group and Hughes Technology Center: G. Atlas, O. Barkan, T. Collins, G. Kramer, C. Pfeiffer, B. Wheeler, D. Wolfe, S. Worley

Rockwell International Corporation: E. J. Anderson, M. D. Petroff

RTK Engineering: J. Brown, L. Dittert, W. McGinley, A. Nunez, M. Riddle

Silicon Dynamics Inc.: D. Klokow, L. VanderHave

Westinghouse Science and Technology Center: M. A. Burke, C. W. Einolf, D. T. Hackworth, D. Marschik, D. W. Scherbarth, R. L. Swensrud, J. M. Toms

Table of Contents

1. Introduction 3
2. Progress since the Expression of Interest 3
3. The SDC detector 4
   3.1. Overview and design goals 4
   3.2. Status of the detector design 8
      3.2.1. Tracking system 8
      3.2.2. Superconducting solenoid 12
      3.2.3. Calorimeter system 14
      3.2.4. Muon system 19
   3.3. Cost estimate 24
4. Physics capabilities 26
   4.1. Overview 26
   4.2. Higgs 26
   4.3. Top quark with mass 250 GeV 29
   4.4. Jet energy resolution 36
   4.5. Z' with mass 4 TeV 39
5. Organization and management of the collaboration 42
6. Budget request 43
7. References 44

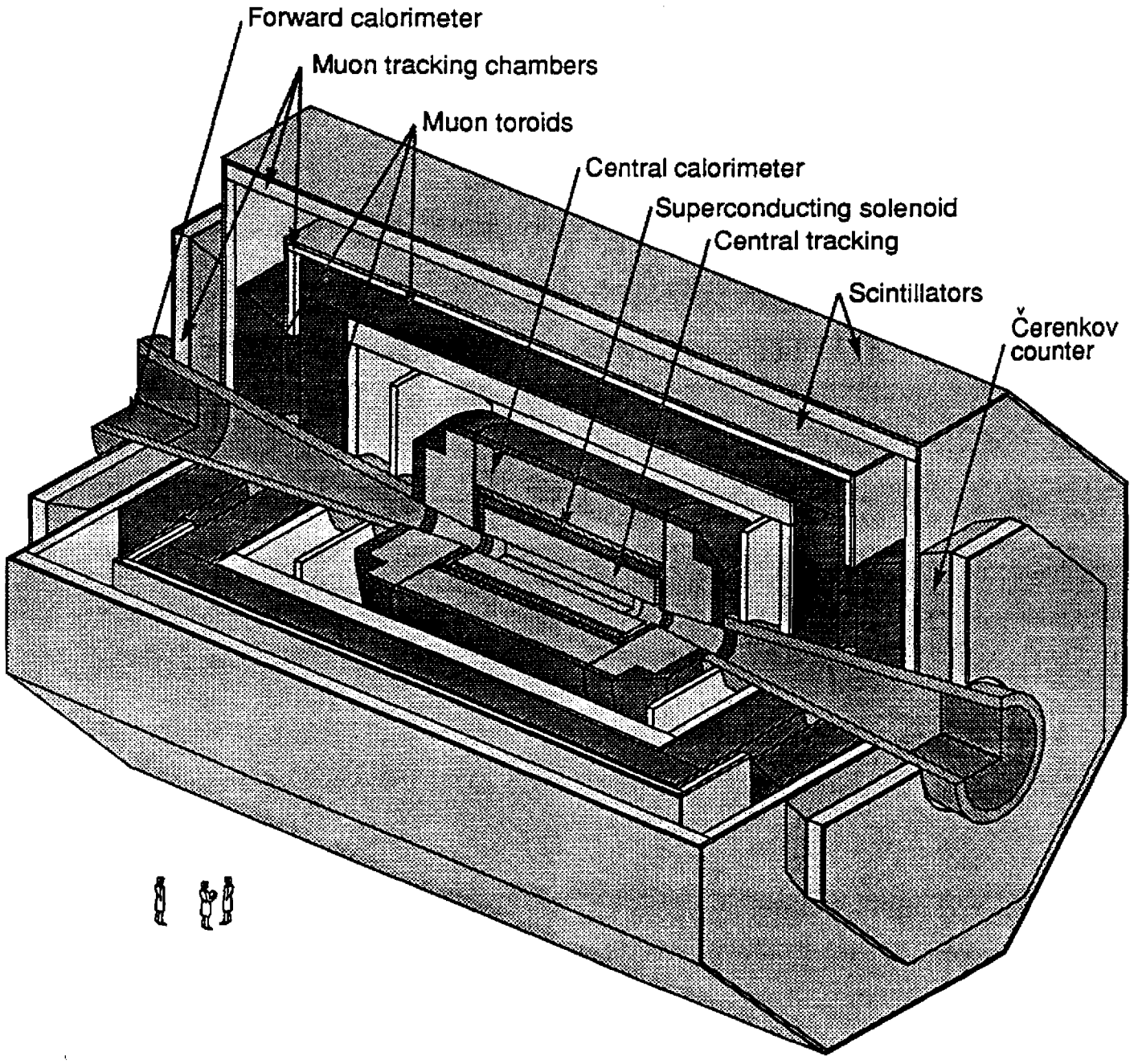

FIG. 1. Overall view of the detector.

1. Introduction

This document is a Letter of Intent (LoI) submitted by the Solenoidal Detector Collaboration (SDC) for a general-purpose detector aimed at pursuing a broad range of physics goals at the SSC. While the proposed detector is optimized for high-p_t physics, it also has diverse capabilities that make it a premier exploratory tool for a broad range of physics topics. We intend to build a detector whose subsystems are all fully functional at the design luminosity of $10^{33}\,\mathrm{cm}^{-2}\mathrm{s}^{-1}$, and which, with somewhat reduced functionality, can tackle the more specialized physics issues which require substantially higher luminosity.

The SDC submitted an Expression of Interest (EoI) in May 1990[1]. It provided a set of responses to questions from the Program Advisory Committee (PAC) in July 1990[2]. The SSCL/PAC responded to the EoI submissions with a decision to support two high-p_t detectors with complementary and overlapping capabilities, one being general-purpose and the other of a more specialized character. Scope reductions to a level of about $500M were mandated. The SSCL called for Letters of Intent proposing detectors of appropriately reduced scope, and also containing answers to several questions prepared by the PAC. This document is the SDC response to the SSCL invitation.

As mandated by the SSCL, this LoI is very brief, and much of the requested information is contained in our EoI. Nearly half of the LoI is devoted to answering the PAC questions, and most of the other half discusses those subsystems in which major evolution has occurred since the EoI: tracking, magnet, calorimetry, and muon systems. A new methodology has been used as the basis for our cost estimate. We also provide a budget request for FY1991 for engineering, integration and R&D not covered under subsystem work, and a budget for FY1992 based on the assumption that all R&D relevant to SDC will then be included in the SDC budget.

---

2. Progress since the Expression of Interest

The SDC detector design has evolved substantially since the submission of the EoI. The changes have been driven partly by more realistic studies of how the various subsystems are assembled and maintained, and partly by the necessity of scope reduction to fit into the cost guidelines suggested by the SSCL. In addition we have reduced the number of technical options under consideration.

The major developments which have occurred since the EoI submission are briefly summarized here and discussed in more detail in the later sections of this LoI. The first three items listed below are motivated by the requirement of scope reduction:

1. The tracking volume has been reduced, the outer radius shrinking from 1.85 m to 1.70 m and the half-length from 4.5 m to 4.0 m. This action reduces the volume and hence the cost of the calorimetry and muon systems external to the tracking. The consequences are a reduction in momentum precision and increased occupancy in the outermost (triggering) tracking superlayer.
2. The tracking system channel count has been reduced. The total area of the silicon system has been decreased and the channel count for the outer tracker has been reduced by about 25%. The performance price is a slight reduction in momentum resolution and some loss in pattern recognition capability.
3. The air-core toroids in the intermediate-angle region of the muon system have been replaced by iron toroids. The consequence is some degradation in momentum precision in the p_t range 100–500 GeV/c due to multiple scattering in the iron toroids. (At lower p_t the central tracker is adequate, and at higher p_t the multiple scattering is relatively unimportant.)

While these scope reduction measures produce some loss in performance, we believe that the detector capabilities remain adequate for fulfilling our goals.

The following developments arise from our progress in narrowing technological alternatives, in elaborating our design, and in improving our cost-estimating methodology:

4. The solenoid magnet style has been chosen on the basis of careful work of an SDC Task Force[3]. The design selected is a unified version of Types S and I described in the EoI, in which the coil is

entirely surrounded by the calorimeter. The task force considered issues of coil fabrication, assembly, and cost, as well as the impact of magnet style on calorimetry, tracking, and triggering. The rejection of a design in which the coil penetrates the calorimeter (Type L in the EoI) is motivated primarily by the resulting deterioration of calorimeter performance.

This selection leads to a somewhat nonuniform field if the calorimeter is nonmagnetic, and a uniform field in the case of an iron-loaded calorimeter. On the basis of studies done to date, we believe that the tracking can be done adequately in the nonuniform field[4].

5. The choice of calorimeter technologies targetted for more extensive engineering design has been narrowed. Our immediate engineering efforts for the central calorimeter ($|\eta| < 3$) will be focused on just two technologies, one using scintillator and the other using liquid ionization. Our specific choices for the detection media are scintillator tile with wave-shifting fiber readout and liquid argon. These choices have been made on the basis of engineering, costing, simulation, and risk assessment studies.
6. Progress on the engineering design of both mechanical and electronic aspects of the tracking systems has led to improved cost estimates for these systems.
7. The arrangement of muon tracking detectors has been modified to optimize performance and triggering capability.
8. The specifications of the overall architecture and protocol of the trigger systems have been refined. These include Level 1 pipeline lengths, Level 1 and 2 trigger signals, and the handling of busy, reset, and initialize states. There has also been considerable progress in the development of critical custom integrated circuits for the readout of tracking systems and calorimetry[5,6].
9. A proposal for extensive test-beam work in the areas of tracking, calorimetry, and muon systems, following the next collider run, has been submitted to Fermilab.

Since the EoI submission, groups from Canada, China, France, Israel, and Romania have joined the SDC. We have also added industrial partners to assist in the preparation of the proposal. These are separately listed at the beginning of this LoI.

In view of our progress and the development of our technical organization, we are confident that, with a reasonable level of support for engineering design, we shall be ready to make a full-scale proposal for our detector in about one year.

---

3. The SDC detector

3.1. Overview and design goals

3.1.1. Detector description

The Expression of Interest submitted last May provides a description of the SDC physics goals. These include studies of electroweak symmetry breaking, properties of the top quark, searches for heavier gauge bosons, for evidence of compositeness, and for new particles implied by supersymmetry, and, most important of all, the uncovering of totally new and unexpected phenomena.

To meet the challenges implicit in these goals, we are proposing a general purpose detector with central tracking in a solenoid magnetic field, hermetic calorimetry, identification and energy measurement of electrons and muons, and high resolution vertex detection. We believe that these capabilities will provide the power and level of redundancy essential for understanding new phenomena at the SSC. Our intention is to design a detector whose subsystems are all fully functional at the design luminosity of $10^{33}\,\mathrm{cm}^{-2}\mathrm{s}^{-1}$, and which can tackle more specialized physics issues at substantially higher luminosity with somewhat reduced functionality.

As discussed in Chapter 2, there has been substantial progress since the submission of the EoI. Table 1 summarizes the detector design goals, and replaces the corresponding table in the EoI.

Fig. 1 shows an isometric view of the SDC detector. Quadrant views corresponding to two different choices of calorimetry are shown in Figs. 2 and 3.

Fig. 2 shows the detector with calorimetry based on lead and iron absorbers and scintillator-tiles with wave-shifting fiber readout. Inside the short coil, the

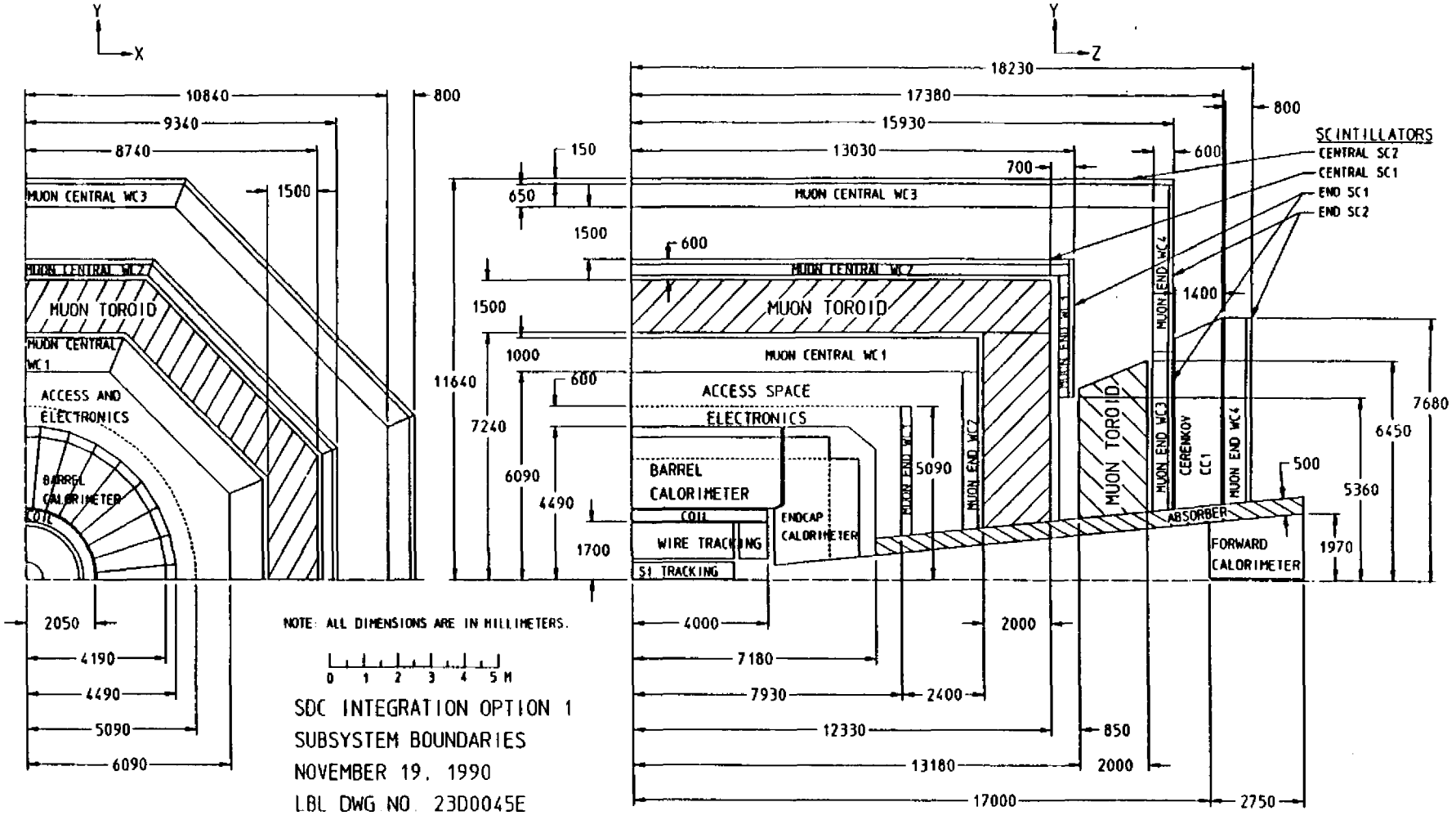

FIG. 2. Quadrant plan view of SDC detector with lead/scintillator calorimeter option.

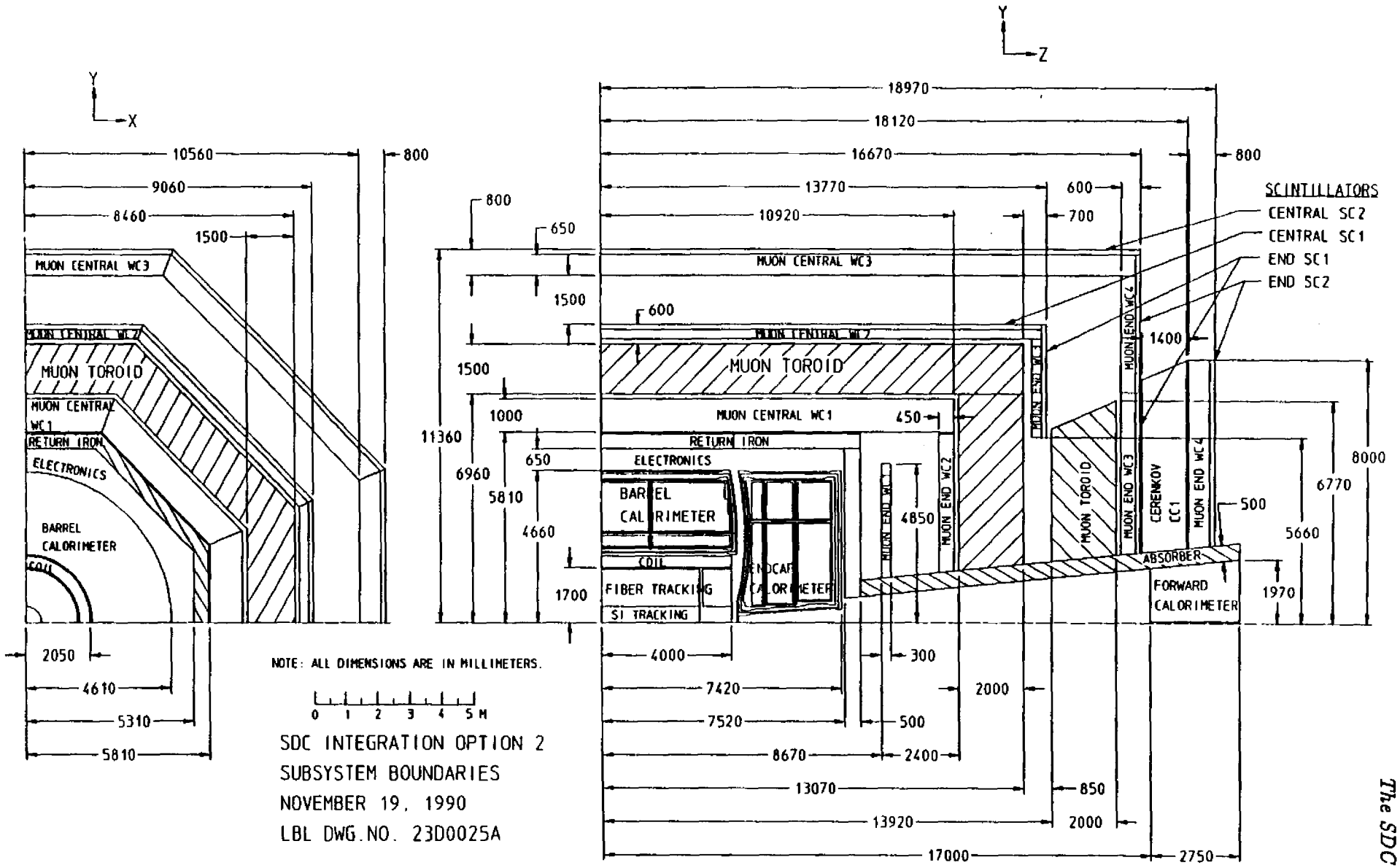

FIG. 3. Quadrant plan view of SDC detector with lead/liquid argon calorimeter option.

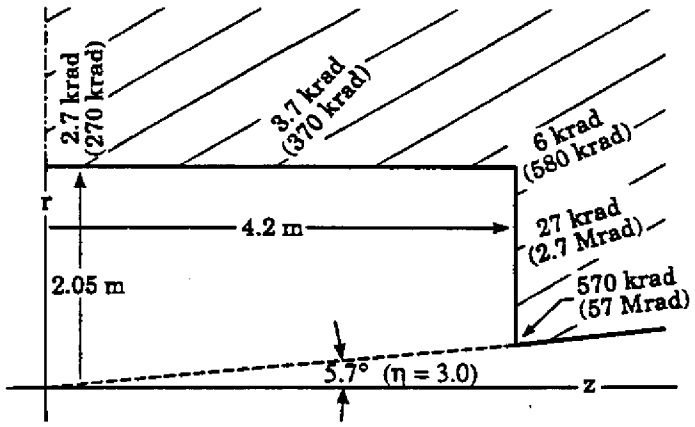

FIG. 4. Maximum ionizing dose in the SDC calorimeter, for standard conditions ($10^{33}\,cm^{-2}s^{-1}$, 1 year) and (in parenthesis) for 10 years at $10^{34}\,cm^{-2}s^{-1}$. The maximum dose occurs at electromagnetic shower maximum. Values have been corrected from those given in the EoI.

central tracker consists of a small-radius silicon strip and pixel system, plus a wire or scintillating fiber tracking system at the larger radii. The return flux is carried partly by the structural element shown at the back of the calorimeter and partly by steel used as the absorbing medium in the last few interaction lengths of the calorimeter. The muon system consists of two scintillator layers for triggering and a set of wire tracking modules. Momentum measurements independent of central tracking information are provided by the iron toroids in both the central and forward directions. Unlike the system described in the EoI, the muon tracking modules are not all identical, and the two modules originally depicted on the inside of the central steel toroid have now been combined into one larger module placed close to the inside surface of the toroid. It should be noted that the combination of measurements in the ϕ direction in the central tracker and in the muon system provides a precision for high energy muons that is significantly better than with either system alone.

Fig. 3 shows the detector with Pb/liquid-argon calorimetry. The absence of radial access space in this case is motivated by both the larger radial dimension of the liquid argon calorimeter and the likelihood that safety considerations would in any case preclude use of access space with a liquid argon calorimeter. The flux return is completely external. The central tracking and muon systems are unchanged.

3.1.2. High-luminosity operation

The radiation environment has been discussed in some detail in the EoI. The ionizing dose in the calorimetry is greatest at electromagnetic shower maximum, and representative values of the dose are shown in Fig. 4. These are a factor of three smaller than in the corresponding Fig. 6 of the EoI because of the discovery of an error[7].

Since the SSC has the potential of operating at luminosities an order of magnitude higher than the design value of $10^{33}\,cm^{-2}s^{-1}$, we intend that our detector retain sufficient functionality at the higher luminosities to study the specialized physics issues requiring higher event rates.

The calorimeter must have the capability to survive the larger doses shown in Fig. 4 (at least in the pseudorapidity range $|\eta| < 3$). For a scintillation calorimeter, the design may include the possibility of replacing damaged scintillator in a limited part of the endcaps.

At the higher luminosities, the tracking system must retain sufficient functionality to provide a stiff-track trigger and momentum resolution of reduced precision. Recent measurements indicate that silicon-strip detectors and radiation-hardened electronics should survive for at least several years at $10^{34}\,cm^{-2}s^{-1}$[5,8], but more R&D is necessary. The performance of the outer tracker at high luminosity depends on which of the technological options is retained: the wire chamber option suffers serious occupancy problems at luminosities much above the design value, although the superlayers at the largest radii may still be able to function. The scintillating fiber option offers the potential of reducing the occupancy by an order of magnitude, but additional R&D is required to establish cost and feasibility.

The muon system will have some stand-alone capability, but its performance will be greatly enhanced by the limited level of central-tracking capability expected at $10^{34}\,cm^{-2}s^{-1}$.

In summary, we are making good progress toward the design of a general-purpose detector of acceptable cost fully operational at the SSC design luminosity. We plan to make our technological decisions taking account of the needs of a physics program continuing to luminosities of $10^{34}\,cm^{-2}s^{-1}$.

Table 1
Detector design goals.

	Central $\lvert\eta\rvert \lesssim 1.5$	Intermediate $1.5 \lesssim \lvert\eta\rvert \lesssim 3.0$	Forward $\lvert\eta\rvert \gtrsim 3.0$
Tracking:			
Magnetic field	2.0 T	2.0 T	No
Radius	1.70 m	1.70 m	
$\delta p_t/p_t^2$ at 1 TeV/c	< 0.25 (TeV/c)$^{-1}$	< 1.3 (TeV/c)$^{-1}$ [a]	
Calorimeter:			
Inner boundary[b]	2.05 m	4.2 m	17 m
Depth	$\gtrsim 9\lambda$	$\gtrsim 12\lambda$	$\gtrsim 14\lambda$
Segmentation (Had)	0.05–0.10[c]	0.05–0.10[c]	10 cm × 10 cm
Resolution (Had) $\delta E/E$	$< 0.7/\sqrt{E} \oplus 0.04$[d,e]	$< 0.7/\sqrt{E} \oplus 0.04$	$< 1.0/\sqrt{E} \oplus 0.05$
Resolution (EM) $\delta E/E$	$< 0.25/\sqrt{E} \oplus 0.02$	$< 0.25/\sqrt{E} \oplus 0.02$	
Electron ID	Yes	Yes	None
Muon system:			
Total absorber	$\geq 14\lambda$	$\geq 14\lambda$	—
$\delta p_t/p_t^2$ at 1 TeV/c (central tracker plus toroids)	$\lesssim 0.13$ (TeV/c)$^{-1}$	$\lesssim 0.45$ (TeV/c)$^{-1}$ [a]	—

[a] At $\lvert\eta\rvert = 2.5$; full tracking capabilities extend to $\eta = 2.5$.
[b] Radius for central calorimeter and z-position for intermediate and forward calorimeters.
[c] $\Delta\eta = \Delta\phi$.
[d] E is in GeV unless otherwise specified.
[e] Here and elsewhere, $\oplus$ indicates addition in quadrature.

3.2. Status of the detector design

3.2.1. Tracking system

The tracking system plays a major role in exploratory physics, lepton and heavy quark identification, mass reconstruction, and in the formation of the trigger, as discussed in Section 3.2 of the EoI. We have put emphasis on reliable pattern recognition and precise momentum and vertex resolution over the pseudorapidity range $\lvert\eta\rvert \leq 2.5$ required for SSC physics. The basic goals for the SDC tracking system, updated from the EoI, are indicated in Table 1. To these general goals we add several more specific requirements:

1. Pattern recognition capability even within jets of p_t up to 1 TeV/c;
2. High resolution vertex detection capable of identifying jets containing b hadrons with good efficiency;
3. Capability of providing Level 1 or 2 trigger information to identify tracks of p_t greater than 10 GeV/c;
4. Functionality of at least part of the tracking system at luminosities significantly above the SSC design value.

Overview of the tracking system

The central tracking system consists of the elements described in Section 4.1 of the EoI. In order of increasing radius, they are:

1. Two-dimensional pixel silicon detectors to aid pattern recognition and detect separated vertices from heavy quark decay;
2. An array of silicon strip detectors to provide pattern recognition and momentum measurement in the pseudorapidity range $\lvert\eta\rvert < 2.5$;
3. A wire-chamber and/or scintillating fiber system to provide the curvature determination needed for high precision momentum and vertex measurements and trigger information for high-p_t particles over the same pseudorapidity range.

Tracking systems using wire chambers and scintillating fibers for the outer tracking technologies are shown in Figs. 5(a) and (b). All tracking elements are organized into superlayers, with each superlayer measuring the space coordinate and the local slope of track segments. As superlayers have significant local pattern-finding capabilities, this results in substantial immunity to detector backgrounds and allows a powerful first-level trigger. The track segments found in each superlayer are readily linked into complete tracks, for example by finding clusters in curvature-azimuth space. Simulations of $Higgs \rightarrow ZZ \rightarrow e^+e^-\mu^+\mu^-$ with tracking elements as in Fig. 5(b) result in high lepton tracking efficiencies even for luminosities substantially greater than $10^{33}\,\mathrm{cm}^{-2}\mathrm{s}^{-1}$, as shown in Fig. 6[5].

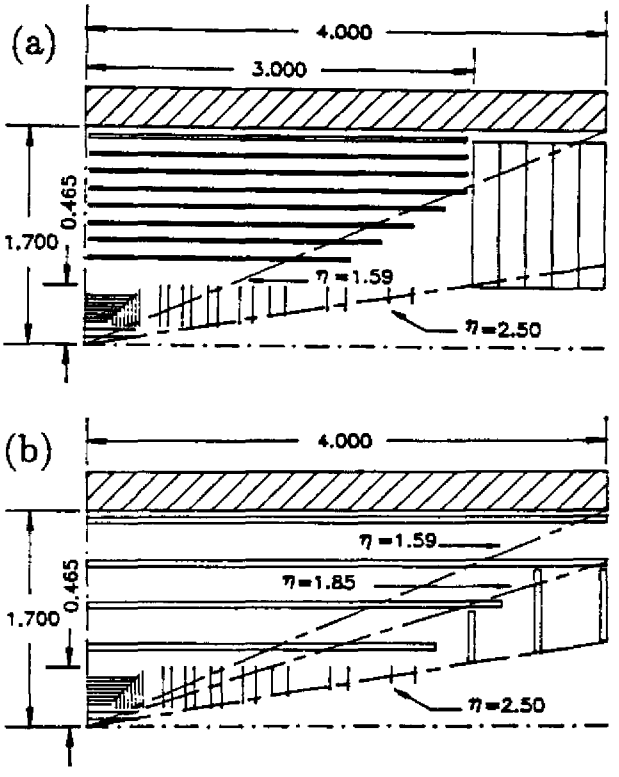

FIG. 5. Tracking system for the SDC detector. At small radius are silicon pixel and strip detectors. Surrounding these are (a) barrel superlayers of straw tubes with radial wire chambers covering the intermediate-angle region; (b) an alternative implementation employing scintillating fiber modules for both the barrel and end regions. Dimensions are in meters. Other variations mentioned in the text are not shown.

As part of the mandated reduction in detector costs, the radius and half-length of the tracking system have been reduced from their EoI values of

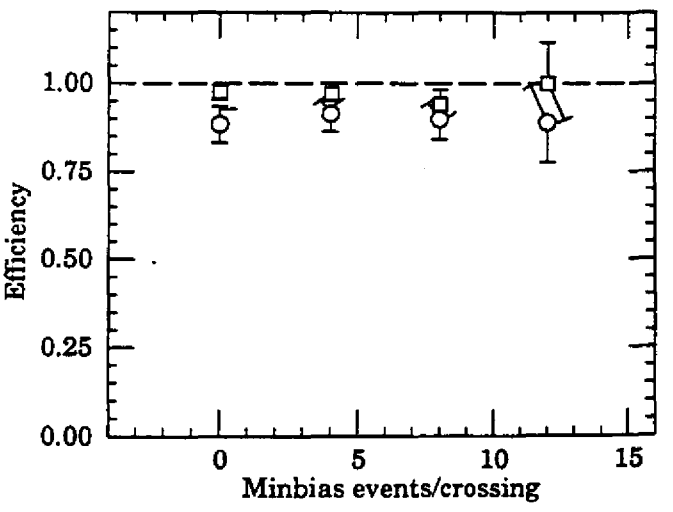

FIG. 6. Tracking efficiency for the process $H \rightarrow Z^0Z^0 \rightarrow e^+e^-\mu^+\mu^-$. Crosses show the efficiency for finding all four leptons; circles for all four leptons also passing the requirement that their reconstructed momenta be within a factor of 2 of their true momenta.

1.85 m by 4.5 m to 1.70 m by 4.0 m. The main cost savings of this change arise from the reduction in the weight of both the calorimeter and the muon toroids. We have obtained further cost savings through reduction of tracking system channel counts by about 25%. These savings lead to a degradation in momentum measurement precision of about 25%, reduced redundancy in pattern recognition, and increased occupancies in the outer "triggering" layers of the tracker. The magnitude of these effects appears to be sufficiently small as not to impair significantly the ability of the detector to achieve the stated physics goals. Quantitative understanding of these issues will require further R&D, detailed simulations, and, eventually, knowledge of the actual technologies to be used for the tracker.

In the next subsections we describe the present versions of the tracking elements. It should be understood that the designs are preliminary. As we improve our simulations and understand the costs better, it is likely that many of the details will change.

Silicon system

The silicon system consists of an array of two-dimensional pixel detectors plus a large array of silicon strip detectors. The pixel detector[9] consists of two concentric cylindrical layers and two disk arrays, and covers a pseudorapidity interval $|\eta| < 1.9$. The pixel detector is contained within a radius of 10 cm and ± 22 cm along the beam direction. Pixel

sizes are expected to be 30 μm × 300 μm in the ϕ and z directions respectively, and the position resolutions are expected to be better than 10 μm in ϕ and 100 μm in z. The pixel superlayer aids pattern recognition, provides superb capability to detect separated vertices from heavy quark decays, and contributes to momentum resolution.

The silicon strip detectors are arranged in 8 cylindrical layers and 44 planar layers. Cost savings relative to the EoI design are achieved by moving the forward planar layers closer to the interaction point and scaling down their radial dimensions, leaving the acceptance unchanged. This degrades the momentum resolution at large pseudorapidities by about 30%. The silicon layers will be instrumented with either double-sided strip detectors or with single-sided short-strip detectors. The double-sided strip detectors have axial (or ϕ) strips on one side and small-angle stereo strips on the other side of each detector, while the single-sided short-strip detectors have each strip subdivided into many short strips to provide pixel-like information. Two layers of such detectors form a superlayer. (Note that individual silicon layers, rather than superlayers, are shown in Fig. 5.)

Radiation tests of bipolar transistors, CMOS transistors for digital applications, and strip detectors were made under the Silicon Subsystem R&D Program[5,8]. The results obtained so far suggest survivability for several years at a luminosity of $10^{34}\,\mathrm{cm}^{-2}\mathrm{s}^{-1}$, but much more R&D remains to be done. There has also been progress in the design of a very stable low-mass mechanical support structure and a viable cooling scheme[5]. Continued support of the silicon subsystem R&D program is critical to the development of the inner tracker of the SDC detector.

Outer tracking system

For radii greater than 50 cm, the tracking technologies under consideration include straw tube and radial wire drift chambers, scintillating fibers, and combinations of these. Active R&D efforts are being pursued for all of these technologies, and should continue to be supported through the relevant subsystem programs.

Our design for a straw tube tracking system covering central pseudorapidities consists of eight superlayers of 4 mm diameter straws. The inner seven superlayers contain six layers per superlayer, whereas the outermost superlayer (in axial geometry) has eight layers to help maintain robustness for a Level 1 trigger. Information along the z direction is provided by 3° stereo superlayers (two stereo-left and two stereo-right). This design, coupled with the reduced tracking outer radius, provides about a 25% reduction in the channel count relative to that given in the EoI.

Substantial progress relative to this design has been made through the Subsystem R&D efforts. This includes extensive studies of prototype straws, development of intermediate wire supports inside the straws, detailed design of end plates including gas manifolding and electronics layout, and the design of mechanical structures for supporting the straws[10,11]. A cosmic ray study of the spatial resolution of a 2.7 m long, eight tube deep stack of 4 mm straws has measured a single tube resolution of $\sigma = 120$ μm[12]. Pattern recognition studies show that segments within straw superlayers are reconstructed with good reliability for stiff tracks, and support our tentative decision to reduce the number of straw layers in a superlayer from eight to six[13].

At intermediate pseudorapidities our wire-based design employs radial wire chambers, supplemented by cathode-strip readout MWPC "crossing taggers," which give coarser position resolution but sharper time resolution than the radial wire drift cells, to resolve the event arrival/drift time ambiguity. These MWPC's also provide the Level 1 or 2 trigger in this region. Experiments with fast drift gases and strong drift fields show the Lorentz angle effects to be manageable, and simulations yield encouraging results concerning the ability of a radial drift plus crossing tagger configuration to extract the good hits from a noisy environment[10]. The current drawn in these chambers remains a concern for operation above the design luminosity, and much work is needed to clarify the way to form a Level 1 trigger with this system. This work is being vigorously pursued in Great Britain.

Extensive research on wire aging has demonstrated that the gas CF_4 combines high drift velocity with a remarkable protective power against wire damage[10,11]. Work at TRIUMF[14] and LBL[15] has demonstrated that CF4-isobutane shows no gain loss for collected charge of more that 1 C/cm corresponding to about 10 years at design luminosity for an inner layer. Direct measurements and operation of straw chambers in nuclear reactors indicate that straw components will survive more that 10^{14} neutrons/cm^2 and that a chamber will continue to

operate with no gain loss while running in this environment at rates exceeding 5 MHz[16]. These numbers indicate that neutrons are an insignificant source of radiation damage to straw chambers at the SSC.

However occupancy considerations indicate that the operation of the wire tracker becomes increasingly problematical as luminosities rise beyond the SSC design value. This makes a tracking system based on scintillating fibers very attractive, because occupancies are an order of magnitude smaller. The principal change from the design given in the EoI is an increase of the fiber diameter from 500 μm to 750 μm, with a corresponding channel count reduction[17]. The occupancies still remain small, and the light output is increased. The amount of material in the tracker is increased, and the precision and two-track resolution are slightly degraded. However, by offsetting the four fiber rows within a layer by a quarter-fiber diameter, one obtains an axial measurement of precision $(750\ \mu\text{m}/4)/\sqrt{12} = 55\ \mu$m. Each superlayer provides two such measurements, separated by about 5 cm, which are used to form local track segments.

For fiber tracking in the intermediate pseudorapidity region, one can use disks of right-bending and left-bending spirals of scintillating fibers plus half-circles of azimuthal fibers to determine (r, ϕ) unambiguously at each location along the z axis[17].

The scintillating fiber subsystem group has developed several new highly-efficient primary dyes for scintillators from which materials that fluoresce in the green to yellow can be fabricated[17]. The successful splicing of scintillating fibers to clear fiber waveguides by thermal fusion has been accomplished, and the visible light photon counter (VLPC) is being developed at the Rockwell International Science Center[17]. The VLPC is a solid state photodetector with $> 60\%$ quantum efficiency across the visible spectrum. These devices operate near liquid helium temperatures with nearby preamplifiers, which may be at about liquid nitrogen temperatures. The major R&D challenge will be the development of a readout scheme whose cost per channel, including all necessary packaging, will be acceptably low.

Another option for the central pseudorapidity region is the use of a hybrid design for the outermost superlayers, with two fiber row pairs of $\pm 5°$ stereo adjacent to an axial straw superlayer[11]. The hybrid tracking superlayers are relatively simple mechanically, and the resulting module yields a localized three-space point together with a direction vector in (r, ϕ). These track segments are then easily employed in the subsequent track linking.

For the intermediate-angle tracking system gas microstrip or gas pixel detectors are also possibilities, although extensive R&D is required. In principle, the microstrip detector[18] features 20 μm resolution, 20 ns pulses, low thickness in radiation lengths, high tolerance to radiation, and direct digital data flow for fast triggers. Prototype chambers have been built and will soon be tested.

R&D on charged particle triggers based on the tracking system includes simulation studies and development of custom circuits to recognize stiff track segments within superlayers in real time[17,10]. Initial simulations of first-level charged track triggers with the scintillating fiber outer tracker find good immunity to false $p_t > 10$ GeV/c triggers even for luminosities substantially above $10^{33}\,\text{cm}^{-2}\text{s}^{-1}$[17]. Study of a charged track trigger using the forward silicon planes suggests that a p_t sensitive trigger for the difficult region $1.2 < |\eta| < 2.5$ can probably be realized at Level 2[19].

Performance characteristics

The principal characteristics of the proposed tracking systems are shown in Tables 2 and 3, and the expected momentum resolution is shown in Fig. 7. As in the EoI, the simulations described in Section 4 use more conservative resolutions than those in Fig. 7 to account for systematic effects.

Technological choices

On the basis of R&D and engineering work already done, it seems very likely that a silicon plus gas-wire tracking system can be implemented at acceptable cost with adequate performance up to the SSC design luminosity. However, gas-wire tracking at higher luminosity appears problematical because of excessive occupancy, at least for the inner layers. Fibers and other technologies hold the promise of operation at much higher luminosity, but they require further R&D to establish feasibility and cost. Milestones for the tracking system R&D for FY1991 are given in Table 4. Over the next few months we will develop a detailed schedule and corresponding R&D plan going beyond FY1991 to allow us to take maximum advantage of technological advances compatible with our goal of having a fully functional

Table 2
Central Tracking

Detector type	Pixels	Silicon Strips	Outer Wires	Outer Scifi
Total number of elements	3.0×10^7	3.6×10^6	1.9×10^5	1×10^6
Number of superlayers	1	4	8	4
Measuring layers/superlayer	2	4	6 (8)	8 (16)
Approx. occupancy per element (in 2 T field at $\mathcal{L} = 10^{33}\,\mathrm{cm}^{-2}\mathrm{s}^{-1}$)	10^{-4}	10^{-3}	10^{-1}	10^{-2}
Total radiation lengths at normal incidence	1.5%	5%	4.5%	6.7%
Resolution/measurement	10 μm × 100 μm	15 μm	150 μm	(text)
Two-track resolution	100 μm × 500 μm	150 μm	2 mm	1 mm

Table 3
Intermediate Angle Tracking

Detector type	Pixels	Silicon Strips	Outer Wires	Outer Scifi
Total number of elements	9×10^6	4.9×10^6	5×10^4	2×10^5
Number of superlayers	1	5[a]	5	3
Measuring layers/superlayer	2	4	8	12
Approx. occupancy per element (in 2 T field at $\mathcal{L} = 10^{33}\,\mathrm{cm}^{-2}\mathrm{s}^{-1}$)	10^{-4}	10^{-3}	10^{-1}	10^{-2}
Total radiation lengths at normal incidence	1.5%	6%	6%	8%
Resolution/measurement	10 μm × 100 μm	15 μm	150 μm	250 μm
Two track resolution	100 μ × 500 μm	150 μm	2 mm	1 mm

[a] Number of superlayers intersected by a track.

detector at SSC turn-on. For FY1991, continuation of R&D efforts on wire, fiber, and hybrid outer trackers as well as silicon strip and pixel inner trackers is essential. In this LoI we request funding to support engineering design and systems integration for both silicon and outer trackers.

3.2.2. Superconducting solenoid

The EoI described three possible solenoid coil configurations. An SDC task force was charged with assembling technical and cost information relevant to each of these magnet styles, and studying the impact of each choice on calorimetry, tracking, and triggering. As a result of this study[3], the type-L design, in which the coil penetrates the calorimeter and extends to a solid iron yoke, was dropped. At the same time, the type-S and type-I coil options were combined into a single unified design (type-U) to be the focus of engineering design and R&D

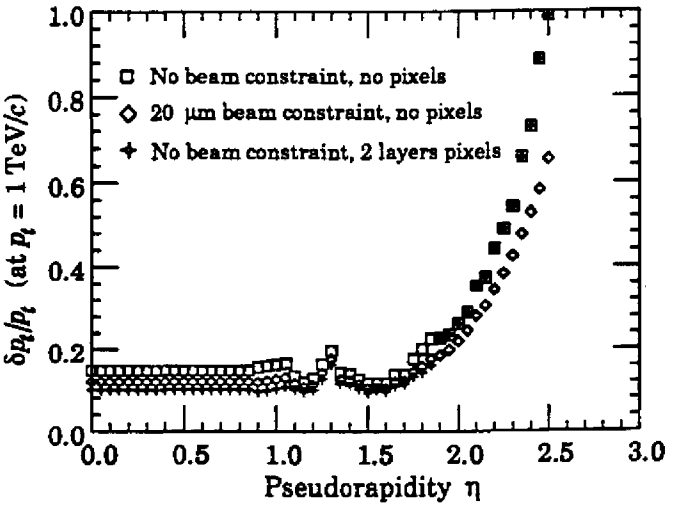

FIG. 7. Momentum resolution vs. η for either the pixel/silicon strip/wire chamber outer tracking system or the pixel/silicon strip/scintillating fiber outer tracking system, based on 100% measurement efficiency and the resolutions given in Tables 2 and 3. Systematic errors are not included.

Table 4
Tracking System Milestones (FY1991)

Milestone	Date
Pixels	
Conceptual design review	Dec. 1990
Fabrication of pixel array prototype	March 1991
Pixel array beam tests	July 1991
Mechanical systems prototype	Sept. 1991
Silicon Strips	
Prototype full-size mechanical module	Sept. 1991
Test of full-size double-sided silicon detector	Sept. 1991
Prototype front-end electronics	Sept. 1991
Establish radiation limits for detectors	Sept. 1991
Wire Drift Chambers	
Beam tests with prototype front-end/trigger electronics	May 1991
Intermediate tracker radial drift chamber sector prototype	June 1991
Full-size barrel module/superlayer prototypes	June 1991
Evaluation of full-scale full-length barrel module prototype	Sept. 1991
Scintillating Fibers	
Beam tests of full-size superlayers using multi-anode phototubes	Feb. 1991
Prototype commercial fabrication of wide fiber ribbons	April 1991
Beam test of 256-channel 4 m long fiber superlayer with VLPCs plus front-end/trigger electronics	May 1991
Delivery of 1000 channels of VLPCs from Rockwell	Oct. 1991

activities. This design is to be usable with either a magnetic endcap calorimeter or with a nonmagnetic one (Fig. 8). Fig. 9 shows the field integral as a function of pseudorapidity for the two cases. The magnet thickness at 90° will be about 1.2 X_0. The axial compressive force on the coil is 360 tonnes with magnetic endcap calorimetry and 1614 tonnes with nonmagnetic. To avoid yielding the aluminum-based superconductor, the axial force in a coil for use with nonmagnetic calorimetry must be transferred to the outer support cylinder and carried as a compressive stress in it. Since this force for the SDC Type-U solenoid is much greater than that found in other detector solenoids, substantial R&D is required to develop a method of bonding or mechanically interlocking the conductor turns to the outer support cylinder. This joining method must be very reliable in the long-term because a failure of the joint would cause the magnet to quench before the operating current is reached. This effort and other required R&D, which will involve Fermilab, KEK, and industrial partners, is briefly described below.

R&D plan for type-U Solenoid

1. *Engineering design:* This will include stress, thermal, quench, and safety analyses and will specify the utility systems (power supply and refrigerator) required. The axial support system will be designed for axial force constants of 50 tonnes cm^{-1} and 5 tonnes cm^{-1}, for use with magnetic or nonmagnetic calorimeters, respectively.
2. *Superconductor:* The goal of this R&D is a conductor stabilizer with a yield strength greater than 50 MPa and a resistivity at 4.5 K of less than 50 pΩ-m. The high strength would make the bond between conductor and outer support cylinder less essential to the ability of the magnet to reach the design current. The technique to co-extrude aluminum around a Cu/Nb-Ti ca-

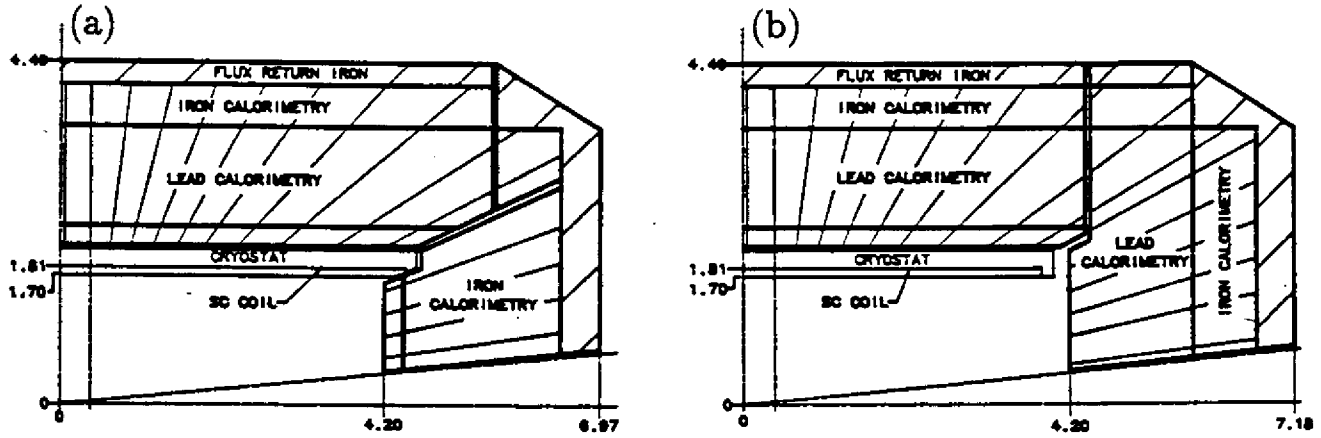

FIG. 8. Coil-iron-calorimeter geometries for Type-U solenoid with magnetic endcap calorimetry (a) and with nonmagnetic endcap calorimetry (b). The axial field at the origin is 2 T in either case. The stored energy with iron calorimetry is 147 MJ; with nonmagnetic calorimetry it is 122 MJ.

ble to final dimensions about 5×50 mm must be developed and demonstrated.

3. *Coil fabrication:* The most important coil fabrication R&D item is the development of a satisfactory method to attach the conductor to the outer support cylinder. A major part of the R&D program is the fabrication of a full-diameter prototype coil of partial length. Mechanical, cryogenic, superconducting excitation, and quench tests will be performed on this prototype.
4. *Cryostat and cryogenics:* To achieve the desired transparency the outer vacuum shell must be fabricated of a material with a density 15–20% that of bulk aluminum. A cylinder about 4 m diameter × 1–2 m long will be fabricated of honeycomb to demonstrate the suitability of this material. Other low-density vessel fabrication techniques will be investigated. The feasibility of a thermosiphon to cool the coil will be determined and the predictability and reliability of this method compared to a liquid helium pump- or compressor-driven force flow.

Some support for the U.S. part of this R&D is included in our funding request.

3.2.3. Calorimeter system

The operational environment and general design goals of the SDC calorimetry have been presented in section 4.3 of the EoI. A summary of the design goals is presented in Table 1. The SDC calorimeter

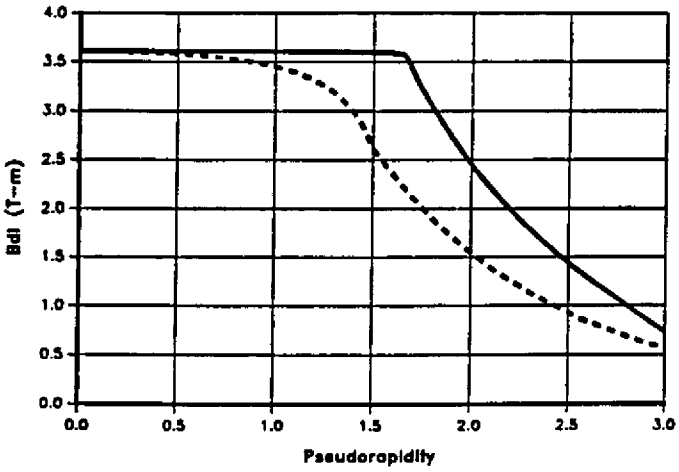

FIG. 9. Bending power versus pseudorapidity for a Type-U solenoid with (a) iron endcap calorimetry and (b) nonmagnetic endcap calorimetry.

system consists of a central, high precision calorimeter ($|\eta| < 3$) and forward calorimetry covering the region $3 < |\eta| < 5$.

When the EoI was submitted, five calorimeter technologies for the central pseudorapidity region were under study. Two technologies with complementary risk elements have now been chosen for engineering development in preparation of the proposal. These two options will be pursued with comparable priority to guarantee at least one technology that can meet our cost, physics performance,

and other requirements. The options are: (1) scintillating tiles with wave-shifting fiber readout and lead/iron absorber; and (2) liquid argon with lead absorber. The choice between these two techniques, planned for no later than the fall of 1991, will be based on a comparison of the physics performance, technical risks, cost, schedule, and the impact of the integration of the calorimeter with the other detector elements. Table 5 summarizes some of the parameters of the two options. In the scintillator option, lead absorber is used in the electromagnetic section, but two choices of absorber are being explored for the hadronic section. The first is a fine-sampling lead section of about seven interactions lengths (including the electromagnetic section) followed by about three interaction lengths of iron with coarser sampling, that also acts to return the magnet flux from the solenoid. The other choice is a full iron hadronic section, possibly with small amounts of lead to attempt to adjust the ratio of electron to hadron response to be near unity. This second choice has the advantage of somewhat lower cost and a uniform magnetic field for tracking. A combination of the two techniques, iron hadronic calorimetry in the endcap region and lead/iron hadronic calorimetry in the barrel is also being explored. This would also provide a uniform field. The test program to study these choices, as well as the liquid argon option, is described later.

The primary goals of the forward calorimetry are to (1) provide excellent hermeticity for missing-E_t triggers and measurements, and (2) tag jets in the forward pseudorapidity region. Pending further study we do not anticipate using the forward calorimetry for electron identification or for multi-jet mass reconstruction. The radiation environment in the forward region is particularly hostile, and we are just now beginning the process of evaluating the technologies or combinations of technologies that will both survive and adequately function in this difficult region. To avoid closing out the possibility of employing promising technologies other than scintillating tile or liquid argon for the forward calorimeters, an aggressive R&D program to demonstrate and compare the feasibility and cost effectiveness of warm liquid, liquid scintillating fiber, and high pressure gas calorimetry will be pursued. Since missing-E_t measurements depend critically on forward calorimetry, this R&D effort is extremely important. However, the smaller scale of the forward calorimetry allows us more time to pursue R&D before choosing a technology than is the case for the central system.

Scintillating tiles with fiber readout

There is a wealth of experience with scintillator plate calorimeters at hadron collider experiments (CDF, UA1, and UA2). More recently, a high quality scintillator plate calorimeter has been constructed for operation in the ZEUS detector. Members of the SDC have participated in the construction and operation of the CDF calorimeters and in the construction of the ZEUS calorimeter. This experience gives us confidence that a scintillating tile calorimeter can be constructed to meet our physics goals through adequate longitudinal and lateral segmentation, excellent hermeticity, an intrinsically fast and low-noise signal readout and accurate calibration by radioactive sources and high-rate processes such as $Z \rightarrow e^+e^-$.

Fig. 19 in the SDC EoI illustrates the concept of the scintillating tile/fiber readout calorimeter for the SDC detector and its realization in the detector is shown in Fig. 2[20]. The key element in this technique is a scintillator plate about 2.5 mm thick with an embedded wavelength-shifting fiber about 1 mm in diameter. This fiber is bonded to a high-transmittance clear fiber that channels the light to phototubes mounted on the back of the calorimeter. The major concerns to be addressed before this technology can be adopted for the detector are radiation hardness of the scintillator and fiber systems, uniformity of light collection over the tile surface, calibration methodology, choice of absorber material, physics performance, and the engineering and production of a system with about one million tile assemblies with high reliability. Since most of these R&D issues will be addressed in the context of the Subsystem R&D proposal on scintillating plate calorimetry, adequate support of this proposal by the SSCL is essential.

Test beam results and plans

Several prototype electromagnetic and hadron calorimeters using tiles with fiber readout have been built and tested in 25 GeV to 150 GeV beams at Fermilab during the past year. The results have been presented at the recent Fort Worth Symposium on Detector R&D for the SSC. Electromagnetic resolution of about $20\%/\sqrt{E} \oplus 1\%$ has been achieved, along with uniformity across tower boundaries of better than 2% for a small number of towers.

Additional studies are planned at Fermilab in the next 6–8 months. These will include further measurements of plate-to-plate uniformity in prototype

Table 5
Parameters for the Calorimeter Options

	Scintilator Tile Fiber Pb/Fe Absorber	Liquid Argon Lead Absorber
Channel count—towers	41000	87400
Channel count—strips	25000	0[a]
EM depth (X^0) at 90°	25	25
Full depth (λ) at 90°	~ 10	~ 9
Depth segmentation	2 EM, 2 HAD	MG,[b] 2 EM, 2 HAD
$\Delta\phi \times \Delta\eta$	$\sim 0.05 \times 0.05$	0.025–0.05 × 0.025–0.05
Peaking time, EM/HAD	15–30/15–30 ns	100/200 ns
EM resolution	$15\%/\sqrt{E} \oplus < 1\%$	$15\%\sqrt{E} \oplus 0.5\%$
Hadronic resolution	$\sim 40\%/\sqrt{E} \oplus \sim 2\%$	$\sim 60\%\sqrt{E} \oplus < 4\%$
EM position resolution	2–3 mm[c]	2–5 mm[c]
Electronic plus pileup noise, $\Delta R = 0.15$ cone at $10^{33}\,\mathrm{cm^{-2}s^{-1}}$	0.2 GeV	1.2 GeV

[a]EM position resolution is provided by fine tower segmentation. If strips are used, channel count will remain about the same.
[b]MG = Massless gap.
[c]EM position resolutions for one transverse direction for scintillator, and both transverse directions for liquid argon.

electromagnetic modules and measurements of e/h in variable iron/lead mixtures. Exposures in test beams to test radiation hardness are described below.

Radiation hardness studies

Radiation damage of the scintillating tiles and readout fibers in the electromagnetic section of the calorimetry could potentially be the limiting factor in this technology. There are four ways to obviate the effects of radiation damage: (1) develop scintillators more resistant to radiation; (2) perform *in situ* calibration using radioactive sources and the copious Z and W decays; (3) replace scintillator every few years in the regions of highest dose; and (4) use a radiation resistant technology, *e.g.* warm liquid calorimetry, for the electromagnetic sections in the region of highest dose, followed by scintillator hadronic sections. Our present assessment is that, with a safety factor of two, the new generation of scintillators recently developed will allow operation to pseudorapidity of about two for an integrated luminosity of 10^{42} cm^{-2}, *i.e.* 10 years of operation at $\eta^{34}\,\mathrm{cm^{-2}s^{-1}}$[21]. In forming this conclusion, full advantage is taken of (a) longitudinal segmentation to help correct for the depth nonuniformity of the damage and (b) *in situ* calibration provided by the large rate of $Z \to ee$ and $W \to e\nu$ events. At the design luminosity of $10^{33}\,\mathrm{cm^{-2}s^{-1}}$ we estimate that it will be possible to calibrate each tower to a precision of better than 1% in a period of 15 days[21]. These conclusions are supported by measurements on a limited sample of scintillators. For example, measurements on 2.5 mm thick Bicron RH1 scintillator plate irradiated with electrons to 1 Mrad showed only a 1.3% loss of light yield after annealing and negligible reduction in attenuation length for 10 cm × 10 cm plates[22]. Development of scintillators with improved hardness is in progress[23]. Although these results are very encouraging, much work remains to investigate long-term exposures and various systematic effects in electromagnetic modules. Complete system tests are being planned to measure the radiation hardness of real calorimeter modules. Several electromagnetic calorimeter test modules will be built and exposed over short and long periods in electron beams with doses up to tens of Mrad to evaluate damage and performance. These tests will take place in Japan (KEK), China, the Soviet Union, and France (Orsay), since no suitable high intensity

electron beams will be available in the United States.

Choice of Absorber

The choice of absorber in the hadronic section is influenced not only by calorimeter performance but by cost considerations and the benefit of a uniform magnetic field for tracking. Lead/scintillator in the thickness ratio of about 4:1 is known to be compensating, at least for gate times of 50–100 ns. Since one of the advantages of scintillator is speed, we have explored by Monte Carlo simulation the effects of smaller integration times as shown in Fig. 10[24]. These studies indicate that an iron absorber would yield an e/h of about 1.2. It may be possible to reduce this value by sandwiching lead inside iron plates to decrease the electromagnetic response[25]. The effects of various absorber choices will be studied in a test beam at Fermilab by next summer. We expect to select the absorber type after these tests and other studies.

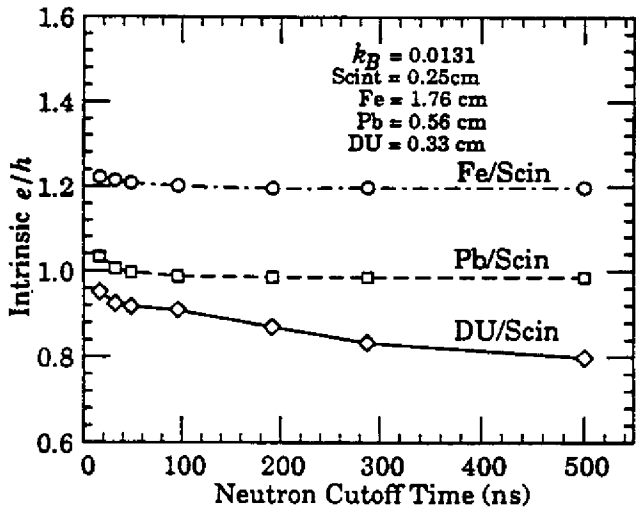

FIG. 10. The electron-hadron response (e/h) for different calorimeter compositions vs. integration time. From Ref. 24.

Engineering issues

Substantial progress has been made in demonstrating the feasibility of lead absorber supported by an integral steel trusswork of plates; this work is by Argonne and the Westinghouse Science and Technology Center[26]. Tests are underway to evaluate the feasibility of making large castings of lead with precision slots. A prototype EM module using this technique will be available early next year. If this approach is not feasible, plates of absorber will be used. Although a conceptual design exists, much more engineering is needed to provide a preliminary design, including integration with other detector systems. Funds to help support this work are requested in this LoI.

Work has started at Fermilab to evaluate the design based on an iron hadronic calorimeter. Substantial engineering studies are required to evaluate the effects of magnetic forces as well as the impact on other systems. Funds to support this effort are also requested here.

Finally, the manufacturing, testing, and assembling of about one-million tiles is a formidable task. The Westinghouse Science and Technology Center, experienced in industrial-scale production, will study this task along with Fermilab and Argonne.

Liquid argon (LAr)

Large liquid argon calorimeters have been reliably operated in many experiments, and substantial experience has been accumulated by members of the SDC in the MARK-II, D0, and VENUS experiments. This experience gives us confidence that a liquid argon system can be constructed to meet our goals. Fig. 3 shows the liquid argon calorimeter option for the detector in more detail. The calorimeter modules use lead plate absorbers. The magnet return iron is located outside the calorimeter cryostat. Liquid argon calorimetry is intrinsically radiation resistant. Recent tests of hybrid preamplifiers that could be located in the liquid indicate the viability of liquid argon over the central pseudorapidity range for integrated luminosity in excess of 10^{41} cm^{-2}, if care is taken in locating the preamplifiers for the region $2.5 < |\eta| < 3$[27]. In addition, liquid argon is known to provide excellent uniformity, stability, and ease of calibration. The critical issues for LAr are e/h, electronic and pileup noise, hermeticity, engineering design and reliability, integration into the total detector, safety, and cost.

Test beam plans and e/h

A large scale Pb/LAr module prototype calorimeter will be tested at BNL next spring with a fast, low noise readout, employing preamplifiers in the LAr. This test will measure e/h in the energy range of 0.5 to 20 GeV. Adequate support of this work through the Liquid Argon Subsystem R&D proposal is critical to the evaluation of liquid argon calorimetry for the SDC detector. The value of e/h for lead liquid

argon is not well known. Results of the SLD group, with a thin calorimeter, yield values in the 1.3–1.4 range[28]. Monte Carlo results from some years ago, indicate a value closer to 1.2[29]. Recent studies using EGS may indicate that values 1.1–1.15 could be obtained by using steel cladding of the lead[25]. Finally, the feasibility of using weighting techniques to bring the effective e/h near 1, as will be done by the H1 group[30], is under study by us.

Engineering

Liquid argon is a mature technology, and detailed engineering work is now needed to evaluate the impact of design choices on physics performance. A conceptual engineering design of the cryostat, modules and feedthroughs, including fabrication and assembly feasibility, has been made by Kawasaki Heavy Industries, KEK, and LBL. Although not yet optimized, this design already indicates that the acceptance for excellent electron energy measurements exceeds 93% for $|\eta| < 2.5$. EGS studies indicate that massless gaps in the barrel-endcap transition region can raise the acceptance to approximately 97%[31]. More work is needed on the cryostat design for the region near $|\eta| = 3$. We have a preliminary design of the cryogenics system for the calorimeter and for the interaction hall. We are continuing to develop a safety system concept that meets SSCL requirements. Support is requested in this LoI to continue these mechanical engineering studies.

We are seeking a speed of response from the liquid argon system that so far has not been necessary in a colliding beam environment. There is a very close connection among mechanical design, electrical (signal propagation) requirements, and the design of preamplifiers. Our first choice is to locate the preamplifiers in the liquid argon and to couple the signal from the calorimeter stacks through magnetic transformers. Shielding magnetic transformers up to an external field of about 0.7 T has been demonstrated[3,32]. The solenoid field is such that it now appears that transformers can be located as needed, although care will be required in part of the endcap region. Our future electromechanical engineering efforts will emphasize shielding the readout transformers, designing and testing a cooling system for preamplifiers in the LAr, and establishing the reliability of electronics mounted within the calorimeter. Considerable progress has already been made in understanding and optimizing calorimeter design to minimize noise, for preamplifiers either inside or outside the cryostat. For preamplifiers inside, with 100 ns peaking time, the expected electronic noise is 0.8 GeV in a full depth tower of $\Delta\eta \times \Delta\phi = 0.1 \times 0.1$. Simulations of pileup noise give a pileup transverse energy of 0.4 GeV at $\mathcal{L} = 10^{33}\,\mathrm{cm}^{-2}\mathrm{s}^{-1}$ for the same conditions. Timing resolution of better than 5 ns is possible for electrons with $E_t > 15$ GeV.

Although our first choice is to locate preamplifiers inside the cryostat, we are continuing to pursue the use of electrostatic transformers (EST) and location of the preamplifiers outside the cryostat. A 20 gap Pb/LAr module with electrostatic transformer (EST) readout and preamplifiers outside of the cryostat has been used to detect cosmic rays with fast (170 ns) peaking time and signal to noise of three to one[33]. The development of this readout method will continue at least until the reliability of preamplifiers situated inside the cryostat is established.

Forward calorimeter

The primary function of the forward calorimeter is to complete the containment for the measurement of missing-E_t. The extreme radiation level in this region restricts the choice of possible technologies, and an evaluation of these has begun. Technologies to be investigated with active R&D efforts in the next year are liquid argon, warm liquid, liquid scintillator fiber, and high pressure gas ionization calorimetry. We briefly address each of these techniques, except liquid argon, below.

Warm-liquid ionization calorimeter

The warm-liquid R&D has concentrated on purity and material compatibility, readout speed and signal-to-noise, radiation damage, and the design of a proof-of-principle test module. Significant progress has been made in the last year and some test beam results are now available[34]. Issues of purity appear to be tractable and the next key goal is to finish construction of a large Test Beam Module next summer, and initiate its beam test by late 1991 or early 1992. This would provide a full scale test suitable for evaluating this technique for forward calorimetry. We encourage the SSCL to support the subsystems proposal in this area so that this test may be completed in a timely fashion.

Scintillating liquid fiber calorimeter

Some work has started on using liquid scintillator in tubes, which may be appropriate in the very high radiation area[35]. Considerable R&D and prototype development is needed to evaluate this technique.

High pressure gas calorimeter

Prototype Pb-Xe and Pb-Ar high pressure gas calorimeters have been constructed and exposed to electron test beams in the USSR by members of the SDC. Work is also underway in the United States[36]. This technique should be particularly insensitive to radiation damage (with remote or shielded electronics).

Preshower and shower-maximum detectors

Preshower and shower-maximum detectors provide more precise position information for electromagnetic showers. Several physics signatures can be improved with the addition of one or the other of these detectors. We are considering a preshower detector with scintillating fibers having a one millimeter pitch, with the coil providing most of the preradiator material in the barrel region. Alternatively, we would use strips about 2 cm wide in each calorimeter tower at shower maximum. The preshower detector would improve electron identification for electrons near jets and also provide improved photon identification by rejecting neutral pions at energies up to about 100 GeV. The strips at shower maximum do equally well for electron identification, but would provide little help for photons. Preshower and shower maximum detectors will be tested with a tile-fiber calorimeter at FNAL in the coming year. Design of strips for liquid argon is primarily an engineering issue and is proceeding. Selection of a preshower or shower maximum detector will be made at the same time as the choice between scintillating fiber and LAr calorimetry. Design work on the preshower detector is underway in France (Saclay) and in the United States.

Calorimeter selection and milestones

A selection of the calorimeter technology for the central region is planned by no later than the fall of 1991. The decision will be based on an assessment of the physics performance, technical risk, and cost factors associated with each of the two technologies. In addition to the R&D efforts already mentioned in the paragraphs above, we have formed study groups to compare the performance of the two technologies. These include:

1. A study of the effect of the pileup and shaping times on electron isolation and missing E_t performance for both options;
2. Evaluation of the physics impact of transitions between the barrel, end cap and forward calorimeters;
3. Assessment and measurements of electron/hadron compensation, and its physics and technology impact;
4. A critical assessment of the physics requirements at luminosities greater than $10^{33}\,\mathrm{cm}^{-2}\mathrm{s}^{-1}$ with special emphasis on processes that distinguish between the technologies.

Table 6 summarizes the performance and R&D milestones foreseen during FY1991. R&D for technologies that may be used for the forward calorimetry is not listed in the table.

3.2.4. Muon system

There have been two major changes in the muon system since the EoI. The first of these is that 4 m thick iron toroids have replaced superconducting air-core toroids in the endcap region. The air-core toroids had been proposed in the EoI in order to have relatively uniform muon momentum resolution over the pseudorapidity range $|\eta| < 2.5$. The decision to replace the air-core toroids with iron toroids is based on cost-benefit considerations applied to the SSCL mandate to reduce the SDC detector scope.

The air-core toroids improve the muon resolution in the region of $1.7 < |\eta| < 2.5$ in the p_t range of 100 to 400 GeV/c. It is important to note that the momentum resolution of low-p_t muons for $|\eta| > 1.5$ is provided by the intermediate inner tracker. Although there is a distinct improvement in the Z mass resolution from air-core toroids for events in which one of the leptons goes into the intermediate angle region, we find that, with our present estimates of backgrounds, the reduced resolution does not prevent us from addressing any of our physics goals.

The second change is a rearrangement of the muon detectors, resulting from a better understanding of how to achieve the Level 1 and Level 2 triggers and optimize the detectors for muon identification and measurement. This rearrangement does not lead to any substantial cost savings, although the number of planes of muon detectors is slightly decreased.

Muon system layout

The basic structure of the muon detection system has not changed from that specified in the EoI, but the detailed layout of counters and chambers has been modified to reflect our clearer understanding of the function of each element.

Table 6
Calorimeter Performance and R&D Milestones in FY1991

		1991 J	F	M	A	M	J	J	A	S	O	N	D	1992 J
Simulation Studies of Performance Issues	pileup + trigger					X								
	e/h requirements						X							
	high luminosity requirements						X							
	electron & photon id requirements								X					
	forward calorimeter requirements								X					
Beam Tests & Engineering Design	LAr e/h in Pb-LAr						X							
	LAr preamps. in or out of LAr						X							
	LAr cryostat design						X							
	Scint. radiation hardness tests										X			
	Tile Fe compensation test							X						
	Tile uniformity tests							X						

The elements of the muon system are drift tubes, scintillation counters, and possibly gas Čerenkov counters in the intermediate region. The drift tubes are approximately 8 cm wide (4 cm maximum drift), except in the inner layers of the intermediate region, where they are 4 cm wide to allow for higher occupancy. Their maximum length is 8.3 m. The design of the tubes has not yet been decided, but they are likely to be similar to those now used by CDF[37] or D0[38] (without the second coordinate readout).

In the central region, the width of the scintillation counters is 15 cm/$\sin^2\theta$. In the endcap regions, the narrowest counters are 10 cm wide and the width scales as $\sin^{1.35}\theta$. These angular dependences are chosen to give a roughly uniform p_t resolution, taking account of both measurement and scattering errors[39]. The counters have a maximum length of 3 m, and a photomultiplier views each end. Both scintillator layers are presently positioned outboard of the toroids. We are studying the possible advantages of moving one layer inside the toroids.

We are also considering the use of gas Čerenkov counters in the forward direction, where the environment is likely to be hostile[40]. These counters are insensitive to muons that either have momenta less than 5 GeV/c or do not point to the interaction region within 50 mr. Beam tests of the effectiveness and efficiency of these counters will be conducted at Fermilab in early 1991.

Table 7 gives the basic layout and channel count. This arrangement tends to place muon detectors preferentially away from massive iron absorbers. This is beneficial because high-energy muons are often accompanied by soft electromagnetic debris at substantial angles to the muon trajectory. The additional lever arm allows the debris to separate transversely from the muon track so that it will be less often confused with the muon signals at either the trigger or pattern-recognition stage.

Design goals and performance

The muon detection system has five distinct goals, each of which puts different requirements on the design of the system. These five goals are the following:

1. To provide a Level 1 trigger;
2. To provide information for the Level 2 and Level 3 triggers;
3. To identify muons;
4. To improve the momentum resolution at very high muon transverse momenta;
5. To provide the capability of operation at luminosities above the design level.

In the following sections, we discuss each of these

Table 7

Layout and channel count for the muon system.

In the first column, WC stands for "wire chamber," SC stands for "scintillation counter," and CC stands for "Čerenkov counter." The coordinates are polar angle θ, azimuthal angle ϕ, and stereo projections s, s_1, s_2 (there are two stereo projections, as explained in the text, at intermediate angles). Furthermore, in the intermediate angle region, the third and fourth chamber layers and the first scintillator layer are split in z since only the region $|\eta| > 1.5$ is behind the 4 m thick iron toroid. Radial and z coordinates are given to the nearest 0.5 m— see Fig. 2 for more details.

Central Region					Intermediate Angle Region				
Layer #	Radius (m)	Coordinate	Layers	Channels (k)	Layer #	z (m)	Coordinate	Layers	Channels (k)
WC1	6.5	θ	6	12.1	WC1	8.0	θ	4	4.0
		ϕ	4	4.0					
		s	2	4.1					
WC2	9.0	θ	4	11.2	WC2	10.0	θ	4	5.2
							s_1, s_2	4	5.2
SC1	9.5	θ	1	2.5	SC1	13.0/16.0	θ	1	1.4
WC3	11.0	θ	6	18.6	WC3	12.5/15.5	θ	4	7.2
		ϕ	4	10.0					
		s	2	6.2					
					CC1	17.0	—	1	0.5
SC2	11.5	θ	1	2.5	SC2	16.0/18.0	θ	1	1.4
					WC4	15.5/17.5	θ	6	12.4
							s_1, s_2	4	8.2
Totals			28 WC	66.2 WC	Totals			26 WC	42.2 WC
			2 SC	5.0 SC				2 SC	2.8 SC
								1 CC	0.5 CC
Grand Total					Grand Total				108.4 WC 7.8 SC 0.5 CC

goals and the requirements they place on the muon system.

Level 1 trigger

The Level 1 trigger operates at the beam crossing rate of 60 MHz and must arrive at a decision in 2 μs. Thus it must be simple and fast, and still have the ability to reduce the accepted rate to a few tens of kHz. It is possible to do this with the muon system by triggering on a coincidence between two scintillator layers and a wire chamber trigger that is derived locally within one of the superlayers beyond the toroids.

The two layers of scintillators are arranged to be projective in θ with the center of a counter in one layer lining up with the division between two counters in the other layer for an infinite momentum trajectory. A suitable coincidence between counters defines the time bucket of the event and discriminates against low energy muons. The trigger efficiency of the scintillator counters as a function of muon transverse momentum is shown in Fig. 11.

The wire chamber trigger, which is in coincidence with the scintillator trigger, is similar to that used by CDF[41]. The wires in every other plane are projective to the interaction point. The time difference

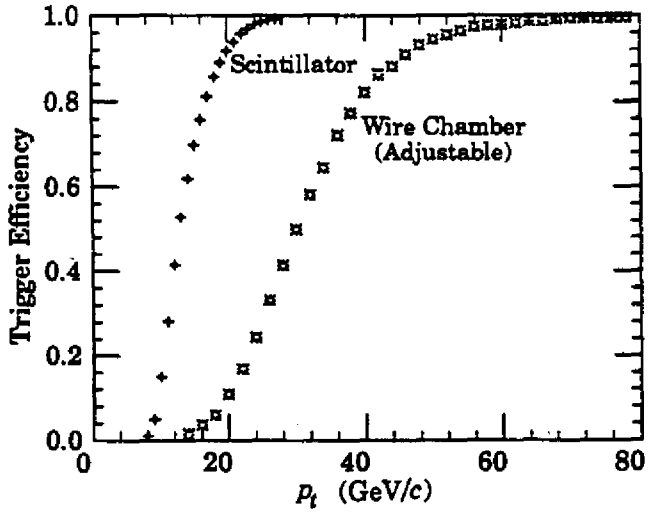

FIG. 11. First-level trigger efficiency of the muon system scintillator and wire chamber triggers. The wire chamber trigger threshold is adjustable. A typical setting is shown.

Δt between pulse arrivals on paired wires is then inversely proportional to the transverse momentum of the trajectory. A trigger threshold can be set on Δt by a simple circuit, whose deadtime is matched to the pulse pair resolution of the chambers. To void inefficiencies due to soft particles accompanying a high-momentum muon, a logical OR of triggers from the last two superlayers is employed. The wire chamber trigger has an adjustable threshold. A typical efficiency curve is shown in Fig. 11.

For transverse momentum trigger thresholds of interest at Level 1, namely 10–40 GeV/c, the resolution of the trigger is dominated by multiple Coulomb scattering in the calorimeter and toroids, and has an rms value of about 25%. Detailed calculations of the low-momentum rejection of this trigger for four and six θ layers within a superlayer are now being performed.

Level 2 and Level 3 triggers

The purpose of the Level 2 trigger is to reduce the trigger rate by sharpening the transverse momentum resolution. This is done by connecting a ϕ measurement in the muon system with a track-stub measurement in the inner tracker. In the absence of scattering, all valid trajectories beyond the flux return point to the interaction point in ϕ. By using projective ϕ wires, the simple circuit discussed above for the Level 1 trigger can be employed to find stiff tracks (*i.e.*, those that have not scattered more than expected) and to record the ϕ information for transmittal to the second-level trigger processor, where a match is made to the inner tracker information. At Level 2, a coincidence of detector octants containing a Level 1 θ trigger and a Level 2 ϕ trigger should be sufficient.

At the highest values of $|\eta|$, the Level 2 ϕ trigger is replaced by an angle-angle measurement in θ across the 4 m thick iron toroids. For this reason, an additional superlayer of θ planes is employed in the intermediate angle region.

The function of the Level 3 trigger is to insure that the lower-level triggers were valid and that they match. Stereo information is used in this process. At intermediate angles, stereo information is generated by simply rotating planes of θ wires by 15 and 30 degrees.

Identification of muons

The key to muon identification is the redundant momentum measurement based on the toroids. These measurements are multiple-scattering-limited at 18% in the central region and 10% in the intermediate region. They are accomplished by angle-angle measurements in θ across the toroids. For this reason, a set of six planes of θ wires, with a minimum of a 50 cm lever arm, have been added in the central region to the superlayer immediately in front of the toroids. No chambers beyond those required for the second-level trigger are required in the intermediate region.

Improved momentum measurements for very high momentum muons

In the central region, the highest precision measurement of muon momentum comes from a combination of ϕ measurements from the inner tracker and the muon system. This is because the effective sagitta measurement is made near the outer radius of the inner tracker, as illustrated in Fig. 12. The resolution for a 1 TeV/c muon at $\eta = 0$ is calculated to be 14%. Fig. 13 shows the expected muon resolution as a function of pseudorapidity for several muon transverse momenta.

Capabilities at higher-than-design luminosities

We believe that the proposed muon detector has enough resolution and redundancy to be capable of operation well above the design value of $10^{33}\,\mathrm{cm}^{-2}\mathrm{s}^{-1}$. At ten times design luminosity, we estimate that the rate of single hits per unit of pseudorapidity in the first layer of the muon system

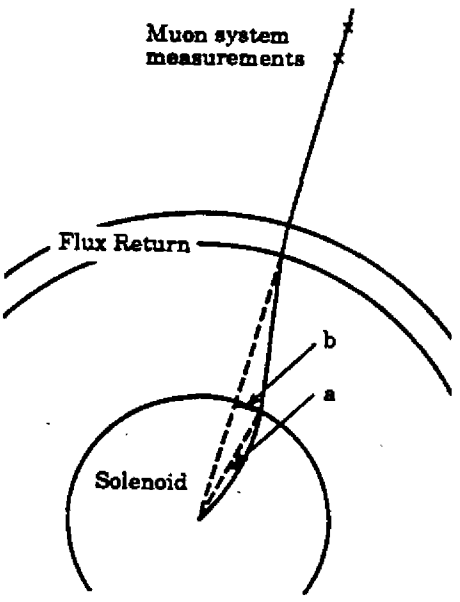

FIG. 12. Illustration of the reason for the improvement of momentum resolution coming from azimuthal measurements in the muon system. Without the muon system measurements, the sagitta is shown by a, whereas with the muon system measurements, the effective sagitta is shown by b. The curvature of a very low momentum track has been used for the purpose of illustration.

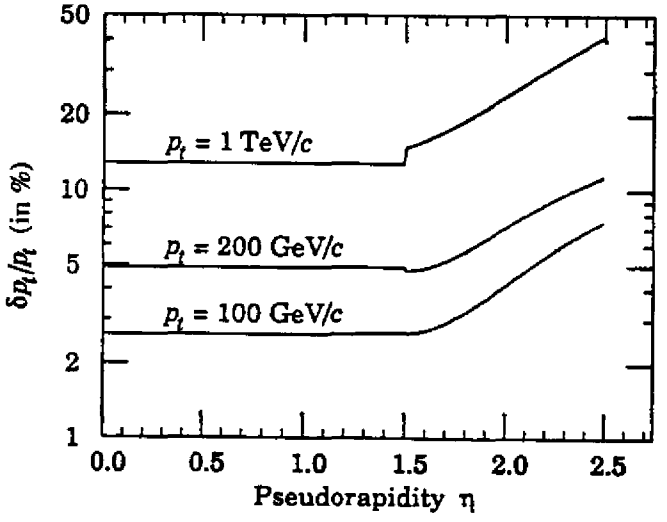

FIG. 13. Muon momentum resolution as a function of pseudorapidity for various values of transverse momentum. A resolution of 0.25 $(\text{TeV}/c)^{-1}$ from Table 1 is used to characterize the central tracking performance.

varies from about 1 MHz at $\eta = 0$ to 100 MHz at $\eta = 2.5$. This latter value corresponds to a 300 kHz rate in a 4 cm drift chamber cell, or an occupancy of 12% in the 400 ns time window set by the maximum drift time. The occupancies of cells at $\eta = 0$ will be about a factor of 50 less, indicating that the muon system will remain operational at very high luminosities. The momentum resolution obtained with just the muon system and the outer superlayer of the central tracker is shown in Fig. 14.

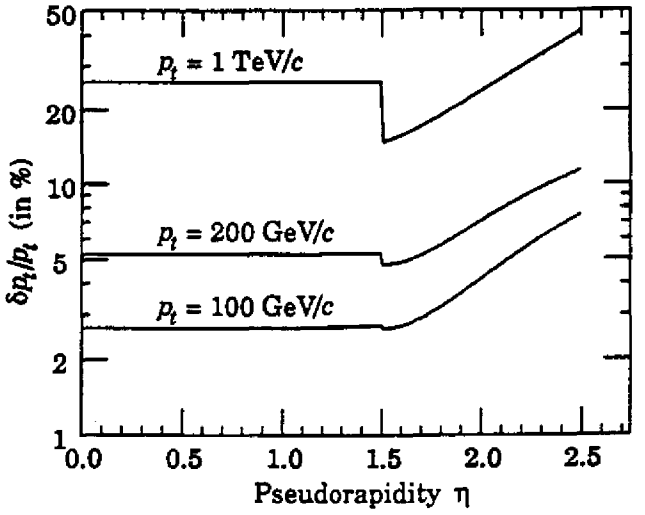

FIG. 14. Muon momentum resolution as a function of pseudorapidity for higher-than-design luminosity. It is assumed that the only operational tracking elements are the outer superlayer of the central tracker and the muon system.

Engineering progress

Work is underway on the design of the iron toroids and their assembly in the underground hall. A preliminary design, taking into account manufacturing feasibility in Japan, the United States, and the USSR will be completed and reviewed by March 1991. Detailed assembly scenarios will then be formulated by engineers at the University of Wisconsin (PSL), LBL, RTK, and the SSCL. Work has begun at Fermilab and PSL on chamber support and alignment.

Conceptual engineering design of chambers and trigger counters, and their supports will be completed by July 1991. Funds to support the engineering design of the muon system are requested in this LoI.

Table 8

The cost estimate given in Table 9 is based upon these parameters. An all-wire outer tracking system is assumed. The central calorimeter is scintillating tile with lead (about 7 interaction lengths) and iron (about 3 interaction lengths) absorbers (at 90 degrees). The calorimeter includes uninstrumented iron used for structural support, additional flux return and hadron absorber. Each muon trigger scintillator is assumed to have two phototubes (channels) and the total includes Čerenkov counters.

Silicon Tracker	
Number of channels - pixels	3.9×10^7
Number of channels - strips	8.5×10^6
Approx. area of silicon (m^2)	28
Central Straw-Tube Tracker	
Number of channels	188,000
Intermediate Wire Tracker	
Number of channels	50,000
Superconducting Solenoid	
Central field (Tesla)	2.0
Stored energy (MJ)	122
Central Calorimetry	
Tonnage (metric tons)	5300
Number of long. depth segments	4
Number of tower channels	41,000
Number of strip channels	25,000
Forward Calorimetry	
Total tonnage (metric tons)	750
Total number of channels	7,000
Muon System	
Barrel toroid tonnage (metric tons)	15,400
Total end-toroid tonnage (metric tons)	8,400
Number of wire chamber channels	108,400
Number of trigger counter channels	16,100

3.3. Cost estimate

In our Expression of Interest we presented an estimate of the detector cost based upon using unit costs developed by an SSCL Task Force. The cost estimate presented in the Expression of Interest was approximately \$630M (FY1990). If we apply these same costing rules to the "baseline" detector as described in Table 8, the cost would be about \$500M. The elimination of the air-core toroids, the reduction in the tracking volume, the reduction in scope of the tracking system and changes in other channel counts result in a very substantial reduction in cost, as estimated by this procedure.

The method of estimating costs used in the Expression of Interest yields only an approximate estimate of the actual detector cost. We have started the process of establishing a Work Breakdown Structure (WBS) for the SDC detector and have completed an initial "bottoms up" construction cost estimate within this structure for the detector parameters given in Table 8. The results are summarized in Table 9. The column labelled "base" refers to the cost of materials and labor to assemble components and subsystems. To this must be added the cost for engineering design, inspection and quality assurance (EDIA). The column labelled "cont" is our estimate of the contingency for each subsystem. Since we have been requested to essentially design to a fixed overall cost, the contingency factors reflect both our estimate of the uncertainty in actual cost and the uncertainty in scope we believe is allowable for each subsystem. Although we expect very substantial in-kind contributions from collaborators outside the United States, our estimate has not taken into account differences in accounting practices or labor rates in non-US countries.

Whenever possible we have used vendor quotes for major procurements (lead, silicon, electronics chips, etc.). If this was not possible, we have used costs from existing detectors (CDF, D0, etc.) to extrapolate to our design. Estimates of EDIA were generally made at the subassembly level, one to two levels below the summary shown in Table 9. All labor estimates were made in man-days and costs were computed using labor rates supplied by the SSC Laboratory. The estimated costs for Installation and Test (8.1) and Project Management (9) do not include contributions anticipated from the Experimental Facilities Support and Operations Groups at the SSC Laboratory.

In-kind contributions from collaborators outside the United States will represent a major fraction of the overall detector cost. The SDC is not now in a position to delineate precisely these contributions. Discussions are now underway within the collaboration, and we expect these to lead to agreements regarding in-kind contributions at the time of submitting a proposal or shortly thereafter. We expect in-

Table 9

SDC detector cost estimate in FY1990 dollars.

	BASE	EDIA	% EDIA	BASE + EDIA	CONT	% CONT	SUB TOTAL
1 TRACKING SYSTEMS							94.8
1.1 SILICON TRACKING SYSTEM	24.9	8.1	25%	33	6.6	20%	39.6
1.2 CENTRAL TRACKER	26.3	9.3	26%	35.6	8.3	23%	43.9
1.3 INTERMEDIATE TRACKER	6.7	2	23%	8.7	2.6	30%	11.3
2 CALORIMETRY							138.6
2.1 CENTRAL CALORIMETER	55.3	9.1	14%	64.4	15.8	25%	80.2
2.2 INTERMEDIATE CALORIMETER	25.5	4.8	16%	30.3	7.5	25%	37.8
2.3 FORWARD CALORIMETER	14	2.5	15%	16.5	4.1	25%	20.6
3 MUON SYSTEM							103.2
3.1 IRON TOROIDS	41.7	1.5	3%	43.2	6.5	15%	49.7
3.2 MUON CHAMBERS	28.6	2.6	8%	31.2	7.8	25%	39
3.3 MUON TRIGGER COUNTERS	11.8	0.8	6%	12.6	1.9	15%	14.5
4 SUPERCONDUCTING MAGNETS							29.8
4.1 SC SOLENOID	22.7	2.1	8%	24.8	5	20%	29.8
5 DATA ACQUISITION & TRIGGER							69.3
5.1 DATA ACQUISITION SYSTEMS	12.5	4.2	25%	16.7	4.2	25%	20.9
5.2 TRIGGER SYSTEMS	18.9	19.8	51%	38.7	9.7	25%	48.4
6 COMPUTING							11.9
6.1 ON-LINE COMPUTING	4.4	5.5	56%	9.9	2	20%	11.9
7 CONVENTIONAL SYSTEMS							20.6
7.1 UTILITIES	1.1	0.5	31%	1.6	0.3	19%	1.9
7.2 CONTROLS	2.3	2.1	48%	4.4	1.3	30%	5.7
7.3 SAFETY SYSTEMS	1.9	2	51%	3.9	1.2	31%	5.1
7.4 CRYOGENIC SYSTEMS	3	0.8	21%	3.8	1	26%	4.8
7.5 STRUCTURAL SUPPORT SYSTEMS	1.1	1.4	56%	2.5	0.6	24%	3.1
8 INSTALLATION AND TEST							28.1
8.1 TEST BEAM PROGRAM	6	1.5	20%	7.5	1.5	20%	9
8.2 SUBSYSTEM INSTALL. AND TEST	10	5.3	35%	15.3	3.8	25%	19.1
9 PROJECT MANAGEMENT							13.2
9.1 PROJECT PLANNING	0.4	0.9	69%	1.3	0.2	15%	1.5
9.2 PROJECT TRACKING	0.4	1	71%	1.4	0.2	14%	1.6
9.3 DOCUMENT DIST. AND CONTROL	0.7	0.5	42%	1.2	0.2	17%	1.4
9.4 SUBSYSTEMS INTEGRATION	1.8	5.8	76%	7.6	1.1	14%	8.7
TOTALS	322	94.1	23%	416.1	93.4	22%	509.5

kind contributions from non-US sources to be about forty percent of the equivalent total detector cost.

Off-line computing costs are not included in the total given in Table 9. By the time of the proposal we will have a detailed computing and networking plan, taking into account existing or potential resources within the collaboration. Substantial support will be needed from the SSCL. We request that about one-half of the computing resources available at the SSCL for physics research be devoted to the SDC.

We recognize that the cost estimate ($509M) presented here is preliminary. Much more work must be done over the next year or so to prepare a detailed proposal and a related cost estimate. Nevertheless we firmly believe that our preliminary estimate is the best that can be obtained today, and we are prepared to design a detector to meet this construction cost goal, assuming a completion date in late 1999.

4. Physics capabilities

.1. Parametrization of detector

In order to evaluate the detector performance in a uniform manner, we have used simple parametrizations of the detector response[42].

The calorimeter is segmented into projective towers of size $\Delta\phi \times \Delta\eta = 0.05 \times 0.05$ for $|\eta| < 3$ and 0.10×0.10 for $|\eta| > 3$. The electromagnetic calorimeter resolution in these studies is taken to be

$$\frac{\Delta E}{E} = \frac{0.15}{\sqrt{E}} \oplus 0.01 \ ,$$

where the energies are in GeV, and the symbol $\oplus$ means that the two terms are added in quadrature. The hadron calorimeter energy resolution is taken to be

$$\frac{\Delta E}{E} = \frac{0.50}{\sqrt{E}} \oplus 0.03 \quad (|\eta| < 3)$$
$$\frac{\Delta E}{E} = \frac{0.80}{\sqrt{E}} \oplus 0.05 \quad (3 < |\eta| < 5) \ ,$$

For hadron energy measurements, the effects of non-aussian tails are included using a parametrization eveloped by the CDF collaboration[43]. The degradation of resolution associated with coil support structures ($1.25 < |\eta| < 1.5$) is incorporated in the parametrization; at the worst point the resolution is degraded by a factor 1.7.

We assumed an η-dependent momentum resolution for the tracking system[42]. The resolution adopted here is about two times worse than that of Fig. 7, and represents the system performance that could be conservatively expected from the actual detector at design luminosity. The combined resolution for the tracking and muon systems is parametrized to be close to that displayed in Fig. 13, which also embodies a central tracking resolution about twice the level of Fig. 7[42].

In most plots in this section, there are far more Monte Carlo events than the number of events expected in a typical data run at the SSC. The error bars, however, correspond to the statistical errors on the expected numbers of events for the integrated luminosities defined in the figure labels, usually one "SSC year" of 10^4 pb^{-1}. We take the electron and ion efficiencies within the detector acceptance to be 85% for analyses requiring isolated leptons. This can be compared with CDF experience, where a value of $85 \pm 3\%$ is obtained for W and Z electrons, including the effects of triggering and mild isolation cuts[44]. In the case where the analysis requires two such leptons reconstructing to an on-shell Z boson, the lepton identification cuts are relaxed for the second lepton, and the efficiency for the second lepton is taken to be 95%.

4.2. Higgs

Describe the capabilities of your proposed detector for searching for a Standard Model Higgs in the following mass regions:

- $80 < M_H < 180\ GeV$
- $M_H \sim 200\ GeV$
- $M_H \sim 400\ GeV$
- $M_H \sim 800\ GeV$

In answering this question, we have assumed a top quark mass of 150 GeV, and have used the efficiencies and resolutions described in Section 4.1. The total Higgs production cross section can be found in Fig. 2 of the EoI. The branching ratios to different final states as functions of the Higgs mass are shown in Fig. 15, and include the effect of a running b quark mass which reduces $\Gamma(H \to b\bar{b})$ by a factor of 0.6[45]. For Higgs masses greater than about 125 GeV, we rely on the decay modes $H \to ZZ^*$ or $H \to ZZ$, where the Z^* or Z decay to electron or muon pairs. In the case of a very heavy Higgs, where the decay rate in this channel becomes small, we also exploit the decay $H \to ZZ \to \ell^+\ell^-\nu\bar{\nu}$. Below 125 GeV, the branching ratio and acceptance become too small to rely on the four-lepton mode, and we have investigated several alternate possibilities, which will be described later in this section.

The four-charged-lepton modes

In the four-lepton channel we require two trigger leptons with $p_t > 20$ GeV/c and $|\eta| < 2.5$. The other leptons are required to satisfy a p_t cut of 10 GeV/c. The backgrounds to $H \to ZZ$ fall into several classes. First, there is an irreducible continuum background arising from $q\bar{q} \to ZZ$ and $gg \to ZZ$. We neglect the contributions of nonresonant $qqWW \to qqZZ$ and $qqZZ \to qqZZ$ scattering, as they are less than 10% of the total continuum background in the regions relevant to this question[46]. The $gg \to ZZ$ calculation is complex and time-consuming; for purposes of this discussion, we multiply the result

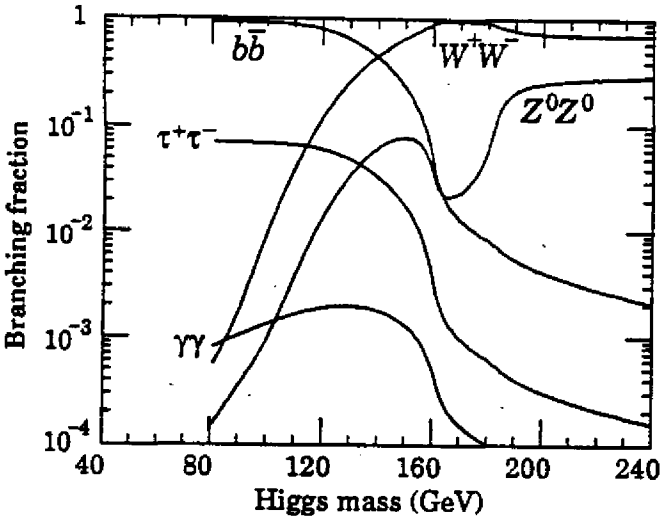

FIG. 15. The branching ratios of the Standard Model Higgs boson into various final states as functions of its mass.

for $q\bar{q} \to ZZ$ by a factor of 1.65 to approximate the combined contribution, following the work of Ref. 47.

There are additional backgrounds in which pairs of heavy quarks decay semi-leptonically to produce lepton signatures. The largest contribution comes from inclusive $t\bar{t}$ production, but backgrounds consisting of a Z and a heavy quark pair ($Z + b\bar{b}$ and $Z + t\bar{t}$) must also be considered. These backgrounds generally contain several nonisolated leptons, and can be controlled by an isolation cut limiting the additional calorimetric energy observed in a cone of radius $R = \sqrt{(\Delta\phi)^2 + (\Delta\eta)^2}$ around the lepton direction. The one exception is $Z+t\bar{t}$, which can produce four isolated leptons, but has a much smaller rate than $t\bar{t}$ or $Z + b\bar{b}$.

To understand the effects of requiring a limited amount of additional energy in a cone R around a lepton (lepton isolation cut), detailed simulations have been carried out for the dominant $t\bar{t}$ background, and for $H \to ZZ^*$ and $H \to ZZ$ signal events, using PYTHIA version 5.4. These simulations include the effects of shower spreading and the detector magnetic field. A distribution of minimum bias events appropriate for a luminosity of $10^{33}\,\mathrm{cm}^{-2}\mathrm{s}^{-1}$ has also been included. The computation of the excess transverse energy (E_t) in the cone includes the effect of an imperfect subtraction of the energy of the lepton itself. The results of this study indicate that a cut of $E_t < 5$ GeV in a cone of $R = 0.3$ provides a rejection factor of greater than 20 for leptons from b quarks (the rejection is p_t-dependent, falling to roughly 15 in the region $10 < p_t^\ell < 20$ GeV/c, but reaching values of greater than 100 for $p_t^\ell > 30$ GeV/c). The rejection is at least a factor of 100 for leptons from c or lighter quarks, while maintaining an efficiency of 95% for each signal lepton at SSC design luminosity. To simplify the subsequent analysis, we conservatively assume that our isolation cut reduces the number of background leptons coming from b or lighter quarks by a factor 10 per lepton[46]. Further study is continuing to optimize this cut as a function of luminosity and to include signal shaping effects in the modeling of the calorimeter readout[48], but there appears to be no particular obstacle to achieving the assumed rejection at luminosities approaching $10^{34}\,\mathrm{cm}^{-2}\mathrm{s}^{-1}$ with the standard calorimeter segmentation.

The heavy flavor backgrounds also produce like-sign lepton pairs, which are suppressed by use of the lepton charge information available in a magnetic detector. This provides an additional reduction of roughly a factor of 2 for $t\bar{t}$ backgrounds, and roughly a factor of 1.5 for $Z + b\bar{b}$ and $Z + t\bar{t}$ backgrounds. Finally, although it has not proved necessary in the current analysis, it is also possible to include an anti-b tag by rejecting events with large impact-parameter tracks found in the inner tracking system, thereby reducing the heavy flavor backgrounds still further.

The four-lepton signals, and their estimated backgrounds, are shown in Figs. 16–19. The $4e$, 4μ, and $2e2\mu$ final states have been combined since they have similar overall resolutions[46]. The global efficiency described in Section 4.1 has been applied to each lepton in addition to the lepton isolation efficiency defined above. In all cases, the charge-zero lepton pair with mass closest to M_Z has been chosen as the primary Z, and a requirement of $M_{\ell\ell} = M_Z \pm 10$ GeV has been imposed.

For the $H \to ZZ^*$ case, the other lepton pair is required to have $M_{\ell\ell} > 20$ GeV to remove $q\bar{q} \to Z\gamma^* \to \ell^+\ell^-\ell^+\ell^-$ background, and the kinematic quantities for both electrons and muons are derived from the tracking information. Note that the electron measurements suffer the complication of relatively large bremsstrahlung energy losses in the inner detector, but the resolution is improved ($\sigma(M_{ZZ^*}) = 1.0$ GeV instead of 1.3 GeV for $M_H = 140$ GeV) over that found for a calorimetric measurement.

For the heavier $H \to ZZ$ cases, both lepton pairs are required to satisfy a requirement of $M_{\ell\ell} =$

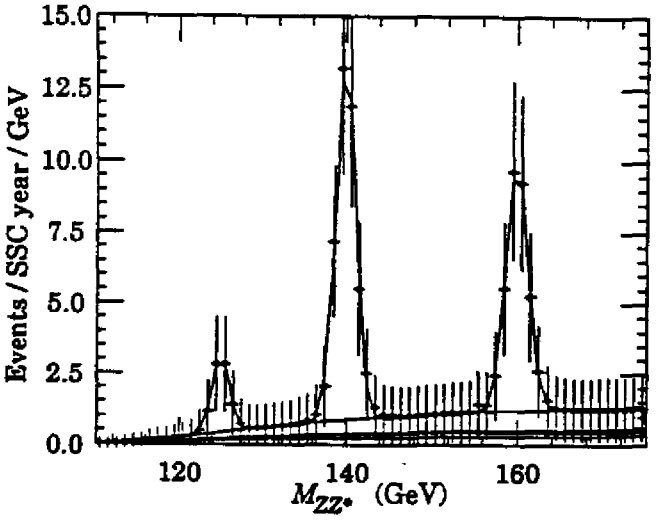

FIG. 16. The reconstructed Higgs mass for ZZ^* decaying to $4e$, 4μ, and $2e2\mu$ with $M_H = 125, 140, 160$ GeV, including the expected backgrounds. The backgrounds are indicated by a series of curves, each one representing a cumulative sum, so that the area between two curves corresponds to the relevant background contribution. The lowest curve is $q\bar{q} \rightarrow ZZ^*$, which has been multiplied by 1.65 to account for $gg \rightarrow ZZ^*$. Next are the heavy flavor backgrounds $Z + b\bar{b}$ and $Z + t\bar{t}$. The final curve includes the dominant $t\bar{t}$ contribution. Two trigger leptons with $p_t > 20$ GeV/c and two other leptons with $p_t > 10$ GeV/c were required. All leptons are isolated by requiring $E_t < 5$ GeV in a cone of radius 0.3. In addition, one pair of leptons is required to have $M_{\ell\ell} = M_Z \pm 10$ GeV and the other $M_{\ell\ell} > 20$ GeV.

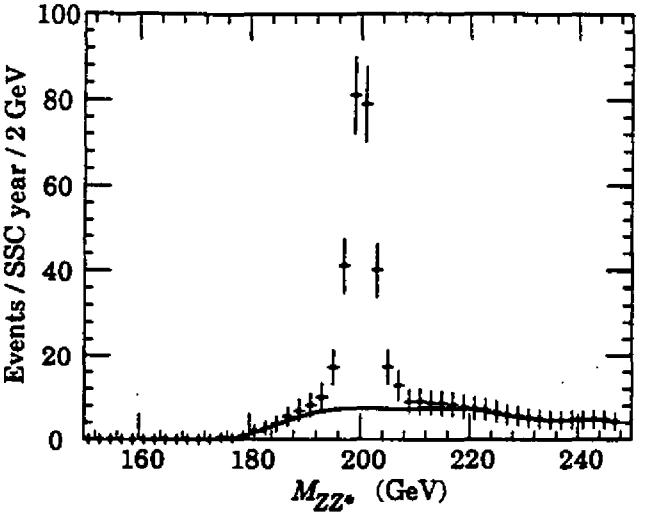

FIG. 17. The reconstructed ZZ mass for the final states $4e$, 4μ, and $2e2\mu$ showing the peak due to a Higgs of mass 200 GeV. The two lepton pairs were both required to have $M_{\ell\ell} = M_Z \pm 10$ GeV. The background curves have the same significance as those of Fig. 16, but the ZZ background gives the only visible contribution.

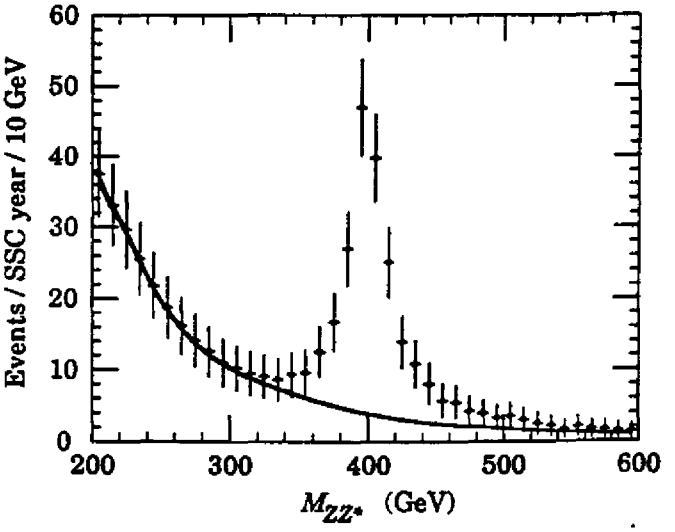

FIG. 18. Same as Fig. 17 except that the Higgs mass is 400 GeV.

$M_Z \pm 10$ GeV, and the electron energy measurements are derived from the calorimetry. Even for the $M_H = 800$ GeV case, the muon resolution for the Z peaks is adequate, resulting in a negligible loss of signal events outside the ± 10 GeV mass window[46].

The significance of the observed signals has been evaluated by counting the number of events expected above the predicted backgrounds in the vicinity of the peak. The $M_H = 140$ GeV and $M_H = 160$ GeV peaks are unambiguous. There are 38 events with 3.5 expected background, and 30 events with 5 expected background, respectively, for a single year of SSC running at nominal luminosity. The $M_H = 125$ GeV peak has a signal of only 8 events with 2 expected background, and consequently requires about 2 years of SSC running at nominal luminosity to establish a convincing signal. For $M_H = 200$ GeV and $M_H = 400$ GeV, the signals are clear, and sufficient for discovery. In the case of a Higgs of mass 800 GeV, there are fewer signal events and no clear peak. The signal-to-background ratio can be improved by requiring that both of the Z's have $p_t(Z) > 200$ GeV/c. As is evident in Fig. 20, the background has been reduced with little loss in signal. The peak region contains 20 events with 6 expected background. To claim a signal, we must be confident that the ZZ rate expected at large ZZ invariant mass in

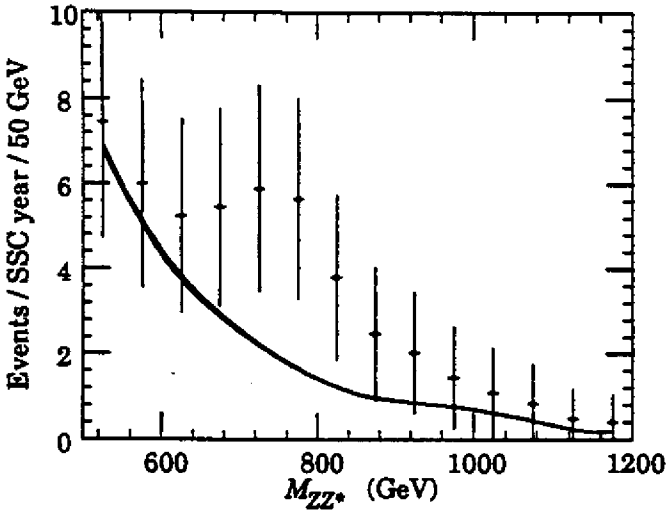

FIG. 19. Same as Fig. 17 except that the Higgs mass is 800 GeV.

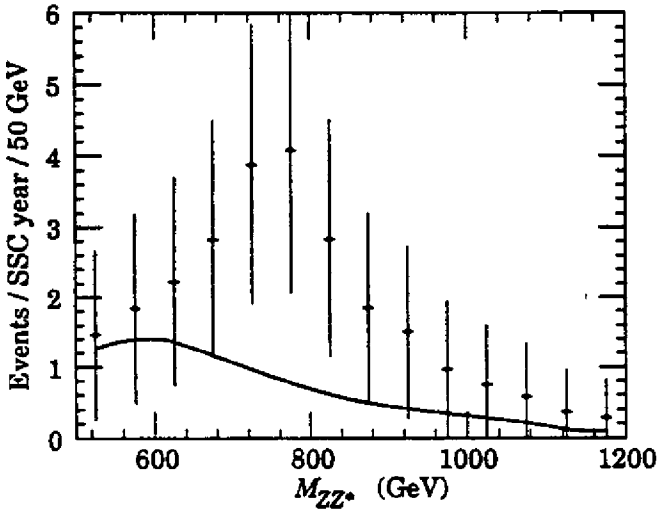

FIG. 20. Same as Fig. 19 except that both Z's were required to satisfy $p_t(Z) > 200$ GeV/c.

the absence of a Higgs boson can be accurately predicted. The measured ZZ rate at lower invariant masses can be used to reduce the uncertainties in the theoretical predictions for the rate at large values of the invariant mass. The major uncertainties in this extrapolation arise from the structure functions and higher order QCD effects[49]. We estimate that we can determine the background with an uncertainty of 20%, and therefore the $M_H = 800$ GeV signal would require 2–3 years of SSC running at the nominal luminosity to be sufficient for discovery.

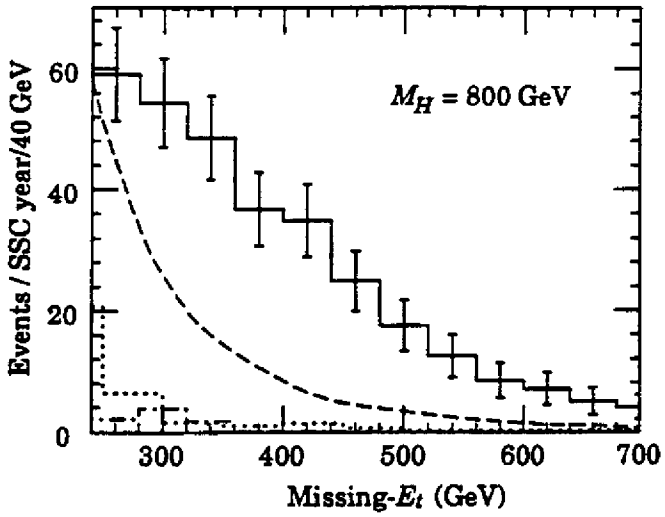

FIG. 21. The distribution in missing-E_t for the final state $Z(\rightarrow e^+e^-, \mu^+\mu^-)$ + missing-E_t, including the effect of a Higgs boson of 800 GeV, where $H \rightarrow ZZ \rightarrow \ell^+\ell^-\nu\bar{\nu}$ (solid). The reconstructed Z is required to have $p_t(Z) > 250$ GeV/c. The background shown as a dashed curve arises from $q\bar{q} \rightarrow ZZ$ (multiplied by 1.65). The dot-dashed histogram arises from the final state Z+*jets*, where the missing-E_t is generated by calorimeter resolution and energy loss out of the end of the detector ($|\eta| > 5$). The dotted histogram arises from the final state $t\bar{t}$, where there is an e^+e^- or $\mu^+\mu^-$ pair of mass $M_Z \pm 20$ GeV and the missing-E_t is due to neutrinos. The events are rejected if they contain a jet with $E_t > 300$ GeV.

The two-lepton two-neutrino mode

In view of the limited four-lepton rate at $M_H = 800$ GeV, we have looked at the channel with e^+e^- or $\mu^+\mu^-$ and missing-E_t in order to extract the signal from the decay $H \rightarrow ZZ \rightarrow \ell^+\ell^-\nu\bar{\nu}$, which contains six times as many events. Figure 21 shows the missing-E_t distribution accompanying a reconstructed Z with $p_t(Z) > 250$ GeV/c. This analysis is similar to that in the EoI, except that here the mass of the Higgs is taken to be 800 GeV[46]. The strategy for extracting a signal is similar to that for the high-mass Higgs in the four charged lepton state, but the lack of a second dilepton mass cut requires a more careful background analysis. Measurements of the four-lepton channel, and of the missing-E_t spectrum recoiling against a Z at lower values of missing-E_t, are used to reduce the uncertainties in the predicted missing-E_t spectrum at larger missing-E_t values in the absence of a Higgs boson. The observed excess of events, in conjunction with the four charged lepton results, would be

sufficient to establish the existence of the Higgs. At higher luminosities, the high radiation flux near $|\eta| =$ may disable this region of the forward calorimetry. In this case, our strategy would be to reduce the forward calorimeter coverage to $|\eta| < 4$. Even this coverage provides excellent rejection against the $Z +$ *jets* background[46] for the large values of missing-E_t present for $M_H = 800$ GeV (for missing-$E_t > 320$ GeV, there would be 2200 signal and 650 background events for a data sample of 10^5 pb^{-1}).

The search for $M_H < 125$ GeV

As is evident in Fig. 16, the signal for $H \rightarrow ZZ^* \rightarrow \ell^+\ell^-\ell^+\ell^-$ is rapidly becoming undetectable for M_H below 125 GeV. To extend the Higgs search to lower masses, we have explored four other possibilities.

The first is the rare decay $H \rightarrow \gamma\gamma$. The electromagnetic resolution assumed in the EoI is somewhat worse than that of the "excellent resolution" case discussed in the 1988 Snowmass study[50] of the decay $H \rightarrow \gamma\gamma$. The conclusions of that study indicate that, with this resolution, this mode will not allow the SDC to extend its range of sensitivity below that already covered by the $H \rightarrow ZZ^*$ search.

A second mode involves $W + H$ production with the subsequent decay $H \rightarrow b\bar{b}$. Previous analysis[51] found a signal-to-background ratio of 0.2 with 20 events per SSC year (for $M_H = 125$ GeV and $M_{\rm top} = 150$ GeV), but neglected the $t\bar{t}$ background. This background has been investigated at the parton level[52]. Smearing effects produced by hadronization cause the small signal to be overwhelmed by background (signal-to-background ratio less than 0.1 with a signal of 10 events per SSC year). Similarly, the final state $H +$ *jets* followed by $H \rightarrow \tau\tau$ was investigated and found to suffer from overwhelming background. In addition, neither of these channels is effective for the case $M_H \sim M_Z$, due to the large $Z \rightarrow b\bar{b}$ and $Z \rightarrow \tau\tau$ backgrounds.

Finally, we have considered $W + H$ production followed by the decay $H \rightarrow \gamma\gamma$. The event rates are very low, but less stringent resolution in the $\gamma\gamma$ invariant mass is required in this final state, compared to the direct $H \rightarrow \gamma\gamma$ case. The dominant backgrounds arise from the final states $W + \gamma\gamma$, $W + \gamma +$ *jet*, and $W +$ *jets*, where the jets fragment in such a way that they look like isolated photons. To estimate the jet backgrounds, we have multiplied the jet rate by a factor of 5×10^{-4} per jet to account for the probability that a jet fragments to a leading π^0 that carries almost all of the energy of the jet. The correct value for this number will not be known until it can be measured at the SSC. Here we have used a number consistent with the following CDF measurements :

- For dijet events with invariant mass in the range 80 GeV $< M_{jj} <$ 140 GeV, a one sigma upper limit on the integrated fragmentation function for $z > 0.8$ is 1.4×10^{-3}[53]. (The effects of finite momentum resolution and systematics of jet energy corrections make this a limit rather than a measurement).
- In the transverse momentum range 27 GeV/$c <$ $p_t <$ 35 GeV/c, the ratio of the isolated π^0 cross section to the jet cross section is $\sim 5 \times 10^{-4}$[54]. Here isolation means less than 15% additional energy in a cone of size $\sqrt{(\Delta\eta)^2 + (\Delta\phi)^2} = 0.7$ centered on the π^0.

We note that the fragmentation function at large z should decrease with increasing jet E_t, and thus the CDF estimate should be taken as an upper bound.

Additional backgrounds may arise from several sources. We have considered the processes $b + \gamma\gamma$, $b + \gamma +$ *jet*, and $b\bar{b} + \gamma$, where the b decays into a hard lepton. We have also considered QCD jet production via the processes 3-*jets*, 2-*jets* $+ \gamma$, and *jet* $+ \gamma\gamma$, where the jets are misidentified as either photons or leptons[55]. The probability for misidentifying a jet as a lepton was taken to be 1×10^{-4}, where an additional rejection of five for either single charged hadrons or conversions from single π^0's is assumed relative to the rejection for misidentifying a jet as a photon.

Our analysis requires an electron or a muon plus two photons. Each must satisfy $p_t > 20$ GeV/c, and the isolation requirement of $E_t < 5$ GeV in a cone of radius 0.3. The photons and lepton were required to be separated in η–ϕ space by 0.4. We have studied the backgrounds described above, and superimposed the expected Higgs signals in the mass region 80 to 140 GeV[55]. The b momentum was smeared by a Peterson fragmentation function, and, as discussed for the four lepton case, an isolation rejection factor of 10 was assumed for each b. The results are displayed in Fig. 22, and it is clear that this technique would be sensitive to a Higgs in the mass region 80 to 140 GeV, provided that a data sample of the required size (10^5 pb^{-1}, corresponding to three years of running at three times the nominal

SSC luminosity) could be accumulated. In this figure, the significance of the peaks varies from four to five standard deviations.

Conclusions

The SDC detector can discover a Standard Model Higgs in the region $125 < M_H < 800$ GeV using the $4e$, 4μ, or $2e2\mu$ channels for $H \to ZZ$ or $H \to ZZ^*$. At the lower end of this range, the signal is statistics limited, and will require slightly more than one year of running at SSC nominal luminosity. At the upper end of the range, the four-lepton signal, in conjunction with the higher rate process $H \to \ell^+\ell^-\nu\bar{\nu}$, will provide a substantial signal. The region $80 < M_H < 125$ GeV will be covered by using the process $W + H$ followed by $H \to \gamma\gamma$. Here, the cross section is small, and approximately 3 years of SSC running at three times the nominal luminosity are required for discovery.

4.3. Top quark with mass 250 GeV

Assume a top quark with a mass of 250 GeV.

- *How is it discovered in your detector;*
- *How accurately could the mass be measured;*
- *Can the decay properties be determined? For example, if the top decays to a charged Higgs with a mass of 150 GeV, at what branching ratio level can this process be detected?*

We have examined three methods for discovering a top quark and measuring its mass. The first method, using isolated $e - \mu$ pairs, has been discussed in the EoI (see Fig. 34 of the EoI which shows the cases $M_{\rm top} = 150$ GeV and $M_{\rm top} = 250$ GeV)[56]. It can be seen from this plot that there is essentially no background for these cases. In the Standard Model, the top branching ratios are known, and a measurement of the production cross section in the isolated $e\mu$ mode can be used to determine the mass. The current theoretical uncertainty of 30% on the production cross section[57] implies that the smallest achievable error on $M_{\rm top}$ using this method is ~ 20 GeV. Moreover, if there are nonstandard decays of the top quark, such as the decay into a charged Higgs, $t \to H^+b$, the correlation between rate and mass is altered, and this method may not yield a reliable mass measurement.

Here, we discuss two more precise methods, and then address the question of nonstandard decays of the top quark.

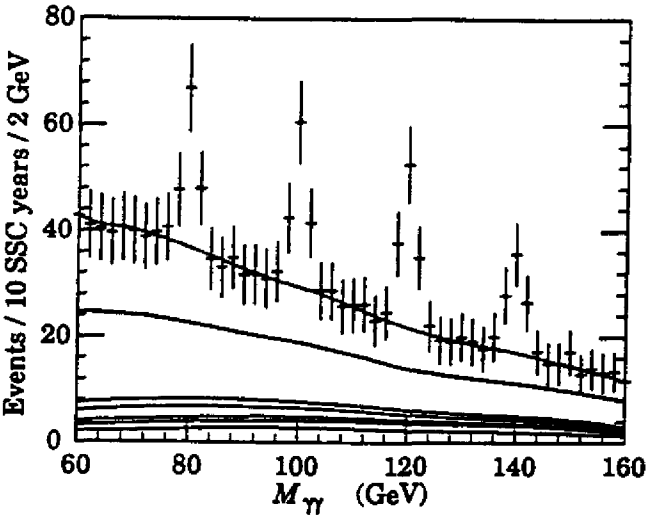

FIG. 22. The $\gamma\gamma$ invariant mass distribution for the process $W + H \to \ell\nu\gamma\gamma$, including all backgrounds. The signal contains peaks from $M_H = 80, 100, 120, 140$ GeV. The lepton and photons were all required to satisfy $p_t > 20$ GeV/c, and to be separated in η–ϕ space by a distance of 0.4. A jet misidentification probability of 5×10^{-4} was assumed in plotting the QCD backgrounds. An isolation cut reduces the b backgrounds by a factor 10. The background curves are cumulative, and are (from lowest to highest): $3 - jet$, $2 - jet + \gamma$, $jet + \gamma\gamma$ combined, then $b + \gamma\gamma$, $b + \gamma + jet$, $b\bar{b} + \gamma$, followed by $W + jets$, $W + \gamma + jet$ and $W + \gamma\gamma$.

The Lepton + Jets Mode

The second method of discovering the top quark is to look for events with one isolated lepton and many jets, arising from the process $t\bar{t} \to WWb\bar{b} \to \ell\nu jjb\bar{b}$. We discuss a determination of the top quark mass by reconstruction of the top quark decay into three jets, which is similar to that presented in the SDC EoI. We focus on those decays where the other top quark decays semi-leptonically yielding an isolated lepton and an energetic neutrino. Two independent Monte Carlo studies have been performed and find similar results (see Ref. 58 and Ref. 59).

The study discussed here was performed using ISAJET version 6.24 to generate $t\bar{t}$ events. The analysis is sensitive to effects due to jet clustering and shower overlap. To take these into account, we simulate the SDC detector response with a full shower Monte Carlo that includes the calorimeter response and tower segmentation[60]. We define electromagnetic and jet clusters using algorithms based

on the observed energies in the calorimeter towers. Jet clustering is performed using a fixed-cone clustering algorithm with a cone radius of $R = 0.4$. A seed tower with $E_t > 2.0$ GeV is required, and a single tower threshold of 0.1 GeV is used for computing the energy inside the cone.

We require the candidate events to have a well-isolated electron or muon with $p_t > 40$ GeV/c and missing-$E_t > 20$ GeV to select those events with at least one $W \to \ell\nu_\ell$ decay. In the following analysis we confine ourselves to the $e + jets$ final state, but the corresponding analysis with muons would be almost identical and would double the rates. Although the missing-E_t resolution in a typical event is 10–20 GeV, this cut provides some rejection against $b\bar{b}$ backgrounds. Events in which the other W decays hadronically are expected to have at least four jets, two from the W decay and one each from the b and $\bar{b}$ quarks. We therefore require the events to have at least four jets with $E_t > 30$ GeV and $|\eta| < 2.0$. This initial selection results in 566,000 events per SSC year for the $e + jets$ final state, assuming the ISAJET $t\bar{t}$ cross section of 1.54 nb.

The primary background to this channel arises from QCD production of W bosons with associated jets. We reduce this background by requiring that at least two of the jets satisfying the kinematic cuts are tagged as b quark candidates using the presence of large impact-parameter tracks in the transverse plane as discussed in Ref. 61. This cut retains $\sim 10\%$ of the signal events, and leaves an estimated background from $W + jets$ production that is less than 0.1% of the signal. We then take all pair combinations of the jets in the event which do not contain b quark candidates and form dijet systems from them.

The resulting invariant mass spectrum for these dijet combinations is shown in Fig. 23, where we have added the requirement that the p_t of the resulting dijet system be greater than 180 GeV/c to reduce the combinatorial background. One sees a clear W signal above a relatively small background. In this plot, there are 9500 signal events per SSC year above a combinatorial background that is less than half of the signal in the dijet invariant mass region between 50 and 95 GeV. The hard p_t cut on the dijet system retains approximately 37% of the correctly reconstructed signal events and reduces the combinatorial background by a factor of 8.

The W mass determination depends on effects resulting from the jet clustering (loss of energy out of the cone or below the calorimeter tower threshold), and from overlap of parton showers with each other and with the underlying event. We have employed a relatively small cone size in this analysis ($R = 0.4$) to optimize the reconstruction efficiency of the two jets arising from the W decay. We have also performed the analysis using cone sizes up to $R = 0.8$ and have found that the reconstruction efficiency falls with increasing cone size with very modest improvements in the W mass resolution. We have also considered the effect of more stringent cuts on the jets (*e.g.* raising the jet E_t thresholds or reducing the η interval) and have found that they provide relatively modest improvements in the overall signal-to-noise and mass resolution with considerable reductions in signal rate.

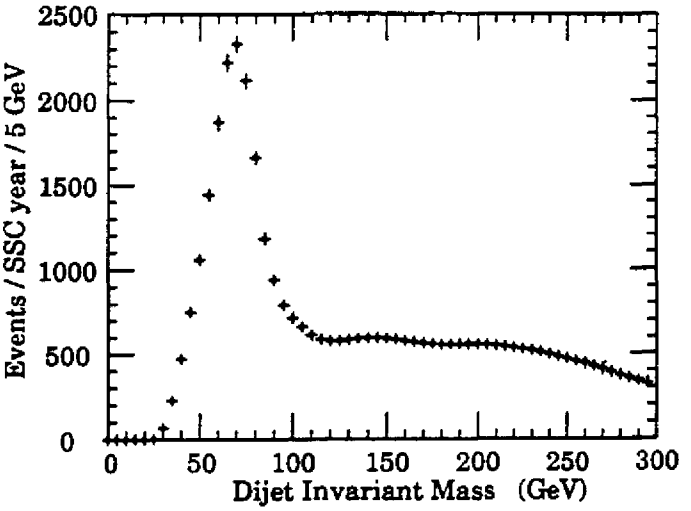

FIG. 23. The dijet invariant mass distribution for all combinations of two jets in $t\bar{t}$ events, where the dijet system was required to have $p_t > 180$ GeV/c. The events have an electron with $p_t > 40$ GeV, missing-$E_t > 20$ GeV, 4 jets with $p_t > 30$ GeV, and at least two tagged b quark jets. The tagged b jets are excluded when forming the dijet combinations.

We define a W candidate to be any dijet combination (excluding tagged b jets) that has an invariant mass between 50 and 95 GeV and $p_t > 180$ GeV/c. We pair these W candidates with each of the tagged b jets to form the three-jet invariant mass distribution shown in Fig. 24. An impressive top signal is seen above a combinatorial background that is relatively flat and slowly changing under the signal peak.

The statistical uncertainty in the estimated mean of the signal peak is ~ 0.4 GeV. However, our knowledge of the jet energy scale is likely to be the largest

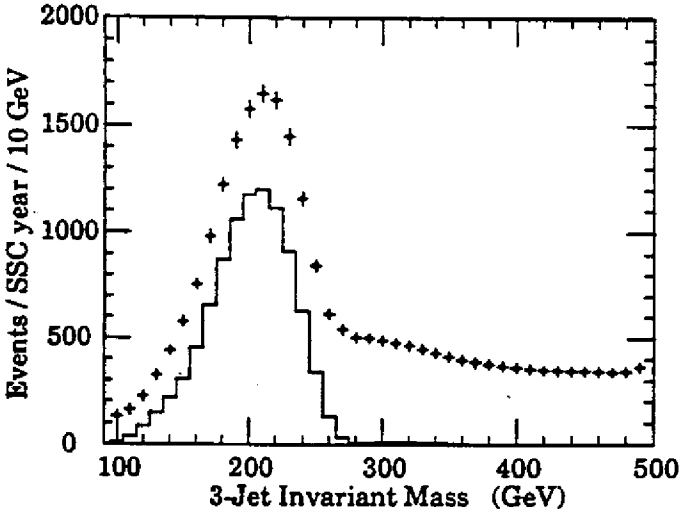

FIG. 24. The three-jet invariant mass distribution for all events with a W candidate having dijet invariant mass between 50 GeV and 95 GeV with $p_t > 180$ GeV/c, where we have only considered the three-jet systems formed from each of the tagged b jets and the W candidate. The solid curve shows only the correct combination of the W and b jets.

source of uncertainty in the top mass determination[58]. We can reduce this uncertainty by making use of the *in situ* calibration provided by the W peak in the dijet invariant mass distribution, which can be determined to a statistical uncertainty of ~ 0.15 GeV. We then use this constraint on the dijet mass, event by event, to calibrate the momentum of the W candidate. A 2% systematic error in this mass constraint would lead to a top mass uncertainty of ~ 1.2 GeV. We must also calibrate the b quark energy scale, which differs from that of the light quarks because of the b quark fragmentation. We therefore assume that there is an additional uncertainty of 3% in the b quark energy scale contributing a top mass uncertainty of ~ 2 GeV. Other effects, such as uncertainties arising from the jet clustering algorithm and event pileup are estimated to create an additional uncertainty of ~ 1.5 GeV. Combining all of these contributions in quadrature, we estimate the total uncertainty on the top quark mass to be ~ 3 GeV. We expect nonperturbative QCD corrections to the top quark mass measurement (i.e., top quark fragmentation) to be small because a top quark of this mass will decay before it hadronizes. Perturbative QCD corrections (*e.g.* gluon bremsstrahlung) are an additional source of uncertainty, but we expect that they will also be smaller than the experimental uncertainties discussed above.

The Sequential $e\mu$ Mode

A third method for measuring the top quark mass relies on events with one isolated electron (from top decay) and one nonisolated muon of opposite sign (from the b-decay product of the same top)[62]. We require the electron to have $p_t > 40$ GeV/c and to have additional $E_t < 4$ GeV in a cone of radius $R = 0.2$ around the electron direction. The muon must have $p_t > 20$ GeV/c and have additional $E_t > 20$ GeV in a cone of radius $R = 0.4$ around the muon direction. Furthermore, the azimuthal distance between the electron and the muon, $\Delta\phi$, must be less than 80° to maximize the probability that the e and μ come from the same top quark. Finally, we require $p_t(e\mu) > 120$ GeV/c to increase the sensitivity to the top mass.

Figure 25 shows the invariant mass of the $e-\mu$ pair, $M(e\mu)$, for top masses of 220 GeV and 250 GeV with the above cuts. The events from the higher top mass peak at a higher $M(e\mu)$. Fig. 26 shows the mean invariant mass of the $e-\mu$ pair as a function of the top mass for several values of the $p_t(e\mu)$ cut. The mean $M(e\mu)$ has an approximately linear dependence on the top mass and the sensitivity (the slope) increases with the $p_t(e\mu)$ cut. A p_t cut of 120 GeV/c gives adequate sensitivity while retaining sufficient statistics for a good mass determination. In one year of running at nominal SSC luminosity, we expect 17,000 events of this type, providing a measurement of the top mass with a statistical error of ± 1 GeV. Backgrounds from other processes are very small. We have considered WW, $Z \to \tau\tau$, and $W+b\bar{b}$ production. Only the latter is a non-negligible source of isolated electrons and nonisolated muons. Using ISAJET, we find that this process contributes a 3% background to the $M(e\mu)$ plot.

The systematic error on the top mass using this method is dominated by uncertainties in the physics inputs. The first is the incomplete knowledge of the b fragmentation function which controls the muon momentum distribution. We use the Peterson fragmentation parametrization for heavy quarks with the value for the ϵ parameter measured by ALEPH [63]. Varying ϵ by one standard deviation, we obtain a ± 3 GeV variation in the top mass. The second uncertainty is the imprecise knowledge of the top p_t distribution. For example, different top p_t spectra are expected for processes not considered here, such as $W+t$ production or $t\bar{t}$ pair production from

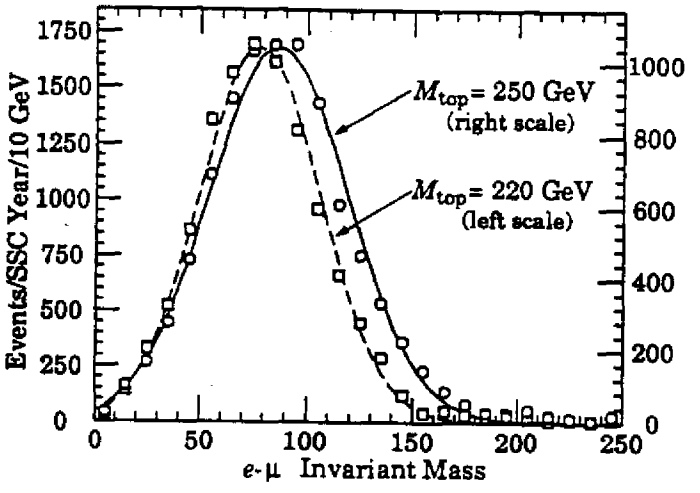

FIG. 25. The invariant mass distribution for the $e-\mu$ pair, $M(e\mu)$, for two different top masses. The lefthand scale and the leftmost curve are for $M_{top} = 220$ GeV, while the righthand scale and the other curve are for $M_{top} = 250$ GeV. The cut $p_t(e\mu) > 120$ GeV/c has been used. The superimposed curves represent Gaussian fits.

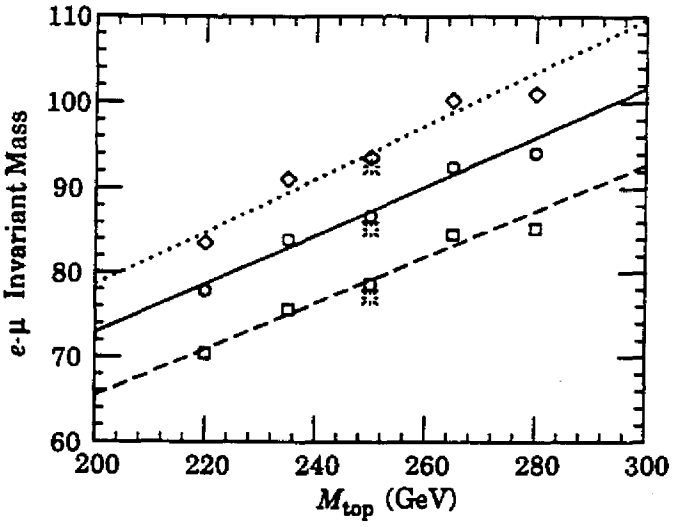

FIG. 26. The invariant mass of the $e-\mu$ pair as a function of the top mass for $p_t(e\mu) > 80$ GeV/c (lower curve), $p_t(e\mu) > 120$ GeV/c, and $p_t(e\mu) > 160$ GeV/c (upper curve). The plotted points represent the fitted mean and its error, derived from Gaussian fits to distributions such as those shown in Fig. 25. The three additional points at 250 GeV correspond to one standard deviation variations in the b fragmentation as measured by ALEPH[63].

gluon splitting. The dependence of $M(e\mu)$ on the top p_t has been studied by reducing the initial state radiation generated by ISAJET, thus obtaining a softer p_t distribution for the top quark. From this variation in the p_t distribution, we derive an uncertainty on the top mass of ±5 GeV. Both of these systematic uncertainties may be reduced after detailed studies of the data from the SSC. Adding all the uncertainties in quadrature we expect to determine the top mass at 250 GeV with an uncertainty of ±1 (stat) ± 6 (syst) GeV for a run of one year at the SSC design luminosity.

The Top Quark Decay Properties

We can determine the relative top quark decay rates to $t \to e\nu_e b$, $t \to \mu\nu_\mu b$ and $t \to q\bar{q}'b$ by comparing the rate for events having an isolated electron and an isolated muon with the rate for events with an isolated electron or muon, two tagged b quark jets and a W boson reconstructed in the dijet final state. We can measure these rates to ~ 1% in one year of SSC operation, and hence can measure the relative branching fractions of the top quark into these three final states with a statistical accuracy of 2%. We expect the systematic errors in this measurement to come from the uncertainty in the lepton and jet reconstruction efficiencies; experience at present hadron colliders indicates that these can be determined to within a few percent[64]. The rate of top quark decays into the $\tau\nu_\tau b$ final state relative to the electron and muon decay modes can be determined by reconstructing the τ decay modes as described below. This would result in a measurement of the relative decay rate into $\tau\nu_\tau b$ with a statistical accuracy of 7%. The absolute branching ratios cannot be determined to better than the uncertainty of the top quark cross section, which is estimated to be of order 30%.

The best way to determine if the top quark has nonstandard decays is to search for them directly. One of the most attractive extensions of the standard Higgs sector contains two Higgs doublets with charged and neutral Higgs bosons[65]. If the charged Higgs boson is lighter than the top quark, the branching ratio for the decay $t \to H^+b$ could be comparable to that for $t \to W^+b$. These branching ratios depend on the couplings of the two Higgs doublets to the quarks and leptons. There are two possible models normally considered for these couplings consistent with the absence of flavor changing neutral currents. In one model (Model-II in the notation of Ref. 65) the neutral component of one of the doublets is responsible for generating the mass

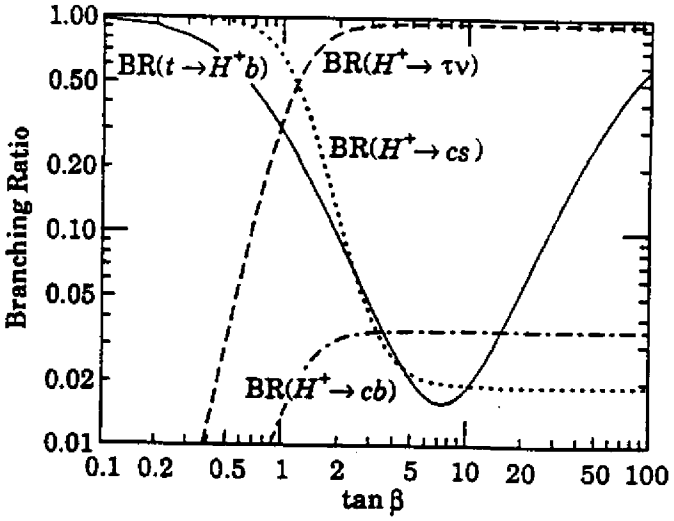

FIG. 27. Branching fractions for the reactions $t \to H^+b$ (solid) and $H^+ \to \tau\nu$, $c\bar{s}$, $c\bar{b}$ as a function of $\tan\beta$[66]. We have assumed $M_{\rm top} = 250$ GeV and $M_{H^+} = 150$ GeV.

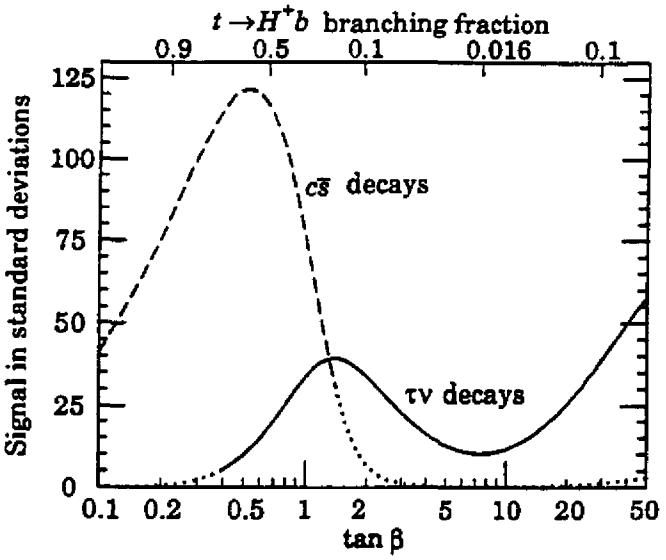

FIG. 28. The solid curve shows the statistical significance of the excess of isolated pions due to $t \to H^+b$, $H^+ \to \tau\nu$, and $\tau \to \pi\nu$ relative to expectations for $t \to W^+b$ (assuming lepton universality) as a function of $\tan\beta$ (bottom labels). We require an isolated lepton with $p_t > 40$ GeV/c and an isolated pion with $p_t > 40$ GeV/c (for $p_t > 100$ GeV/c there are $\frac{2}{3}$ as many standard deviations). The dashed curve shows the statistical significance of the H^+ peak in the two-non-b-jet invariant mass distribution as a function of $\tan\beta$. We assume one SSC year of running and have taken $M_{\rm top} = 250$ GeV and $M_{H^+} = 150$ GeV. For $\tan\beta$ values where the curves become dotted, the given technique has become marginal for H^+ discovery. The upper labels give the $t \to H^+b$ branching ratio, which reaches a minimum at $\tan\beta \approx 8$, see Fig. 27.

of leptons and charge $-\frac{1}{3}$ quarks while the other generates the mass of charge $\frac{2}{3}$ quarks. This is the model predicted by minimal supersymmetry and will be the one considered here (Model-I yields similar results for $\tan\beta < 5$, but has a very small branching ratio for $t \to H^+b$ for $\tan\beta > 10$). The couplings of the charged Higgs bosons to fermions are entirely determined by the quark and lepton masses and by $\tan\beta = v_2/v_1$, where $v_1(v_2)$ are the vacuum expectation values of the Higgs field which couples to the down (up) type fermions. The branching fractions for $t \to H^+b$, $H^+ \to \tau\nu$, and $H^+ \to c\bar{s}$ depend on $\tan\beta$ as shown in Fig. 27.

We have investigated two methods, applicable to overlapping ranges of $\tan\beta$, for H^+ detection in $t\bar{t}$ events for the case $M_{\rm top} = 250$ GeV and $M_{H^+} = 150$ GeV[66]. Method (i) involves a search for an excess of τ leptons arising from H^+ decay. Method (ii) involves reconstruction of the hadronic decays $H^+ \to c\bar{s}$. Both methods require an isolated electron or muon with $p_t > 40$ GeV/c and $|\eta| < 2.5$. Leptons are isolated if the nonleptonic energy observed in the calorimeter in a cone of $R = 0.4$ is less than 20% of the lepton energy. The events are further selected by requiring two tagged b-jets (from the decay of the t and $\bar{t}$) each with $p_t > 30$ GeV/c and $|\eta| < 2.0$. We used ISAJET version 6.31 to generate the $t\bar{t}$ events. The background from non-$t\bar{t}$ events is negligible.

In Method (i) we search for $\ell\tau$ events (*e.g.*, $t \to bW^+ \to b\ell^+\nu$, $\bar{t} \to [\bar{b}H^-$ or $\bar{b}W^-] \to \bar{b}\tau^-\nu$) in which the τ decays to a single $\pi^\pm$ (or $K^\pm$) with $p_t > p_t^{\rm cut}$ where $p_t^{\rm cut} = 40$ GeV/c. The τ signature is an isolated charged hadron, where isolation for a hadron is defined in analogy with the lepton definition above. Note that this requires a good momentum measurement for the charged hadron. If t quarks only decay to W^+b, the observed number of $\ell^+\ell^-$ events plus lepton universality in W decays allows us to compute the number of $\ell\tau$ events expected. If instead top quarks can also decay to H^+b, and if $BR(H^+ \to \tau\nu)$ is not small, we would detect an excess of $\ell\tau$ events over the universality prediction.

The statistical significance of the excess in the observed number of isolated pions over the prediction from universality is given in Fig. 28. It is important to include the polarization of the τ's in Monte Carlo studies; ignoring this polarization reduces the num-

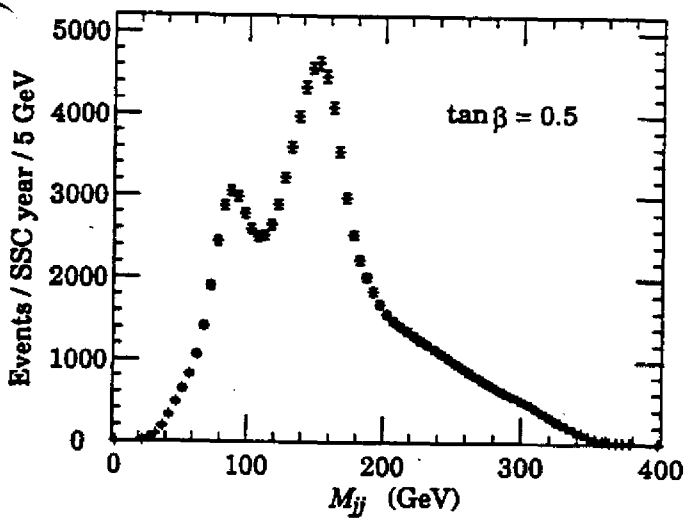

FIG. 29. Two-jet mass distribution, for the sum of the $t\bar{t} \to WWb\bar{b}$ and $t\bar{t} \to WHb\bar{b}$ events in the case $\tan\beta = 0.5$. Only one two-jet combination per event is plotted: the combination with the two highest p_t non-b jets consistent with the t mass (see text).

ber of standard deviations by a factor of two. After one year of SSC running, we could detect five standard deviation signals for $t \to H^+b$, $H^+ \to \tau^+\nu$ for all $\tan\beta > 0.5$.

For smaller values of $\tan\beta$, where $BR(H^+ \to \tau\nu)$ becomes small, we must employ the $H^+ \to c\bar{s}$ decay mode (Method (ii)). For this purpose, we have extended the technique described in Ref. 66 to study a 250 GeV top quark decaying to H^+ (or W^+) with $H^+(W^+) \to u\bar{d}$ or $c\bar{s}$ (with the same lepton trigger as for Method (i)). Jets are formed by clustering final-state particles appearing in the region $|\eta| < 3.0$ within a cone of radius $R < 0.7$. The 4-momenta of these jets are then smeared with the assumed jet resolution of the SDC calorimeter.

Any two jets (excluding the tagged b jets) within $|\eta| < 2.5$ and $p_t > 20$ GeV are then used to form invariant mass combinations. The combinatorial background can be reduced by restricting the dijet invariant mass plot to the two (non-b) jets with the highest transverse momenta that in combination with either one of the tagged b jets yield a three-jet invariant mass smaller than 400 GeV. This requirement is consistent with the top quark mass of 250 GeV already measured by the methods described above. The combinatorial background is severely reduced by only plotting one combination per event, and this choice is usually the correct one. The resulting W^+ and H^+ peaks for $\tan\beta = 0.5$ are shown in Fig. 29.

To quantify the statistical significance of the H^+ mass peak, we again plot the number of standard deviations above background as a function of $\tan\beta$ in Fig. 28. The combinatorial background can arise from either $t\bar{t} \to WWb\bar{b}$ or $WHb\bar{b}$. These two sources look very similar, so we can scale the combinatorial background to fit the observed data. The signal is the number of events above this scaled background in the H^+ or W^+ peak. The highest $\tan\beta$ value for which we could discover the charged Higgs by this method depends critically on understanding the shape of the combinatorial background. We conservatively argue that Method (ii) is useful only for $\tan\beta < 1.5$. For $\tan\beta > 1.5$ the H^+ peak is much less distinct, though the W peak remains visible. For $\tan\beta < 0.2$, where there are very few WW decays, the W mass peak is not visible above the background, although the H^+ peak may be substantial (with 1,000 or 10,000 events for $\tan\beta = 0.06$ or 0.2 respectively). The lowest value of the branching ratio $t \to H^+b$ for which we are sensitive depends on the $H^+ \to \tau\nu$ branching ratio and the $H^+ \to c\bar{s}$ branching ratio, but is roughly 2%.

Conclusions

We have described three different techniques for discovering the top quark and measuring its mass. The isolated $e\mu$ mode yields a clear signal, but a less reliable mass determination. The lepton + jets and the sequential $e\mu$ modes provide mass measurements dominated by systematic errors, which we estimate to be 3–6 GeV for the two modes for a top mass of 250 GeV and one nominal SSC year of luminosity. As the errors are overwhelmingly systematic, measurements made using a substantially smaller data sample will have only slightly larger errors.

We have also analyzed the decay properties of the top quark. The ratio of the semi-leptonic decay rate to the $q\bar{q}$ rate can be measured with a precision of 2–3%. The specific case of $t \to H^+b$ has also been studied in $t\bar{t}$ events in which the second t decays to $W^\pm b$. In the particular case of $M_{\rm top} = 250$ GeV and $M_{H^+} = 150$ GeV, detection of the charged Higgs boson appears possible over the entire interesting range of parameter space ($t \to H^+b$ branching ratios above 2%) using either $H^+ \to \tau\nu$ decays or $H^+ \to c\bar{s}$ decays or both. These studies illustrate the importance of efficiently tagging b-quark jets and measuring charged hadron momenta to identify τ's.

4.4. Jet energy resolution

Demonstrate the jet energy resolution of your proposed detector by studying decays

- $Z \rightarrow jet + jet$
- $Z' \rightarrow jet + jet, \quad M_{Z'} = 1\ TeV$

We have studied the dijet invariant mass resolution from Z and Z' decays and the irreducible contributions to the dijet invariant mass resolution from physics-related sources such as clustering, jet fragmentation fluctuations and contributions from underlying events. These effects determine a minimum mass resolution that is independent of detector parameters. In addition, we have studied the effects on the mass resolution induced by the detector, particularly by calorimeter energy resolution.

Detector Independent Effects

The energy and angular resolutions of jets from Z's and Z''s depend on the production process, which determines the distribution of transverse momenta. Furthermore, the dijet mass resolution depends on the Lorentz boost of the Z's and Z''s. At low p_t we form the invariant mass of the two jets, whereas for highly boosted Z's the invariant mass of the coalesced jet provides the best estimate of the mass. At low p_t, jets are broad, with substantial tails of particles escaping from any reasonable clustering region; while, at high p_t, jets form tighter clusters, and clustering losses are smaller, but not negligible. For this reason the optimal size for the clustering region depends on the p_t of the jet.

Another dependence on the production process comes from the inevitable inclusion in the clustering region of particles that arise from the underlying event and not from the actual Z or Z'. Fluctuations in this underlying event degrade the energy and angular resolutions. The effect of particles lost from the clustering cone can be reduced by increasing the cone size, but this leads to increased fluctuations in the contribution of the underlying event and other events from the same bunch crossing.

A further contribution to the detector-independent resolution effects arises from fluctuations in the energy fraction carried away by undetected neutrinos from semileptonic decays of heavy quarks inside the jet. These losses produce a long tail of low invariant masses of the dijet system. Finally, gluon radiation also leads to losses out of the clustering cone.

Detector Dependent Effects

Detector induced resolution effects that have been studied in formulating our answer to this question include:

- calorimeter segmentation,
- calorimeter energy resolution,
- magnetic field and
- nonlinearity of the hadron calorimeter

Methodology

Because both detector-dependent and detector-independent resolution contributions depend on p_t, we have studied the dijet mass resolution at low p_t (50 GeV/c < p_t < 60 GeV/c) and at high p_t (500 GeV/c < p_t < 600 GeV/c) for both Z and Z'. Two independent studies of these processes have been made and reach similar conclusions [67,68].

Events containing Z's and Z''s are generated via the Drell-Yan process using PYTHIA version 4.9 with an additional requirement that the jet axis be within $|\ \eta\ | < 1$. The Z's and Z''s are generated with zero intrinsic width, in order to better evaluate detector resolution effects. For the Z', the intrinsic width (which we define as full-width/2.3) is model dependent with typical values of 0.2–1.4% of the mass[69]. This is somewhat smaller than the effects described below. For the Z, the intrinsic width is substantially smaller than detector-independent effects induced by clustering and fragmentation. The simulation tracks individual particles to the calorimeter, including the effect of the magnetic field. For the calorimeter, the energy deposit in individual cells is done using realistic shower shapes.

Jet clusters are reconstructed by starting with a "seed" tower and accumulating energy within an $\eta - \phi$ cone of fixed radius R centered on the seed tower. We start with the seed tower with the highest energy and form subsequent clusters by searching outside the already formed clustering cones to select a new seed tower of highest energy. In the case of overlapping cones, the energy is assigned to the cluster with the higher energy seed. A single-tower threshold of 0.1 GeV, and a seed threshold of 2 GeV are used. Clusters are not saved unless they have more than 5 GeV in E_t. Unless otherwise noted, the tower size is $\Delta\eta = \Delta\phi = 0.05$ and the center of the tower is taken as the direction of energy flow. The cluster cone radius used is 0.7.

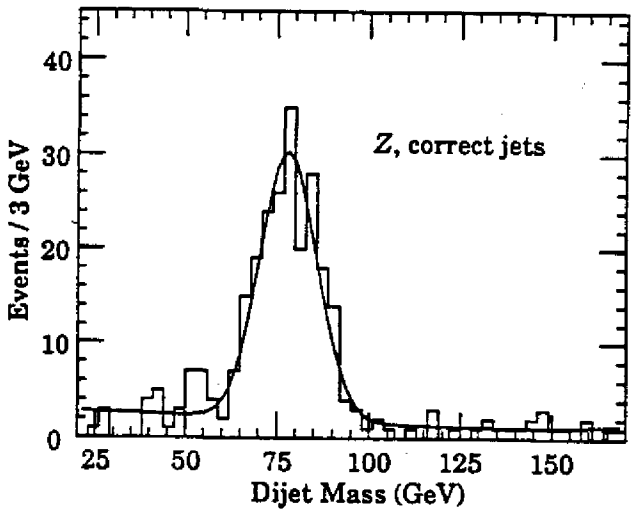

FIG. 30. Dijet mass distribution for Z events with $50 < p_t < 60$ GeV/c for case (d) as described in the text. Only the correct jet pair is included in the plot. The smooth curve is a fit to a Gaussian plus a polynomial function.

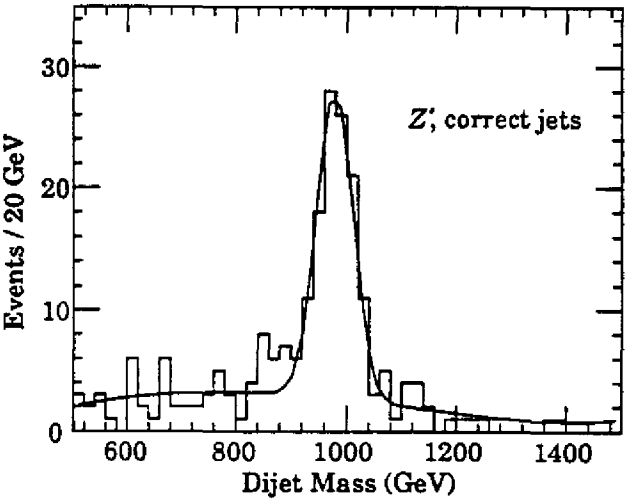

FIG. 31. Same as Fig. 30, for Z' events of mass 1 TeV with $500 < p_t < 600$ GeV/c.

The final clusters formed in this way are identified as jets. The jet 4-momentum vector is then calculated by summing all calorimetric cells above the tower threshold within the cone, treating each cell as a massless particle. The invariant mass of the two jet system is calculated as $M_{JJ} = [(E_1 + E_2)^2 - (\vec{p}_1 + \vec{p}_2)^2]^{1/2}$. For high p_t Z's, when the two jets have coalesced, we calculate a single jet mass as $M_{JJ} = \sqrt{E_1^2 - |\vec{p}_1|^2}$.

The mass distributions that result from this procedure are non-Gaussian. They have long, asymmetric tails with losses primarily arising from undetected neutrinos and from gluon radiation. In this study, in order to characterize the central peak of each mass distribution in a meaningful way, we fit the mass distributions with the sum of a Gaussian and a polynomial function. To compare resolutions between simulations with different conditions we use the value of σ from the Gaussian part of the fit. Examples of the reconstructed mass distributions for the Z and Z' are shown in Fig. 30 and Fig. 31. We have combined the correct jets, as given by the Monte Carlo. Figure 32 shows an example of plotting all jet combinations. The values given below for mass resolution are derived from fits to distributions combining the correct jets thereby enhancing the sensitivity to detector-induced effects.

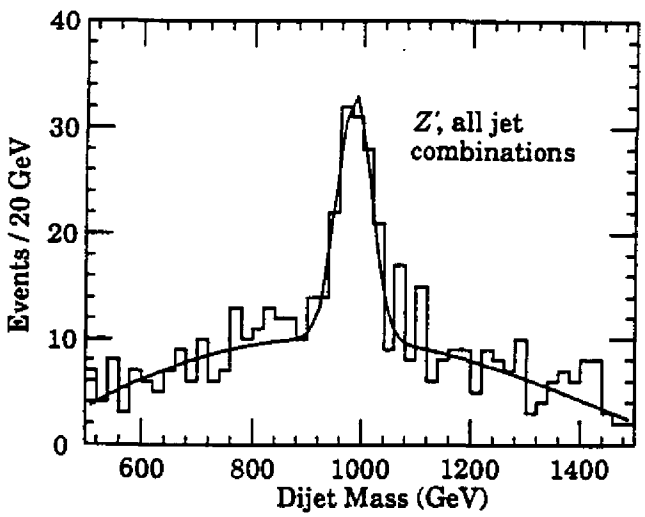

FIG. 32. Same as Fig. 31, except that all jet combinations are plotted.

Resolution Studies

In Fig. 33 and Fig. 34, we present results from calculations of the dijet mass resolution for a number of assumptions about the detector-independent contributions and about the calorimeter parameters for the Z and Z' at both high and low p_t. The different effects are invoked sequentially in successive points on the graphs in order to demonstrate the different contributions to the dijet resolution. The conditions in the points on the graph are as follows:

(*a*) The original quark direction is used as the center of a clustering cone of radius 0.7, within which the energy from all detectable tracks in the generated event is combined as a jet. Extra tracks from

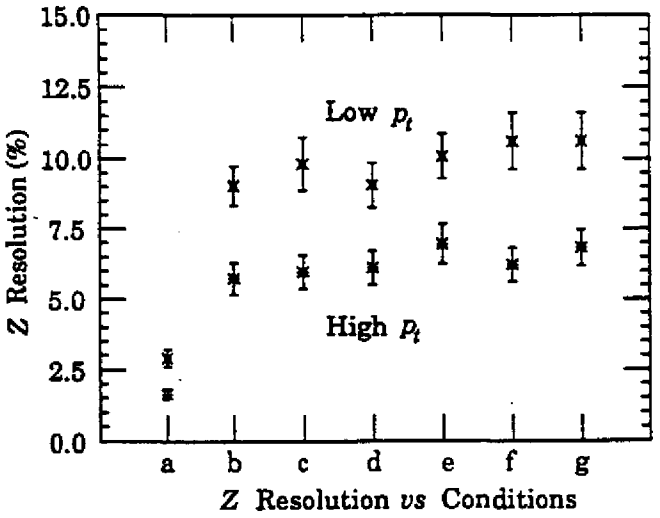

FIG. 33. Summary of mass resolution calculations for reconstructed Z's for the two p_t ranges described in the text. The first two points show the effect of detector-independent contributions to the resolution. The following points show the effect of variations in detector performance. The values plotted represent the sigma from the fits described in the text. The error bars correspond to the statistical error on the sigma. See the text for explanations of each entry.

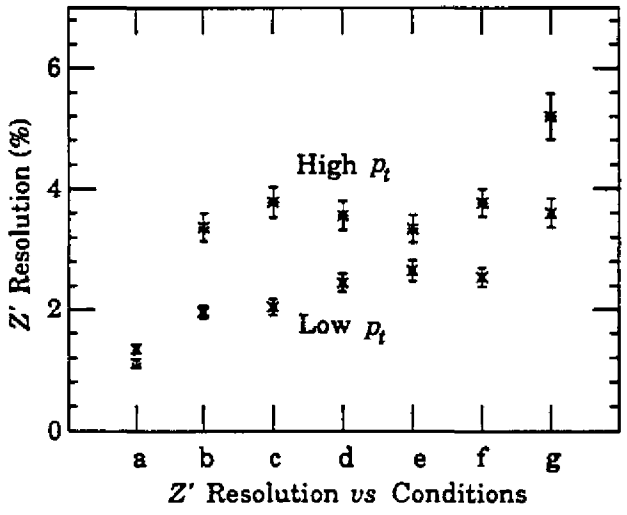

FIG. 34. Same as Fig. 33, but for Z''s of mass 1 TeV.

the underlying event are included. No simulation of showers is performed. This shows the contribution to the mass resolution of basic physics processes, including fluctuations in fragmentation energy outside the cone, effects of the underlying event, missing neutrinos, and gluon radiation.

(*b*) Our detector simulation distributes the shower energy with a realistic shape, but perfect energy resolution is assumed. Clustering is now done with seed towers as described above. This point represents a minimum resolution for a perfect detector with a reasonable tower geometry.

(*c*) Same as (b) with the addition of energy resolution in the calorimeter cells of $0.3/\sqrt{E} \oplus 0.02$ for individual hadrons and $0.15/\sqrt{E} \oplus 0.01$ for photons and electrons.

(*d*) Same as (c) with a hadronic calorimeter resolution of $0.5/\sqrt{E} \oplus 0.03$.

(*e*) Same as (c) with a hadronic calorimeter resolution of $0.7/\sqrt{E} \oplus 0.04$.

(*f*) Same as (d) with an electromagnetic calorimeter resolution of $0.25/\sqrt{E}$.

(*g*) Same as (d) with calorimeter noncompensation corresponding to the extreme limit of the acceptable range defined in Table 1, namely $e/h = 1.3$. The resulting overall constant term of about 4% in the hadronic energy resolution is in addition to the 3% constant term introduced in (d) for each hadron. The nonlinear response of the hadron calorimeter due to imperfect compensation is simulated using an ansatz of Groom[70]. We emphasize that this represents an extreme, and that we are striving to achieve much better compensation.

In Fig. 33 and Fig. 34, the first two points can be understood as successively adding effects that arise from the physics process and the irreducible parts of the measurement process, and do not reflect the specific capabilities of the SDC calorimeter. The remaining points illustrate the effect of calorimeter parameters that span the range of calorimeter performance being considered by the SDC. The dominant contribution to the mass resolution does not come from the detector but from clustering and other effects. In the case of low p_t Z's the mass resolution is dominated by clustering, the fluctuation of energy outside the $R = 0.7$ cone and by fluctuations of the underlying event. A perfect detector can measure the Z mass with a resolution of about 9%. Detector induced effects worsen this resolution by at most a factor of 1.25. In the high p_t Z case, most particles are well contained in the cone and the minimal resolution is about 6%. Detector induced effects may worsen the resolution by about a factor of 1.2. In the case of the Z', the detector-dependent contributions are negligible for high p_t and small for low p_t

except for the effect of the extreme e/h value introduced in (g) above, which worsens the resolution by about a factor of 1.5. The Z''s have worse resolution at high p_t than at low p_t because of the larger role played by angular resolution effects.

Several other issues have also been studied for their effect on the mass resolution for conditions (d). The results presented above include the effects of the solenoid field. The magnetic field acts to spread jets, removing some energy from the clustering cone, and also changes the direction of the energy flow within the cone. At low p_t, the detector-independent fluctuations dominate and the degradation in resolution with a magnetic field is negligible, within the statistics of our present simulation. At high p_t, the mass resolution is degraded by at most a factor of 1.2.

The segmentation of the calorimeter influences the angular resolution and hence the mass resolution. Previous studies have shown a weak dependence of the mass resolution on segmentation[71]. We have confirmed these previous studies. Changing the calorimeter segmentation in the range from 0.03 to 0.15 causes less than a 15% change in the mass resolution for any of the cases. Finally, setting a p_t threshold of 1.0 GeV/c (instead of the nominal 0.1 GeV/c) to attempt to reduce the effect of the underlying event, has no effect for high p_t Z's or on Z''s at any p_t, but degrades the mass resolution by about a factor of 1.3 for low-p_t Z's.

Conclusions

From these studies we conclude that the intrinsic effects of jet clustering, jet fragmentation uncertainties and fluctuations in the underlying event dominate the mass resolution for both low and high p_t Z and Z' production for the range of calorimeter performance under investigation by the SDC. The physics study of top quark detection through multi-jet mass reconstruction (Section 4.3) confirms this conclusion. For some conditions in which the intrinsic fluctuations are very small (low p_t Z' for example), extreme e/h deviation from unity produces detectable degradation. We believe that the design goals given in Table 1 represent a reasonable match to the requirements suggested by the analysis described here.

4.5. Z' of mass 4 TeV

Demonstrate the acceptance and resolution (not the ability to run at extremely high luminosities) of the lepton detector by a study of a Z' with a mass of 4 TeV. Show a measurement of the mass and asymmetry for 1000 produced $Z' \rightarrow e^+e^-$, $\mu^+\mu^-$, $\tau^+\tau^-$ each.

To answer this question we assume that the Z' has the same couplings to quarks and leptons as the standard model Z. Such a Z' has a larger production cross section than the E_6 Z_η discussed in the EoI[69]. In this study we have required that 1000 events be produced in each of the e^+e^-, $\mu^+\mu^-$, $\tau^+\tau^-$ channels with the invariant mass of the lepton pair in the range $M_{Z'} \pm \Gamma_{Z'}$, where $\Gamma_{Z'}$ is the full width of the Z' (112 GeV in our model). The running time to collect these events at $\mathcal{L} = 10^{33}\,\mathrm{cm}^{-2}\mathrm{s}^{-1}$ would be about 10 years; therefore, such a heavy object can only be explored in detail with higher luminosity running of the SSC. To answer the question as posed, we assume the detector performance expected at the nominal SSC luminosity, as defined in Section 4.1. More details of this analysis can be found in Ref. 72.

The Z' Mass and Width Measurements

Figure 35 shows the invariant mass spectra for e^+e^- and $\mu^+\mu^-$ pairs from the Z' as well as the background from continuum Drell-Yan processes. There are no other relevant backgrounds.* The pseudorapidity coverage of the SDC detector corresponds to a geometrical acceptance of 86% for the the e^+e^- and $\mu^+\mu^-$ modes. In the e^+e^- channel, the mass resolution of the detector is less than the natural width of the Z' so that the mass and width can both be measured. For the 1000 event sample shown in Fig. 35(a), after deconvoluting the resolution of the detector we obtain an error on the mass of ± 3 GeV and an error on the width of ± 7 GeV.

The peak in the μ channel, shown in Fig. 35(b), enables a measurement of the Z' mass with an error of ± 10 GeV. The resolution in this channel is clearly not good enough to obtain information concerning the width. Universality is tested by comparing the event rates in the e^+e^- and $\mu^+\mu^-$ channels, corrected for the difference in resolution for the two channels. The two plots shown in Fig. 35(a) and

*The absence of serious backgrounds for high p_t dileptons has been demonstrated in the UA1 [73], UA2 [74], and CDF [75] experiments. The ratio of the Z' cross section to QCD background at the SSC is similar to the ratio of Z production to QCD at current collider energies.

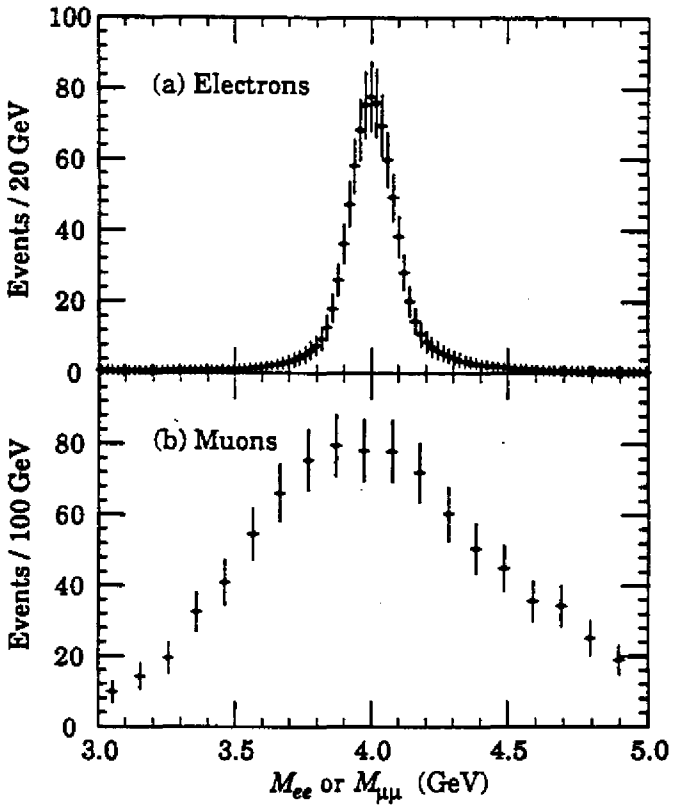

FIG. 35. The invariant mass distribution of (a) e^+e^- pairs and (b) $\mu^+\mu^-$ pairs from Z''s of mass 4 TeV, including the Drell-Yan background.

Fig. 35(b) give 993 and 904 events in these channels respectively if we sum over dilepton masses in the range 3 TeV $< M_{\ell\ell} <$ 5 TeV. In the absence of the Z' these values would be 38 and 41. The dominant error in this measurement of e/μ universality will be the 4.5% statistical error.

The situation is more complex for the $\tau^+\tau^-$ channel. Pairs of isolated tracks from the decays $\tau \to e\nu\nu$, $\tau \to \mu\nu\nu$, and $\tau \to \pi\nu$ can be exploited. The e^+e^- final state (but not the $\mu^+\mu^-$ final state) can be used because we can eliminate events where the invariant mass of the e^+e^- pair is between 3.7 TeV and 4.3 TeV, so that the direct decay $Z' \to e^+e^-$ is excluded. The missing-E_t requirement below eliminates the e^+e^- Drell-Yan background. In the case of electrons and hadrons we require that the energy measured in the calorimeter (E) and the momentum measured in the tracking (p) satisfy $E/p < 1.15$. In the case of muons, we require that there be less than 5 GeV in a cone of radius $R = 0.4$ around the muon direction.

There is an irreducible background from the Drell-Yan production of τ pairs and from leptons produced

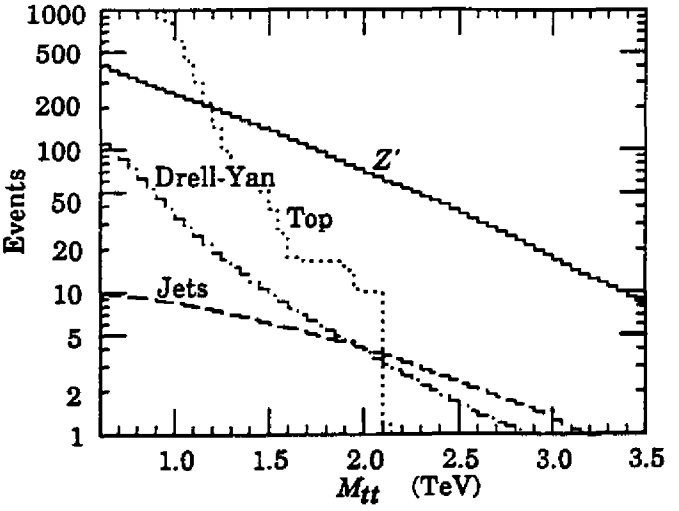

FIG. 36. The rate for the production of ee, $e\mu$, $e\pi$, $\mu\pi$ and $\pi\pi$ final states from the process $Z' \to \tau\tau$ for a Z' of mass 4 TeV. Each pair is required to have a two track invariant mass $M_{tt} > M_0$. The integrated rate is shown as a function of M_0. The tracks are required to have $p_t > 200$ GeV/c, to be back-to-back within 30° and to satisfy the cuts described in the text. The events are also required to have missing-E_t of at least 100 GeV in the transverse plane within 30° of either track. Shown separately is the background from $t\bar{t}$ production with $M_{\rm top} = 150$ GeV (dotted), the Standard Model prediction for Drell-Yan production of τ pairs (dot-dashed) and QCD jet production (dashed).

in the decays of W's from $t\bar{t}$ events. For a 4 TeV Z', it is possible to reduce the $t\bar{t}$ background considerably by requiring that the tracks have high p_t, that the invariant mass of the two tracks be large, that they be almost back-to-back in azimuth, and that there be missing-E_t with an azimuthal angle close to that of one of the tracks. Figure 36 shows the integrated invariant mass distribution for ee, $e\mu$, $e\pi$, $\mu\pi$, and $\pi\pi$ events where the particles are required to to satisfy the above cuts and to have $p_t > 200$ GeV/c. We have also required that there be at least 100 GeV of missing-E_t and that the missing-E_t vector in the transverse plane be within 30° of either track. The rate is shown as a function of the minimum invariant mass of the two-track system (M_{tt}). The estimated backgrounds from Drell-Yan production of τ pairs and from $t\bar{t}$ events (assuming a top mass of 150 GeV) are shown separately.

There is an additional background from dijet events where both jets fragment into isolated particles. This is rare but the jet rate is very large. As in

the previous answers, the dijet cross section has been multiplied by a factor of 5×10^{-4} per jet (2.5×10^{-7} per event) to account for the probability that both jets fragment into leading particles that carry almost all of the energy of the jets. This value is deduced from the CDF results discussed in Section 4.2, and we note that the fragmentation function at large z should decrease with increasing jet E_t and thus the CDF estimates should be taken as an upper bound, making our background rejection factor conservative. The tracking and calorimeter systems will enable the fragmentation function to be measured over a range of jet energies, testing this assumption.

It is clear from Fig. 36 that if $M_{tt} > 1400$ GeV, the rate for Z' events exceeds that of the $t\bar{t}$ background. There are 160 signal events in this range. We emphasize that the top mass and decay properties will have been measured in SDC, and hence the $t\bar{t}$ background will be precisely known. Therefore, we expect a statistical error on the ratio $BR(Z' \to \tau\tau)/BR(Z' \to e^+e^-)$ of 8%. This error could be improved by accepting a larger fraction of the tau decays. In order to accept all 1-prong decays we would have to relax the E/p cut and study the resulting jet rejection. This requires further study, but could reduce the statistical error by a factor of 1.5.

The Z' Asymmetry Measurement

By measuring the asymmetry in the leptonic decays, one can gain information on the helicity structure of the couplings of the Z'. Events are selected for which the Z' has substantial longitudinal momentum. Since the large-x part of the distribution for a proton is more populated by quarks than antiquarks, for sufficiently large Z' longitudinal momenta, the quark (antiquark) that produced the Z' is likely to have been moving in the same (opposite) direction as the Z' itself. If the couplings of the quarks to the Z' violate parity, the Z's will be produced with a preferred helicity. If the leptonic couplings also violate parity, then by determining the lepton sign one can determine an asymmetry:

$$A = \frac{\int_0^1 d\cos\theta^* \, dN/d\cos\theta^* - \int_{-1}^0 d\cos\theta^* \, dN/d\cos\theta^*}{\int_0^1 d\cos\theta^* \, dN/d\cos\theta^* + \int_{-1}^0 d\cos\theta^* \, dN/d\cos\theta^*}$$

where θ^* is the angle, measured in the center of mass frame of the Z', of the negatively charged lepton with respect to the direction of motion of the Z' in the lab. These angular distributions, plotted in Fig. 37(a) and Fig. 37(b), clearly show a small asymmetry,

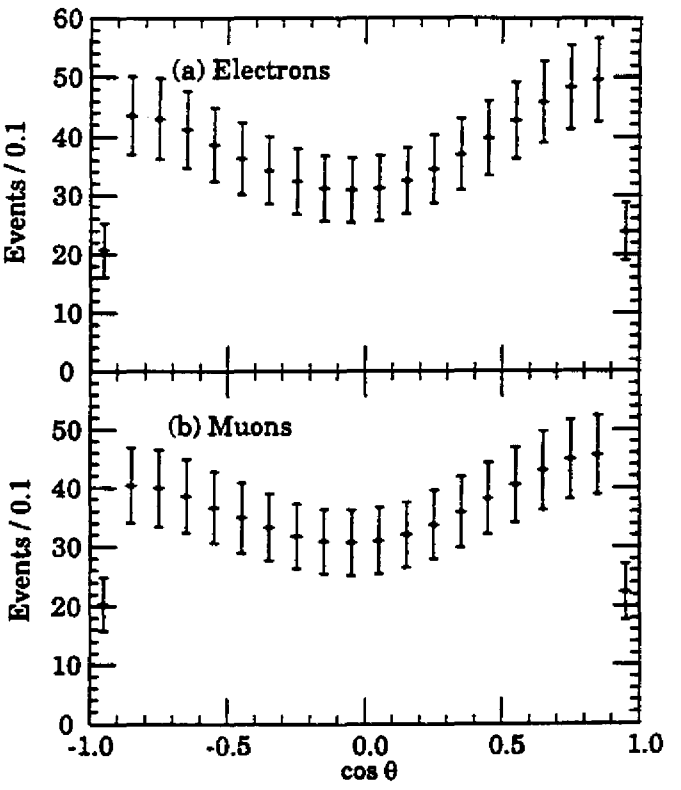

FIG. 37. The angular distribution, $dN/d\cos\theta^*$, of the (a) e^- or (b) μ^- in the center of mass frame of the e^+e^- or $\mu^+\mu^-$ pair for dilepton pairs. The mass of the pair is required to be between 3 and 5 TeV and the pair to have momentum along the beam direction of at least 1 TeV/c measured in the lab frame. The value $\theta^* = 0(\pi)$ corresponds to the case where the e^- or μ^- is parallel (antiparallel) to the direction of motion of the pair. The measured charges of the leptons are also required to have opposite signs.

as well as a drop in the detector acceptance for $|\cos\theta^*| > 0.8$. In making these plots we have selected events where the invariant mass of the reconstructed dilepton pair is between 3 and 5 TeV, where the longitudinal momentum along the beam direction of the pair is greater than 1 TeV/c, and where the leptons are measured to have opposite signs. There are 741 (707) events in these plots for the electron (muon) channel. The loss of events from Fig. 35 is due almost entirely to the Z' momentum cut. In 96% (99%) of the events in the electron (muon) plots the charges of both particles are measured correctly.

The asymmetry is dependent upon the invariant mass of the dilepton pair due to interference effects between the photon, Z, and Z' propagators. For the couplings that we are using, and for a dilepton mass

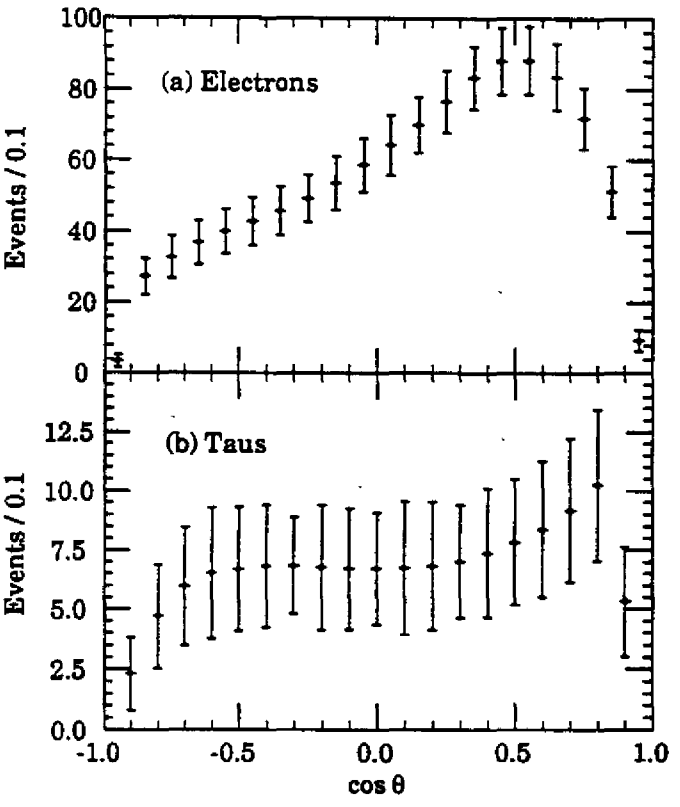

FIG. 38. (a) Same as Fig. 37(a), except the e^+e^- pair is required to have its mass between 1 TeV and 2 TeV. (b) The angular distribution of the negatively charged track of the events from Fig. 36 where the two tracks are required to have an invariant mass greater than 1400 GeV. The angle is measured in the frame where the tracks are back to back. The value $\theta^* = 0$ corresponds to the case where the negatively charged track is parallel to the component of momentum along the beam direction as measured in the lab frame. The β of the boost from the lab frame to the back to back frame is required not to be in the range $-0.24 < \beta < 0.24$. The measured charges of the tracks are also required to have opposite signs.

equal to the Z' mass, we have an asymmetry

$$A = \tfrac{3}{4} x_e (f_u x_u + f_d x_d) .$$

where f_u (f_d) is the fraction of Z' produced from the annihilation of charge 2/3 (1/3) quarks and x_e, x_u and x_d depend on the helicity structure of the Z' couplings. Since $x_e \propto 1 - -4\sin^2\theta_W$, the expected asymmetry is very small (5.2%) in this model. Larger asymmetries are expected in other models; the Z_η has an asymmetry of 11%, and the E_6 Z' with $\cos\alpha = -0.6$ has an asymmetry of -16% (see Ref. 69). We obtain an error on the asymmetry of $\delta A = \pm 5\%$ for the event samples shown in Fig. 37.

Due to interference effects the asymmetry is larger for $M_{e^+e^-} < M_{Z'}$[76]. To illustrate this effect we show in Fig. 38(a) the angular distribution for e^+e^- events with 1 TeV $< M_{e^+e^-} <$ 2 TeV. In this mass range the asymmetry is 27%. The statistics in Fig. 38(a) are comparable to those in Fig. 37(a), and the asymmetry in Fig. 38(a) is measured with an error of 4%.

Measurements of the asymmetry in the $\tau\tau$ mode are more difficult due to the limited statistics in the channels that we observe. However, the direction of the τ and its sign are both determined by the direction and sign of the e, μ, or π from its decay. These particles have less momentum than the electrons produced from the direct decay of the Z', and hence their charges are well measured. Events are selected from those in Fig. 36 by requiring that the invariant mass of the two tracks be greater than 1400 GeV. These events are then boosted back along the beam direction to the frame where the two tracks are back to back. Events are rejected if the β of this boost is in the range $-0.24 < \beta < 0.24$ in order to ensure that the decaying Z' have a nonzero longitudinal momentum. The resulting angular distribution is shown in Fig. 38(b). The expected asymmetry is 10%, and the statistics correspond to an error of $\pm 10\%$. While most of the events in Fig. 38(b) arise from $M_{\tau\tau} \sim M_{Z'}$, there are a significant number with $M_{\tau\tau} < M_{Z'}$. Hence the asymmetry shown in Fig. 38(b) is intermediate between those shown in Figs. 37(a) and 38(a).

Conclusions

The SDC detector is able to measure the mass and width of the Z' in the e^+e^- channel with errors of ± 3 and ± 7 GeV respectively. In the muon channel, the mass is measured to ± 10 GeV. Electron/muon universality can be probed with an error of 5%, and the asymmetries in these two channels measured with a statistical precision of 5%. In the case of τ's, we are limited by background from the $t\bar{t}$ final state, but we can measure e/τ universality with an error of 8%, and the asymmetry with an error of 10%.

5. Organization and management of the collaboration

The organization and management of the SDC are discussed in some detail in Chapter 8 of the EoI. An updated list of the principal officers of the SDC, the membership of its Executive Board, and the chairpersons of the various technical steering committees are shown in Table 10. The Executive Board is elected by the collaborators and provides the scientific direction of the experiment in concert with the spokesperson. The Technical Board consists of the spokesperson, deputy spokespersons, technical manager, co-chairpersons of the steering committees, and other individuals appointed by the spokesperson.

The technical steering committees have provided the leadership in moving toward our reduced-scope detector design, with general guidance given by the Technical Board. They have the major responsibility for leading the SDC in its task of making technological choices on a schedule that allows maximum latitude for R&D progress compatible with being ready at SSC turn-on. As responsibility for the R&D program moves to the SDC, these committees will have the task of recommending priorities for that program to the Executive Board, Technical Manager, and Spokesperson.

For issues that cross subsystem lines, or that require specialized knowledge, the spokesperson and technical manager will appoint *ad hoc* task forces with well-delineated charges. This procedure has already been used to good effect in the selection of the magnet style.

Table 10

Management of the Solenoidal Detector Collaboration

SPOKESPERSON:
G. Trilling (LBL)

DEPUTY SPOKESPERSONS:
G. Bellettini (University of Pisa)
D. Green (FNAL)
T. Kondo (KEK)

TECHNICAL MANAGER:
M. Gilchriese (LBL)

CHAIRPERSON OF INSTITUTIONAL BOARD:
T. Kirk (ANL)

CHAIRPERSONS OF TECHNICAL STEERING COMMITTEES:

Calorimetry
A. Maki (KEK)
L. Nodulman (ANL)
J. Siegrist (SSCL)

Computing and analysis software
K. Amako (KEK)
A. Baden (Univ. Maryland)
L. Price (ANL)

Detector integration and experimental facilities
J. Cooper (FNAL)
R. Kadel (LBL)

Electronics, data acquisition, and trigger
M. Campbell (Univ. Michigan)
A. Lankford (Univ. Calif. Irvine)
W. Smith (Univ. Wisconsin)
Y. Watase (KEK)
H. H. Williams (Univ. Pennsylvania)

OTHER MEMBERS OF TECHNICAL BOARD:
R. Hubbard (CEN Saclay)

EXECUTIVE BOARD:
D. Bintinger (SSCL)
S. Errede (Univ. Illinois)
G. Feldman (Harvard Univ.)
E. Gabathuler (Univ. Liverpool)
G. Hanson (Indiana Univ.)
K. Kondo (Tsukuba Univ.)
S. Mori (Tsukuba Univ.)
Y. Nagashima (Osaka Univ.)
T. Ohsugi (Hiroshima Univ.)
L. Price (ANL)
R. Ruchti (Univ. Notre Dame)
A. Seiden (Univ. Calif. Santa Cruz)
R. Thun (Univ. Michigan)

Muon systems
G. Feldman (Harvard Univ.)
S. Mori (Tsukuba Univ.)
R. Thun (Univ. Michigan)

Physics and detector performance
K. Einsweiler (LBL)
L. Price (ANL)
Y. Takaiwa (KEK)

Superconducting magnets
R. Kephart (FNAL)
A. Yamamoto (KEK)

Tracking
J. Elias (FNAL)
W. Ford (Univ. Colorado)
T. Ohsugi (Hiroshima Univ.)

Collaboration membership

The proposers listed on this LoI are PhD physicists who commit substantial fractions of their research time to the work of the Collaboration plus a number of engineers whose efforts are almost entirely devoted to this effort. The institutional membership consists of U.S. and foreign universities, laboratories, and institutes, each of whom must have at least two members. We also have a number of associated industrial collaborators who bring to the Collaboration their specialized technical and generalized manufacturing experience.

Applications for memberships in the SDC are made on an institutional basis. New institutions apply to the Institutional Board (IB) whose membership consists of one representative per institution. Each potential new member institution provides a list of proposed members and a statement of their scientific and technical areas of interest in the work of the SDC. This information is circulated to the IB for comment. Following this comment period, a vote is taken with one vote per institution. Acceptance follows immediately if there is a favorable majority of all institutions and the negative vote, if any, is no greater than 10% of all institutions. If these conditions are not met, the issue is carried for decision to the next IB meeting. Thus far, no institutions have been rejected for membership in the SDC.

Member institutions of the SDC may add individual members at their own discretion provided that they meet the criteria defined above. Individual physicists from nonmember institutions may become full members of the SDC by establishing a formal association with a member institution.

---

6. Budget request

Our budget request for the remainder of FY1991 is very similar to that presented in the Expression of Interest with the following major differences:

1. Funds for design of superconducting air-core toroids have been eliminated;
2. Funds to support video conferencing have been eliminated; and
3. The $500K of funds already allocated to the SDC have been subtracted on a task-by-task basis.

Our total funding request for the remainder of FY1991 is $5210. The request is presented by task and by institution in Table 11. We have divided the project reserve into two categories: contingency and R&D. Although most of the R&D for the SDC in FY1991 will be supported directly by the DOE/SSCL under the major subsystems R&D program or by other means, we anticipate the need for some modest R&D directed by the SDC. Subsequent to actions by the Program Advisory Committee and the SSCL in response to major subsystems R&D proposals and this LoI, we would expect to present a more detailed plan for dispersal of these funds to augment existing R&D in critical areas. As was explained in some detail in the EoI, the remainder of the funds are to support design integration of the detector subsystems and of the overall detector, and to support cost and schedule estimates.

We expect to begin formal construction of the SDC detector in FY1993. Therefore, preconstruction funding will be needed not only in FY1991 but also in FY1992. We assume that most of the R&D needed for the SDC detector in FY1992 (and beyond) will be supported under the auspices of the SDC rather than under the major subsystems R&D program. We are planning to formulate an R&D plan by late summer or early fall of 1991 summarizing the R&D progress made by members of the SDC and presenting a detailed request for FY1992. Clearly we are not now in a position to present detailed budget numbers for FY1992. Nevertheless we have made a preliminary estimate, in the framework of the SDC Level 3 WBS, for FY1992 funding (US only) that may be used for planning purposes. This is shown in Table 12 along with the FY1991 request (in the Level 3 WBS framework) for comparison.

Table 11

Budget request for the remainder of FY1991.

		SUB TOTALS ($K)	PRIORITY
Integration of tracking systems		**765**	**1**
Pixel and silicon trackers(LANL, LBL)	275		
Modular straw tracker(ORNL, WSTC)	245		
Fiber, hybrid and overall outer tracker(ORNL)	245		
Superconducting solenoid design		**300**	**1**
Design and integration with other systems(FNAL)	300		
Integration of calorimeter systems		**975**	**1**
Scintillating-tile(ANL, FNAL, WSTC)	650		
Liquid ionization(LBL)	325		
Integration of muon systems		**285**	**1**
Chamber support design(FNAL)	65		
Iron toroid design, chamber design and integration with other systems(U. of Wisconsin - PSL)	220		
Integration of electronics systems		**790**	**1**
Trigger systems(U. of Chicago, Harvard, U. of Michigan, U. of Wisconsin)	275		
Data acquisition systems(FNAL, IBM)	100		
Silicon and wire chamber rad-hard processing development(U. of Pennsylvania, UC Santa Cruz, IBM)	75		
Straw tube front-end system integration (Colorado, ORNL, U. of Pennsylvania)	75		
Calorimeter front-end system integration (FNAL, LBL, WSTC)	165		
Overall electronics system integration(WSTC)	100		
Computing and software engineering		**495**	**1**
Software engineers(ANL, FNAL, LBL)	300		
Workstations and other hardware(ANL, FNAL, LBL)	95		
Software packages and licenses(ANL, FNAL, LBL)	100		
Overall integration and coordination		**900**	**1**
Overall detector systems integration(LBL, RTK)	600		
Project coordination and management(LBL)	200		
Project reserve - contingency		**400**	**2**
LBL	400		
Project reserve - R&D		**400**	**2**
SSCL	400		
	GRAND TOTAL	**5210**	

Table 12

Preconstruction funding request for FY1991 and FY1992 by WBS element. Only the US part of the SDC preconstruction budget request is given in this Table. The budget request for FY1991 assumes that almost all of the R&D for the SDC is supported by the major subsystems program or by other means. In FY1992 it is assumed that most of the research and development will be supported under the auspices of the SDC. This budget request would also support subsystem engineering design and systems integration.

	FY91	FY92
1 TRACKING SYSTEMS	**0.69**	**6.8**
1.1 SILICON TRACKING SYSTEM	0.31	3
1.2 CENTRAL TRACKER	0.48	2.5
1.3 INTERMEDIATE TRACKER	0.10	0.3
2 CALORIMETRY	**1.05**	**6.5**
2.1 CENTRAL CALORIMETER	0.53	4
2.2 INTERMEDIATE CALORIMETER	0.42	2
2.3 FORWARD CALORIMETER	0.10	0.5
3 MUON SYSTEM	**0.30**	**1**
3.1 IRON TOROIDS	0.15	0.4
3.2 MUON CHAMBERS	0.15	0.5
3.3 MUON SCINTILLATORS		0.1
4 SUPERCONDUCTING MAGNETS	**0.30**	**0.6**
4.1 SC SOLENOID	0.30	0.6
5 DATA ACQUISITION & TRIGGER	**0.70**	**3**
5.1 DATA ACQUISITION SYSTEMS	0.35	1.5
5.2 TRIGGER SYSTEMS	0.35	1.5
6 COMPUTING	**0.60**	**1**
6.1 ON-LINE COMPUTING		0.2
6.2 OFFLINE COMPUTING	0.50	0.8
7 CONVENTIONAL SYSTEMS	**0.15**	**0.6**
7.1 UTILITIES	0.05	0.1
7.2 CONTROLS		0.1
7.3 SAFETY SYSTEMS		0.2
7.4 CRYOGENIC SYSTEMS	0.05	0.1
7.5 STRUCTURAL SUPPORT SYSTEMS	0.05	0.1
8 INSTALLATION AND TEST	**0.40**	**3.2**
8.1 TEST BEAM PROGRAM	0.20	2.5
8.2 SUBSYSTEM INSTALLATION AND TEST	0.20	0.7
9 PROJECT MANAGEMENT	**0.83**	**3.1**
9.1 PROJECT PLANNING	0.15	0.2
9.2 PROJECT TRACKING	0.00	0.2
9.3 DOCUMENT DISTRIBUTION AND CONTROL	0.05	0.2
9.4 SUBSYSTEMS INTEGRATION	0.70	2.5
TOTALS	**5.21**	**24.8**

The SDC expresses its strong appreciation to Ms. Betty Armstrong for her outstanding work in her preparation of this Letter of Intent.

7. References

1. G. H. Trilling *et al.*, "Solenoidal Detector Collaboration Expression of Interest," Solenoidal Detector Collaboration Note SDC-90-00085 (1990).
2. "Reply by the Solenoidal Detector Collaboration to Questions from the Program Advisory Committee," Solenoidal Detector Collaboration Note SDC-90-00084 (12 July 1990).
3. "Report of the SDC Magnet Task Force" (Chairman: T. Kirk), Solenoidal Detector Collaboration Note SDC-90-00095 (1990).
4. H. Iwasaki, "Momentum Resolution in a Nonuniform Magnetic Field," Solenoidal Detector Collaboration Note SDC-90-00097 (Aug. 1990);
   Y. Takaiwa, "Short Solenoid vs. Long Solenoid—Effects on Tracking," Solenoidal Detector Collaboration Note SDC-90-00103 (Oct. 1990).
5. "Subsystem R&D Proposal to Develop a Silicon Tracking System (1990-91)," submitted to the SSC Lab. (1990).
6. "Proposal for Front End Electronics Development for SSC Detectors," submitted to the SSC Lab. , U. Penn Preprint, (1990);
   S. Kleinfelder, M. Levi, O. Milgrome, "Test Results of a 90 MHz Integrated Circuit Sixteen Channel Analog Pipeline for SSC Detector Calorimetry," in *Proc. of the Fort Worth Symposium on Detector R&D for the SSC* (to be published) (1990);
   S. Kleinfelder, M. Levi, O. Milgrome, "Toward a 62.5 MHz Analog Virtual Pipeline Integrated Data Acquisition System," LBL-29608, submitted to Nucl. Phys. B." (1990);
   S. A. Kleinfelder, "A 4096 Cell Switched Capacitor Analog Waveform Storage Integrated Circuit," IEEE Trans. Nucl. Sci. **NS-37**, 56 (1990).
7. D. E. Groom, H. Hirayama, and W. R. Nelson, "Erratum to SSC-SR-1033," SSC Laboratory Report SSCL-285 (July 1990).
8. H. F. W. Sadrozinski *et al.*, "Radiation Hard Front End Electronics and Silicon Microstrip Detectors," in *Proc. of the Fort Worth Symposium on Detector R&D for the SSC* (to be published) (1990).
9. "The Pixel Detector Development Collaboration," submitted to the SSC Lab. (1990).
10. "SSC Detector Subsystem Summary Report and Proposal for FY1991," submitted to the SSC Lab. (1990).
11. "Hybrid Central Tracking Chamber Collaboration, Summary Report—Part I: Progress Report for FY1990," submitted to the SSC Lab. (1990).
12. S. Oh *et al.*, "Construction and Test of a Prototype Straw Chamber Detector of Length 2.7 Meters," Solenoidal Detector Collaboration Note SDC-90-00119 (1990).
13. W. T. Ford and M. Lohner, "Track Reconstruction in Straw Superlayers," in *Proc. of the Fort Worth Symposium on Detector R&D for the SSC* (to be published) (1990).
14. R. Openshaw, R. S. Henderson, W. Faszer, and M. Saloman, "Etching of Anode Wire Deposits with CF_4/Isobutane (80:20) Avalanches," in *Proc. of the Fort Worth Symposium on Detector R&D for the SSC* (to be published) (1990).
15. J. Kadyk, D. W. Hess, J. Vavra, and J. Wise, "Recent Work on Radiation-Hard Gases and Straw Tubes," in *Proc. of the Fort Worth Symposium on Detector R&D for the SSC* (to be published) (1990).
16. J. Dunn *et al.*, "Radiation Damage Studies of Straw Tube and Scintillating Fiber Elements," in *Proc. of the Fort Worth Symposium on Detector R&D for the SSC* (to be published) (1990);
    B. Zhou *et al.*, "Performance of Small-Radius Thin-Wall Drift Tubes in an SSC Radiation Environment at the MIT Research Reactor," BUHEP-90-2, (Dec. 1989);
    Subsystem Research and Development Proposal for a Compact Central Tracker for the SSC, submitted to the SSC Lab. (1990).
17. "Summary Report of the Fiber Tracking Group," submitted to the SSC Lab. (1990).
18. "Microstrip Track Chambers, Development of an Intermediated-Angle Spectrometer for Supercollider Detectors," submitted to the SSC Lab. (1990);
    and E. F. Barasch *et al.*, "Microstrip Track Chambers," in *Proc. of the Fort Worth Symposium on Detector R&D for the SSC* (to be published) (1990).
19. J. Matthews, "High-p_t Forward Pseudorapidity Tracking Trigger Using Silicon Planes," Solenoidal Detector Collaboration Note SDC-90-00067 (Aug. 1990).
20. For additional references see G. W. Foster, J. Freeman, and R. Hagstrom, in *Proc. 2nd International Conference on Advanced Technology and Particle Physics*, Como, Italy (to be published) (12 June 1989).
21. J. Proudfoot, "Radiation Damage to Scintillator and Wavelength Shifter Fiber and the Resulting Effects on Calorimeter Performance," Solenoidal Detector Collaboration Note SDC-90-00139 (1990).
22. M. Bertoldi *et al.*, "Radiation Damage Tests of New Scintillating Fibers and Plates," in *Proc. of the Fort Worth Symposium on Detector R&D for the SSC* (to be published) (1990).

23. Numerous papers on this subject in *Proc. of the Fort Worth Symposium on Detector R&D for the SSC* (to be published) (1990). See, for example, C. Zorn *et al.*, "Results of Preliminary Low Dose Rate Irradiation of Selected Plastic Scintillating Fibers;" J. Harmon and J. Walker, "A Review of Polymeric Scintillator Materials for Use at the SSC;" and R. Clough, "Radiation Damage to Organic Scintillators."
24. J. Proudfoot *et al.*, "Simulation Studies for Design Optimization of a Scintillator Plate Calorimeter," in *Proc. of the Fort Worth Symposium on Detector R&D for the SSC* (to be published) (1990).
25. P. M. Mockett and M. Boulware, "Electromagnetic Shower Sampling Efficiency in Liquid Argon Sampling Calorimeters and the Sampling Efficiency Dependence on Low-Z Cladding of High-Z Absorber Plates," in *Proc. of the Fort Worth Symposium on Detector R&D for the SSC* (to be published) (1990).
26. A. Buerhing *et al.*, "Scintillator Plate Mechanical Design," in *Proc. of the Fort Worth Symposium on Detector R&D for the SSC* (to be published) (1990); "Scintillator Plate Subsystem R&D Proposal for FY1991," submitted to the SSC Lab. (1990).
27. A. Stevens *et al.*, "Rad-Hard Electronics Development Program for SSC Liquid Argon Calorimeters," presented at the *International Industrial Symposium for the SSC* ," Miami FL, (March 1990); and H. W. Kraner, *et al.*, "Radiation Damage Studies on Hybrid Preamplifiers," in *Proc. of the Fort Worth Symposium on Detector R&D for the SSC* (to be published) (1990).
28. R. Dubois *et al.*, "SLD Liquid Argon Calorimeter Prototype Test Results," IEEE Trans. Nucl. Sci. **NS-33**, 194 (1986).
29. J. Brau, "Monte Carlo Studies with HETC," *Workshop on Compensated Calorimetry*, CALT-68-1305, (1985).
30. H1 Technical Progress Report (Oct. 1987).
31. C. Hearty, "Resolution and Hermeticity of the Liquid Argon Electromagnetic Calorimeter as a Function of Pseudorapidity," submitted to the SSC Lab. , SDC-90-00145 (1990).
32. I. Horvath *et al.*, "Magnetic Transformers for the SDC," submitted to the SSC Lab. , SDC-90-00069 (1990).
33. C. Hearty *et al.*, "Liquid Argon Calorimeter Readout with an Electrostatic Transformer and External Preamps," in *Proc. of the Fort Worth Symposium on Detector R&D for the SSC* (to be published) (1990).
34. "Warm Liquid Calorimetry Subystem R&D Proposal," submitted to the SSC Lab. (1990); M. Pripstein, "Warm Liquid Calorimetry," in *Proc. of the Fort Worth Symposium on Detector R&D for the SSC* (to be published) (1990).
35. P. Datte *et al.*, "A Liquid Scintillator Spaghetti Calorimeter EM Module for Forward Calorimetry at the SSC," in *Proc. of the Fort Worth Symposium on Detector R&D for the SSC* (to be published) (1990); P. Datte, *et al.*, "Effect of Radiation-Induced Discoloration on the Cladding of Liquid Scintillating Fibers," in *Proc. of the Fort Worth Symposium on Detector R&D for the SSC* (to be published) (1990).
36. S. Cihangir *et al.*, "High-Pressure Ionization Chambers for Calorimetry in High-Energy Physics," in *Proc. of the Fort Worth Symposium on Detector R&D for the SSC* (to be published) (1990).
37. G. Ascoli *et al.*, Nucl. Instr. and Meth. **A268**, 33 (1988).
38. C. Brown *et al.*, Nucl. Instr. and Meth. **A279**, 331 (1989).
39. R. Thun, "Iron-Scintillator Configurations for SDC Muon Triggers," Solenoidal Detector Collaboration Note SDC-90-00077 (1990).
40. U. Nauenberg, "The Use of Gas Čerenkov Counters as part of a Trigger System for Muons in SSC Detectors," Solenoidal Detector Collaboration Note SDC-90-00092 (1990).
41. G. Ascoli *et al.*, Nucl. Instr. and Meth. **A269**, 63 (1988).
42. I. Hinchliffe and M. D. Shapiro, "Resolution Parametrizations for the EoI," Solenoidal Detector Collaboration Note SDC-90-00035 (1990); I. Hinchliffe, "Resolution Parametrizations for the LoI," Solenoidal Detector Collaboration Note SDC-90-00100 (1990).
43. T. Hessing and S. Behrends, "Inclusive Jet Spectrum E_t Corrections and Resolution Unsmearing," Internal CDF Note CDF-1132 (1990).
44. F. Abe *et al.*, "A Measurement of $\sigma(W \rightarrow e\nu)$ and $\sigma(Z \rightarrow ee)$ in $\overline{p}p$ Collisions at $\sqrt{s} = 1800$ GeV," submitted to Phys. Rev. D.
45. R. N. Cahn, Rept. on Prog. in Phys. **52**, 389 (1989); E. Braaten and J. P. Leveille, Phys. Rev. **D22**, 715 (1980).
46. R. M. Barnett, K. Einsweiler, I. Hinchliffe, "Higgs Detection via Decays to Leptons with the SDC Detector," Solenoidal Detector Collaboration Note SDC-90-00099 (1990).
47. E. W. N. Glover and J. J. van der Bij, Phys. Lett. **B219**, 488 (1989).
48. Y. Sakai, "Pileup Issues in Electron Identification," Solenoidal Detector Collaboration Note SDC-90-00105 (1990).
49. R. N. Cahn *et al.*, in *Experiments, Detectors, and Experimental Areas for the SuperCollider*, p. 20, ed. by R. Donaldson and M. G. D. Gilchriese, Berkeley, CA, 1987 (1988).

50. C. Barter *et al.*, in *Proc. of the 1988 Summer Study on High Energy Physics in the 1990's,"* ed. by F. J. Gilman and S. Jensen, Snowmass CO, July 1988 (1989).

51. J. E. Brau *et al.*, in *Proc. of the 1988 Summer Study on High Energy Physics in the 1990's,"* ed. by F. J. Gilman and S. Jensen, Snowmass CO, July 1988 (1989).

52. R. P. Kauffman, in *Proc. of the 1990 DPF Summer Study on High Energy Physics,"* Snowmass CO, (to be published).

53. B. Hubbard, "Fragmentation Properties of Jets Produced in Proton-Antiproton Collisions at $\sqrt{s} = 1.8$ TeV," PhD Thesis, LBL-27687, (1989).

54. R. Harris, for the CDF Collaboration, "Recent Results on Direct Photons from CDF," to be published in the *Proc. of the Workshop on Hadron Structure Functions and Parton Distribution Functions*, Fermilab (April 1990).

55. M. L. Mangano, "Production of $W + H \rightarrow e/\mu + \gamma\gamma$," Solenoidal Detector Collaboration Note SDC-90-00113 (1990).

56. A. Barbaro-Galtieri, "Study of Top Pair Production in Electron-Muon Events with SDC," Solenoidal Detector Collaboration Note SDC-90-00038 (1990).

57. G. Altarelli *et al.*, Nucl. Phys. **B308**, 724 (1988).

58. R. J. Hollebeek, H. H. Williams, P. K. Sinervo, "Reconstructing 250 GeV Top Quarks Using Multi-Jet Final States," Solenoidal Detector Collaboration Note SDC-90-00117 (1990),
"Uncertainties in Estimating the Top Quark Mass using the Multi-Jet Final States," Solenoidal Detector Collaboration Note SDC-90-00118 (1990).

59. R. M. Barnett, J. F. Gunion, B. Hubbard, "Determining the Mass of the Top Quark with the SDC Detector," Solenoidal Detector Collaboration Note SDC-90-00140 (1990) .

60. R. J. Hollebeek, H. H. Williams, P. K. Sinervo, "Reconstruction of Top Quarks in an SSC Solenoidal Detector," Solenoidal Detector Collaboration Note SDC-90-00030 (1990).

61. B. Hubbard, "Efficiency for b-jet Tagging in $t\bar{t}$ Events," Solenoidal Detector Collaboration Note SDC-90-00031 (1990).

62. A. Barbaro-Galtieri, A. Bay, A. Palounek, M. Austern, "Measurement of the Top Mass in the $e\mu$ Channel," Solenoidal Detector Collaboration Note SDC-90-00133 (1990).

63. D. Decamp *et al.*, Phys. Lett. **B244**, 551 (1990).

64. F. Abe *et al.*, Phys. Rev. Lett. **64**, 142 (1990).

65. J. F. Gunion, H. E. Haber, G. Kane, S. Dawson, *The Higgs Hunters Guide*, Addison Wesley (1990).

66. R. M. Barnett, J. F. Gunion, H. E. Haber, I. Hinchliffe, B. Hubbard, H.-J. Trost, "Searching for Top Decays to Charged Higgs Bosons with the SDC Detector," Solenoidal Detector Collaboration Note SDC-90-00141 (1990); and references therein.

67. R. Blair *et al.*, " SDC Hadronic Mass Resolutions in Z and Z' Decays," Solenoidal Detector Collaboration Note SDC-90-00150 (1990).

68. A. Para *et al.*, "Jet Energy Resolution of the SDC Detector," Solenoidal Detector Collaboration Note SDC-90-00149 (1990).

69. I. Hinchliffe, M. L. Mangano, and M. D. Shapiro, "Z_η Production with the SDC Detector," Solenoidal Detector Collaboration Note SDC-90-00036 (1990).

70. D. E. Groom, "Energy Scaling of Low-Energy Neutron Yield, the e/π Ratio, and Hadronic Response in a Calorimeter," *Proc. of the Workshop on Calorimetry for the Superconducting Super Collider,* Tuscaloosa, Alabama, 13–17 March 1989, ed. R. Donaldson and M. G. D. Gilchriese, World Scientific (June 1990), 59–75.

71. J. Freeman and C. Newman-Holmes, in *Experiments, Detectors, and Experimental Areas for the SuperCollider,* p. 673, ed. by R. Donaldson and M. G. D. Gilchriese, Berkeley, CA, 1987 (1988);
A. Bay *et al.*, in *Proc. of the 1988 Summer Study on High Energy Physics in the 1990's,"* p. 882, ed. by F. J. Gilman and S. Jensen, Snowmass CO, July 1988 (1989).

72. I. Hinchliffe, M. D. Shapiro, "Z' Production with the SDC Detector," Solenoidal Detector Collaboration Note SDC-90-00115 (1990).

73. C. Albajar *et al.*, Z. Phys. **C44**,15(1989).

74. R. Ansari *et al.*, Phys. Lett. **194B**, 158 (1987).

75. F. Abe *et al.*, Phys. Rev. Lett. **63**, 720 (1989).

76. G. Eppley and H. Miettinen, "Asymmetry vs. Mass for a 4 TeV Z'," Solenoidal Detector Collaboration Note SDC-90-00125 (1990).